INSTITUTO SUPERIOR DE ENGENHARIA DE LISBOA

Área Departamental de Engenharia Eletrotécnica de Energia e Automação

Analysis of Nickel-Copper Metallic Foam Supercapacitor for Electric Vehicles with Hybrid Battery-Supercapacitor Energy Storage System

LEONARDO CORRÊA MALBURG
B.A. Design Industrial

Trabalho Final de Mestrado para Obtenção do Grau de Mestre
em Engenharia Eletrotécnica – Ramo de Energia

Orientadores:
Professora Dra. Rita Marcos Fontes Murta Pereira
Professora Dra. Maria Teresa Oliveira de Moura e Silva

Júri:
Presidente: Professor Dr. Luís Manuel dos Santos Redondo (ISEL)
Vogais:
Professor Dr. Miguel Cabral Ferreira Chaves (ISEL)
Professora Dra. Rita Marcos Fontes Murta Pereira (ISEL)

Dezembro de 2019

Abstract

For centuries, the indicators of CO_2 had never been so higher than past half century indicators, accounting for an increase rate of 1,5 ppm/year. This is the direct reflect of global warming, a problem that has motivated researchers on developing adequate alternatives for a variety of human needs, which is the case of transitioning from fossil fuels to renewable electrical powering sources, such as Electric Vehicles trending. This dissertation concerns one of the most delicate aspect about electric vehicles (EVs) design, the Energy Storage System, which regarding autonomy, is the key to overcome the current transportation electric energy sources limitations. Among the numerous known devices, Batteries and Supercapacitors are the main technologies in which electric vehicles energy storage relies on. However, batteries because of their chemical nature can be environmentally harmful when considering disposal aspects, concern which has motivated the energetic development and improvement of greener technologies, such as supercapacitos. This dissertation presents a proposition for the development procedure of a positive electrode nickel-copper hybrid supercapacitor theoretical cell, which was simulated, and the resulting data analyzed and discussed. Therefore, the hybridization of both technologies was subjected to computational simulations in order to test the hypothesis that a direct parallel connection between both technologies could interact collaborating to extend battery's lifespan, hence, reducing its environmental impact. The simulations have shown that such interaction results in reduced current demand, causing the state of charge wave period to increase, thus, extending the lifespan of batteries.

Keywords

Electric Vehicle

Energy Storage Systems

Supercapacitor

Battery

Hybrid

Análise e Comparação de Supercondensadores com Base em Espumas Metálicas de Níquel-Cobre em Veículos Elétricos com Sistema Híbrido de Armazenamento de Energia

Resumo

Durante séculos, os indicadores de CO_2 nunca estiveram tão elevado quanto no último meio século, o que representa uma aumento de 1,5 ppm/ano. Este dado é reflexo direto dos efeitos do aquecimento global, problema o qual tem motivado pesquisadores no intuito de desenvolver novas e mais adequadas alternativas para nossas mais diversas necessidades, à exemplo disto a transição do consumo de combustíveis fósseis para fontes renováveis de energia elétrica, impactando diretamente nos veículos elétricos. Este trabalho refere-se à um dos aspectos maior peso no projeto de veículos elétricos (VEs), o Sistema de Armazenamento de Energia, o qual em termos de autonomia é crucial para superar as atuais limitações das fontes de energia elétrica para apicações móveis. Entre os inúmeros dispositivos conhecidos, baterias e supercapacitores são as principais tecnologias nas quais o armazenamento de energia de veículos elétricos é hoje dependente, sendo implementado por diversos fabricantes em uma grande variedade de categorias veículares. Entretanto, devido à composição das baterias eletroquímicas, estes dispositivos acabam por se tornarem ambientalmente prejudiciais consoante ao processo de descarte e reciclagem de seus componentes uma vez que compostos químicos possuem processos normalizados e controlados para o descarte. Sendo assim, esta dentre outras questões tem motivado pesquisadores a desenvolverem novos materiais com uma viés ecologicamnte correta assim como o esforço no desenvolvimento de outras tecnologias de armazenamento de enrgias, atuais ou novas, com base nos mesmos princípios já citados.

Dentre as tecnologias pesquisadas encontram-se os supercondensadores, os quais devido à diferenciação para com as baterias consoante à tecnologia de armazenamento, não deixam resíduos químicos como consequência de seu descarte, sendo assim considerados dispositivos ecologicamente corretos. Com o intuito de paralelamente estudar e desenvolver um procedimento para a modelização de células de supercapacitores a

partir de materiais ensaiados laboratorialmentes com o intuito da utilização como eletrodos de tais dispositivos, as espumas metálicas de níquel-cobre [Eugénio13] foram escolhidas para tal processo, as quais apresentam elevada área de superfície específica para as reações eletroquímicas ocorrerem, fator o qual é conhecidamente motivo de influência nos valores de capacitância obtidos. Devido a proposta original do material estudado ser relacionada ao uso como eletrodo positivo, o processo desenvolvido deu origem a um supercondensador do tipo híbrido, o qual contou com um eletrodo negativo de carbono ativado complementar ao de níquel-cobre. Tal dispositivo mostrou-se capaz de apresentar capacitâncias superiores (454F) quando comparados ao dispositivo base de projeto, Maxwell 2.3V 300F. Entretanto, devido ao potencial eletroquímico inferior do Ni-Cu, o dispositivo híbrido apresentou uma tensão nominal reduzida de 2V quando em comparação ao dispositivo base. Para a implementação dos dados gerados em um bloco padrão do software Matlab Simulink, foi seguido o procedimento descrito por [Zubieta00] sendo que devido a falta de informações, complementarmente foi desenvolvido um procedimento de otimização não linear através do software Microsoft Excel via plugin Solver para a obtanção de tais dados. Esta etapa mostrou-se efetiva uma vez que os dados resultantes mostraram-se correspondentes ao esperado com base em [Zubieta00]. A partir disso, o perfil de corrente imposto ao sistema, conforme apresentado em [Omar09], foi validado através de uma segunda simulação computacional, também via Matlab Simulink, na qual a mesma configuração de elementos de armazenamento de energia, baterias e supercapacitores, foi implementada e submetidos ao perfil de carga mencionado. Esta simulação resultou em dados os quais validaram o apresentado em [Omar09] através da comparação dos perfis de correntes resultantes do banco de baterias e módulo de supercondensadores. Como a vida útil das baterias é determinada pelo consumo de cíclos face ao número máximo determinado em ficha técnica, os quais são computados pelo conjunto dos eventos de carga de descarga (ciclo) do dispositivo, uma terceira simulação foi desenvolvida, esta com o intuito de controlar a imposição de corrente e geração de ciclos completos e uniformes. Tal simulação demonstrou uma redução no na corrente demandada e número de ciclos completados pela bateria em módulo híbrido quando comparada ao mesmo procedimento em modo solo, sendo que esta redução é caracterizada por períodos mais longos entre picos, sendo assim uma extensão teórica da vida útil do dispositivo de

aproximadamente 36 minutos (2%). Com o intuito de utilizar a empilhadeira elétrica Carer R45NCF [Omar09] um modelo tridimensional foi desenvolvido através do software AutoCAD 2014 com o intuito de identificar dois parâmeteros necessários, área frontal do veículo e localização do centro de gravidade.

A partir dos dados obtidos uma simulação do veículo elétrico (empilhadeira) foi desenvolvida, apresentando como sistema de armazenamento de energia as mesmas configurações já citadas. Nesta simulação o perfil de carga foi convertido de corrente para velocidade angular através das equações das dinamicas de movimento para veículos. Para além disso, neste modelo foram aplicados ambos os supercapacitores, Maxwell 2.3V 300F e supercapacitor híbrido de Ni-Cu/AC. Os resultados obtidos para o dispositivo da Maxwell foram concordantes aos obtidos nas simulações anteriores, sendo que também foi observada a redução nas correntes de descarga das baterias submetidas aos sistemas solo e híbrido. Já para o supercondensador híbrido de Ni-Cu/AC, notou-se um lijeiro aumento na contribuição fornecida para com a bateria, resultado esperado face a diferença de capacitância, consequentemente também de carga, quando comparado ao supercapacitor Maxwell 2.3V 300F. O dispositivo contribuiu para a redução da demanda do sistema para com a bateria fornecendo maior corrente nos momentos de picos de descargas quando comparado ao dispositivo base.

Palavras-chave

Veículos Elétricos

Sistemas de Armazenamento de Energias

Supercapacitores

Baterias

Híbrido

Agradecimentos

Esta dissertação tem um significado de grandes proporções em nossas vidas, trabalho o qual marca o início de uma nova jornada e é símbolo de tudo aquilo que abdicamos para que chegássemos até este momento, é um lembrete sobre os ausentes momentâneos e daqueles que hoje vivem em memória.

À Professora Doutora Rita Marcos Fontes Murta Pereira, quero deixar meu mais profundo agradecimento pelo imenso apoio prestado, pelas inúmeras idas e vindas na busca pela consolidação da temática de trabalho, pela constante disponibilidade para quaisquer questionamentos, pelo suporte prestado e conhecimentos transmitidos. Agradeço os diversos conselhos, os quais foram sempre da maior valia para a ótima evolução deste trabalho. Enfim, agradeço por ter acreditado em mim, em minha proposta de trabalho, por ter partilhado do meu objetivo com paciência e clareza sem iguais.

À Professora Teresa Oliveira de Moura e Silva, agradeço o tamanho suporte na transmissão do conhecimento particular à sua àrea de pesquisa, conteúdo fundamental para o desenvolvimento deste trabalho. Desta forma, agradeço o apoio prestado na consolidação do conteúdo aqui apresentado, assim como toda a disponibilidade na resolução de dúvidas e auxílio à pesquisa.

Entretanto, o hoje não se faz somente do agora e sim, é uma reação do ontem e efeito de escolhas e oportunidades ao longo de uma caminhada. Desta forma, devo meu mais sincero agradecimento às pessoas que estiveram comigo desde o primeiro momento, aqueles os quais demonstraram apoio e amor incondicionais, guiaram-me pelos primeiros passos em direção às oportunidades as quais foram essenciais para a definição do meu caráter e escolhas que moldaram meu futuro. Aos meus pais, meus mais sinceros agradecimentos.

Esta jornada certamente só foi possível graças ao apoio diário e incansável daquela que tem sido minha parceira por mais de quinze anos, minha melhor amiga, namorada, minha esposa, a companheira de encontros e desencontros, de aventuras, parte essencial na

conclusão desta nossa mais nova jornada. À ti Sara, a minha imensa gratidão e meu sincero amor.

Aos meus sogros, Márcia e Mauricio, os quais fazem parte da minha vida já há mais de uma década, os quais nos apoiam em todas as jornadas, com conselhos e exemplos, estando sempre presentes para tudo o que for necessário, o meu mais sincero afeto, respeito e meu imenso obrigado.

Eu não poderia deixar de agradecer ao meu primo Arthur, sem o qual esta já difícil jornada teria sido ainda mais árdua. À você, quem nos deu abrigo, suporte, atuou como guia deste novo mundo que é Portugal, quem se esforçou com sucesso para que nos sentíssemos em casa, não somente o meu, porém o nosso muitíssimo obrigado, jamais iremos esquecer.

Quero deixar meu imenso agradecimento ao Murphy, o qual tem sido meu parceiro de estudos diário, estando junto à mim pelo tempo necessário e noite afora, sempre ao meu lado pelas inúmeras madrugadas enquanto escrevia esta dissertação. Ao nosso cão, meu melhor amigo, o meu amor e sincero agradecimento.

À todos aqueles que, de alguma forma, contribuíram para que eu chegasse até este momento, meu mais sincero obrigado!

Index

List of Figures

List of Tables

Abreviations List

2E	Two-Electrode Configuration
3E	Three-Electrode Configuration
A.C	Activated Carbon
AC	Alternating Current
Al	Aluminum
AECs	Aluminum Electrolytic Capacitors
AWG	American Wire Gauge
BEV	Battery Electric Vehicles
BP	Black Phosphorous
CAES	Compressed Air Energy Storage System
CEF	Connecting Europe Facility
CO_2	Carbon Dioxide
COFs	Covalent Organic Frameworks
CNTs	Carbon Nanotubes
CPE	Constant Phase Element
CPR	Capacitive Potential Range
CPs	Conducting Polymers
CV	Cyclic Voltammetry
DFT	Density Functional Theory
DC	Direct Current
DQDs	Double Quantum Dots
ED	Energy Density
EDL	Electric Double Layer
EDLC	Electric Double Layer Capacitor
EVs	Electric Vehicles
ECs	Electrochemical Capacitors
EN	Negative Electrode
ESS	Energy Storage Systems
EP	Positive Electrode

ESP	Gravimetric Specific Energy
ESR	Equivalent Series Resistance
EU	European Union
EBA	European Battery Alliance
FES	Flywheels Energy Storage System
GCD	Galvanostatic Charge and Discharge Curves
GV	Galvanostatic
HEVs	Hybrid Electric Vehicles
HESS	Hybrid Energy Storage System
HPES	Hydro Pumped Energy Storage System
IEA	International Energy Agency
IHP	Inner Helmholtz Plane
IUPAC	International Union of Pure and Applied Chemistry
LCOE	Levelized Cost of Energy
LP	Linear Optimization Problem
MCV	Maximum Charging Voltage
MOFs	Metal-Organic Frameworks
NMFs	Nanoporous Metallic Foams
NOAA	National Oceanic Atmospheric Administration
NLP	Nonlinear Optimization Problem
OHP	Outer Helmholtz Plane
PD	Power Density
PHEV	Plug-In Hybrid Electric Vehicles
PM	Permanent Magnet
PSP	Specific Power
PZV	Potential of Zero Voltage or Equipotential
REEV	Range-Extended Electric Vehicles
RFB	Redox Flow Battery
Ri	Immediate Branch Resistance
Rl	Long-term Branch Resistance
SAE	Society of Automotive Engineers
SCE	Saturated Calomel Electrode

SDS	Sustainable Development Scenario
SEM	Scanning Electron Microscopy
SEVs	Solar Electric Vehicles
SI	International System of Units
SMES	Super-Conducting Magnetic Energy Storage
SOC	State of Charge
SR	Switched Reluctance
SSA	Specific Surface Area
NASA	United States National Aeronautics and Space Administration

List of Symbols

Constants and variables

β	CPE Exponent
δ	Mass Factor; Diffusion Layer Thickness; Effect of Powertrain
Δi	Current Inversion (A)
ΔV	Potential Difference (V)
ε	Dielectric Constant (F m^{-1})
ε_0	Dielectric Constant of Free Space (F m^{-1})
ε_r	Dielectric Constant of Material (F m^{-1})
η_m	Motor Efficiency/Losses (%)
η_t	Transmission Efficiency/Losses (%)
μ	Medium Permittivity (F m^{-1})
ρ	Density (kg m^{-3})
ΣF_t	Total Tractive Effort (N)
ΣF_{tr}	Total Resistance (N)
τch	Proportionality Coefficient of a Complete Cycle
τdc	Proportionality Coefficient of a Complete Cycle
υ	Scan Rate (V s^{-1})
ωC	Absolute Angular Velocity of Terminal C (rad s^{-1})
ωR	Absolute Angular Velocity of Terminal R (rad s^{-1})
A	Area (m^2)
c	Coil Circumference (m)
CC	Constant Current
C_{cell}	Capacitance of Cell (F)
CCR_{ich}	Complete Cycle Rate for the Charge Curve
CCR_{idc}	Complete Cycle Rate for the Discharge Curve
C_D	Aerodynamic Drag Coefficient
C_{dl}	Double Layer Capacitance (F)
C_{elec}	Capacitance of Electrode (F)

$C_{elec}{}^{c<}$	Smaller Electrode Capacitance (F)
$C_{elec}{}^{c>}$	Greater Electrode Capacitance (F)
CG	Center of Gravity
Ci	Three Branches Supercapacitor Capacitance (F)
$Ci0$	Immediate Branch Capacitance (F)
$Ci1$	Voltage Dependent Capacitance (F V^{-1})
Cd	Direct Branch Capacitance (F)
Cl	Long-term Branch Capacitance (F)
C_p	Pseudocapacitance (F)
C_{rate}	Battery Rated Capacity (Ah)
$C_{sp.asymm.cell}$	Specific Capacitance of Asymmetric Cell (F g^{-1})
$C_{sp.cell}$	Specific Capacitance of Cell (F g^{-1})
$C_{sp.CV}$	Specific Capacitance from CV Tests (F g^{-1})
$C_{sp.GCD}$	Specific Capacitance from GCD Tests (F g^{-1})
d	Dielectric Thickness (m)
D	Wire Diameter; Lead Screw Diameter (m)
E	Energy (Wh)
E^0	Electrochemical Potential (V)
E_{out}	Net Energy Consumed from Storage Source (Wh)
$E_{max.hybrid}$	Maximum Energy Storage Capability of Hybrid Supercapacitor (Wh)
$E_{sp.hybrid}$	Gravimetric Specific Energy of Hybrid Supercapacitor (Wh kg^{-1})
F_{bf}	Frontal Brake Force (N)
F_{br}	Rear Brake Force (N)
F_f	Rolling Resistance (N)
F_g	Grading Resistance (N)
Fr	Rolling Resistance (N)
f_r	Rolling Resistance Coefficient
F_{rd}	Road Resistance (N)
F_{rf}	Front Tire Rolling Resistance (N)
F_{rr}	Rear Tire Rolling Resistance (N)
F_{tf}	Front Tire Tractive Effort (N)
F_{tr}	Rear Tire Tractive Effort (N)

F_w	Aerodynamic Drag (N)
H	Core Height (m)
h_g	Height of the Center of Gravity (m)
h_w	Height of the Center of Application of Aerodynamic Resistance (m)
i	Current Density (A m^{-2})
i_0	Gear Ratio of Final Drive
Ib	Battery Current (A)
Ic	Supercapacitor Current (A)
Ich	Charge Current (A)
Idc	Discharge Current (A)
i_g	Gear Transmission Ratio
Kv	Voltage Dependent Capacitance (F V^{-1})
L	Inductance (H)
L_{fr}	Distance from Frontal to Rear Axle (m)
L_a	Distance from Frontal Axle to Center of Gravity (m)
L_b	Distance from Rear Axle to Center of Gravity (m)
m	Terrain Inclination Grade (%)
m_{cell}	Supercapacitor Cell Mass (kg)
m_s	Mass of the Solid (kg)
m_{total}	Total Mass of Both Active Materials (kg)
M_v	Vehicle Mass (kg)
M_vj	Forward Force (N)
N	Number of Turns
N_{in}	Rotational Speed Input (rad s^{-1})
N_{out}	Rotational Speed Output (rad s^{-1})
p	Coil Pitch (m)
$P_{b\text{-}out}$	Battery Output Power (W)
$P_{sp.hybrid}$	Usable Specific Power of Hybrid Supercapacitor (W kg^{-1})
Q	Battery Capacity (Ah)
Ri	Immediate Branch Resistance (Ω)
r_d	Effective Radius of the Wheel (m)
Rd	Direct Branch Resistance (Ω)

R_f	Electrode/Electrolyte Resistance (Ω)
Rl	Long-term Branch Resistance (Ω)
R_p	Faradaic Charge Transfer Resistance (Ω)
R_s	Series Resistance (Ω)
T	CPE Parameter (F $cm^{-2}s^{\alpha-1}$)
T_p	Torque Output from the Power Plant (N.m)
T_{rf}	Frontal Rolling Resistance Torque (N.m)
T_{rr}	Rear Rolling Resistance Torque (N.m)
T_w	Driving Wheel Torque (N.m)
U	Energy Density (J m^{-3})
V_{drop}	Voltage Drop (V)
V_w	Wind Speed (m s^{-1})
W_f	Frontal Load (N)
W_r	Rear Load (N)
Y_0	Diffusion Admittance (℧)
Z_{CPE}	Impedance for the Constant Phase Element (Ω)
Z_P	Faradaic Impedance for the Positive Electrode (Ω)

CHAPTER 1

Introduction

This chapter presents an overview of the global climate situation from the historic and current perspectives to emphasize the pollution increasing levels, which results from the uncontrolled usage of the world's natural resources. In this chapter is also mentioned the need for a change from the predominant consumption of fossil fuels to renewable sources, such as the electric energy. As for the electric energy to be consumed, storage devices must be in steady development to adapt to the increasing demand. Finally, the dissertation framework is presented, as well as its intent, the technology state of the art and objectives.

1.1 Global Climate Situation – The Great Motivator

The global climate has constantly changed throughout history. These changes happened naturally, as result of the planet's formation and evolution of primitive life forms. However, there was an important difference between that period and nowadays, one detail that exponentially worsen this scenario, the humankind. In its early ages, planet Earth had singlehandedly managed to keep the balance of its environment, and during the past 400 thousand years, its carbon dioxide (CO_2) cyclic emission rates have been kept under 300 ppm/year, resulting in an approximate average increase rate of 0,01 ppm/year [Etheridge96]. However, the humans rising abruptly changed this nearly steady cyclic situation to a unprecedent chaos. According to the United States National Aeronautics and Space Administration (NASA) official website [NASA19], after collecting and analyzing several publications on this subject, it was noticed that since 1950 the carbon dioxide rates have changed their pattern to a rapid ascending behavior, surpassing its historical maximum. The data gathered basically compares information from Vostok ice core samples with the National Oceanic Atmospheric Administration (NOAA) CO_2 records, which contains the compound's concentration data acquired from the analysis of air trace trapped in the ice of Antarctica (Fig. 01).

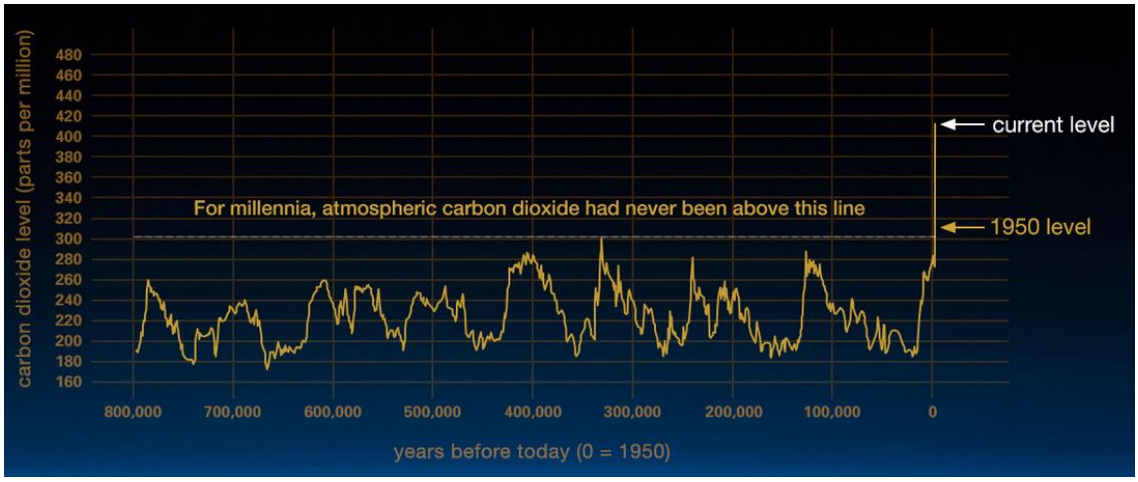

Figure 01 – CO_2 data records [NASA19].

Even though CO_2 emissions just overcame the historical rates from the 1950's, it all truly began with the industrial revolution of late 18th century. The change between the hand production to machines, provided an enormous increase in manufacturing capacity, allowing companies to experience technologies that could

work incessantly as no man ever would. Together with the modern manufacturing equipment, new chemical compounds and processes were developed and presented to the industry community, as the iron manufacturing technology, which have been one of the key materials for the daily production of many different industries. In order to fuel that new scenario, steam power machines were vastly implemented, equipment which were essentially powered by coal [Stearns13].

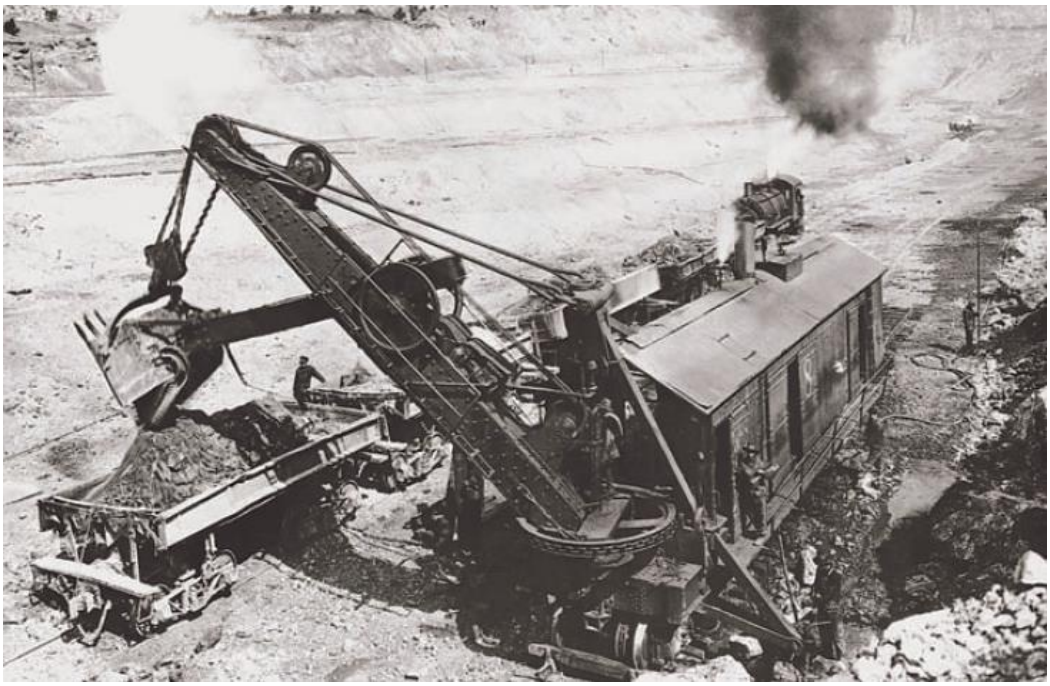

Figure 02 – Stem powered mining excavator [Kras04].

That specific aspect together with the unprecedent and unplanned population growth, initiated a chain of events that then would lead us to the late 19th century, when some industries started to gradually insert chemicals as powering sources, paving the way to the so-called second industrial revolution. Even though petroleum early records dates from more than two thousand year ago, with its use being attributed to the ancient Chinese during the Western Han dynasty that last from 206 BCE to 9 CE [Bielenstein80], the first modern record regarding a well drilling dates from the 1870s in South Caucasus, ancient Russian Empire, region which was formed by Abkhazia, Armenia, Azerbaijan, Georgia, Nagorno-Karabakh, South Ossetia and Russia's North Caucasus [Stearns13].

Figure 03 – Azerbaijan national photo & film archive – Oil rig [AFC19].

While the petroleum industry grew and solidified as main energy source and one of the most profitable markets known today, minimum attention was being directed to the consequences of its massive trading and consumption. However, for the past twenty years scientists worldwide started to suggest that the recent climate events had in fact someone to blame, humankind, as previously mentioned. They have gathered evidences to sustain that hypothesis and such event was then called the anthropogenic (*Anthropos:* human, *Genesis:* origin) effect, "from human origin". Basically, global warming occurs by the malfunctioning on the natural heating relation between the Sun and the Earth due to an external factor. When the solar radiation reaches our atmosphere, just part is reflected while great portion is in fact absorbed causing the planet's temperature to rise. Complementary, the heating causes the Earth's surface to emit back longer wavelengths in the form of infra-red radiation towards the atmosphere, what acts as a protective layer for all lifeforms. Without this protective shell, colder temperatures would prevail causing the climate to change. Therefore, contrary to what most people may conclude, the greenhouse gasses are vital for life to exist the way we understand it. However, as result of human unnatural emissions, this protective layer has become thicker over the years which has unbalanced the relation of internal and external radiation emissions, therefore an increase in the planet's temperature [Eurostat19].

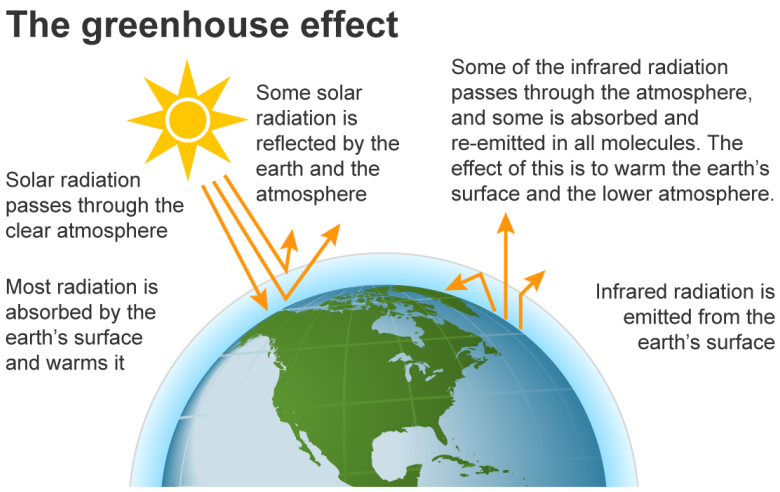

Figure 04 – Greenhouse emissions exchange [EIA19].

As the planet's resources are being recklessly consumed in an ascending rate, the need for an alternative is more than clear, especially when considering the increasing pollution indicators, leading to climate disturbances. Oil is no longer the only economically feasible energy source available to power our civilization. For the last 50 years, the global modern renewable energy consumption has increased in over 5 times, accounting now more than 5 thousand TWh/y [OWiD16].

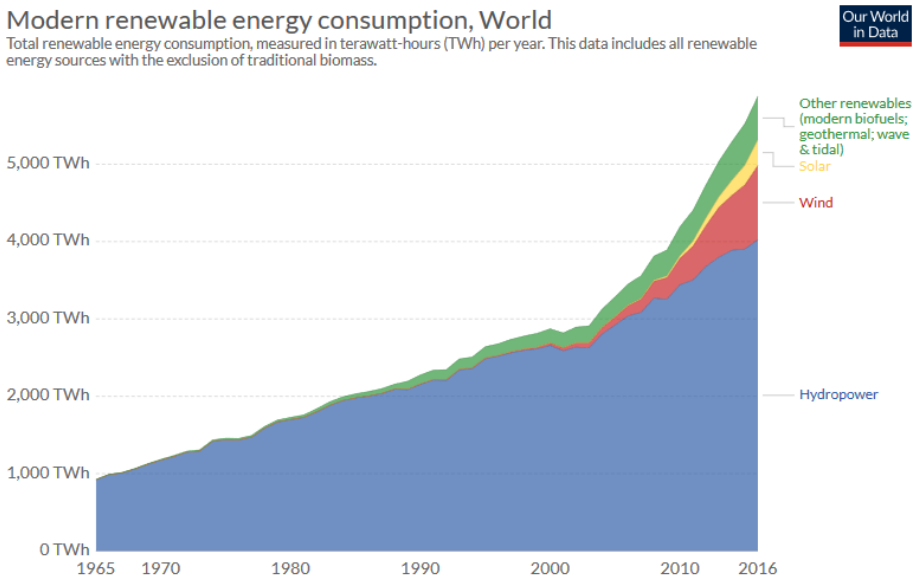

Figure 05 – Demand increase [OWiD16].

Nowadays, renewable energy sources are implemented in a way that its global market share accounts for a third of the total power capability. In 2018, the sector received an

addition of about 170 GW regarding generation capability worldwide. Even though that renewable energy increased from a wide perspective and consequently non-renewable sources have decreased in regions like Europe, North America and Oceania, which accounted a reduction of about 85 GW since 2010, in Asia and Middle East it took an inverse path actually increasing the non-renewable generation capacity by about 115 GW over the same period [IRENA19].

In addition to the ecological perspective, the major decision point lies in lowering the costs of such technologies in a way that the exchange becomes economically appealing. By the end of 2017, the levelized cost of Energy (LCOE) regarding the different power generation technologies commonly implemented, have reached considerable soundness to its analogous, fossil fuels. Due to the major scientific and economic efforts, a variety of more feasible manufacturing processes and materials have made renewable energy sources a definitively tangible investment. In 2016 the LCOE referred to the global photovoltaic generation dropped 17%, as for the onshore and offshore wind generations the reduction was of 18% and 28%, respectively [Ram17].

Based on the indicators, it can therefore be asserted that the so-called green energy sources are a fact and possess a share of the world's energy market of most significance. However, it is undeniable that our urban infrastructure is not entirely set to receive it as it is and has historically been destined for fossil fuels. The need for adaptation is clear and urgent. If we take both generic forms of energy, renewable and fossil, thee green energy is much less reliable due to its unpredictability in relation to the generation consistency. A solar farm can have its production levels dropped significantly or even ceased for a certain period due to cloudy seasons, what is also possible to other renewable energy technologies and their related sources. Therefore, controlling software and energy storage technologies have been incessantly developed as a form of adaptation so the renewable energy technologies can consolidate their worldwide presence.

1.2 Framework – Batteries and Supercapacitors

Energy storage systems (EES) are capable to store energy in many forms throughout different technologies and by that, are often referred as multi-physic devices. The vast variety of technologies were developed at some point to supply certain need since none of the technologies is suitable to every situation. Therefore, the comparison between each

storage technology is only possible when specific applications are taken into consideration (Fig. 06).

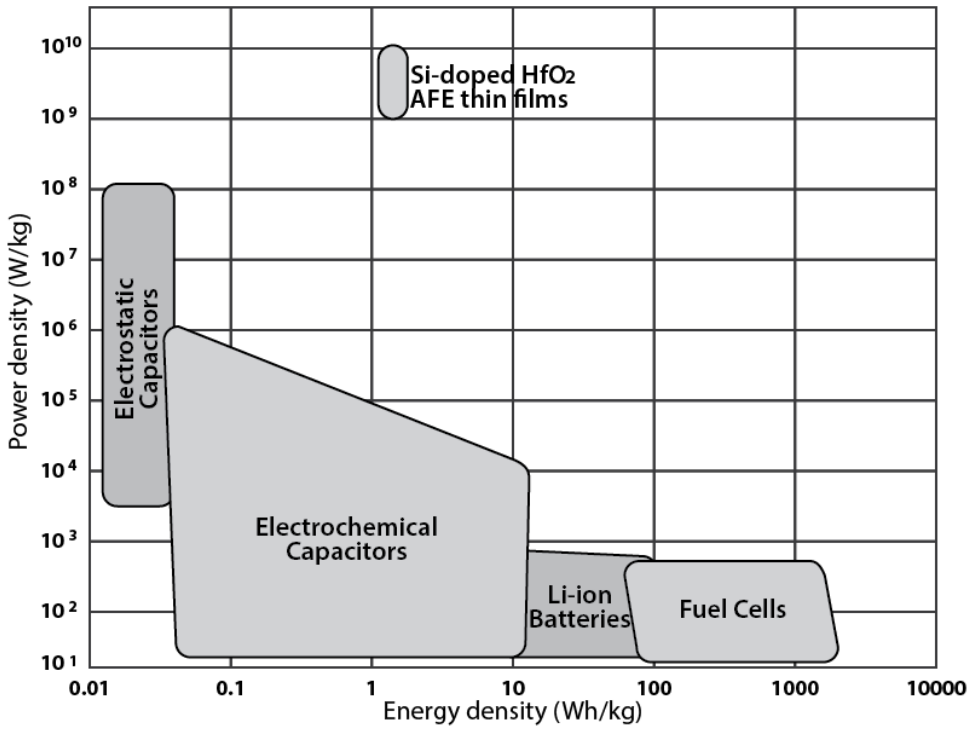

Figure 06 – Ragone chart [Faizan17].

Certain comparison parameters, such as storage technology and the nature of the application, stationary of mobile, are the preferable methods of crosschecking the devices performance and profitability [Moseley15]. From electrical to mechanical and chemical sources, energy storage devices are offered in a variety that tends to be suitable to any sort of generation technology. The difference lies on the form of energy which it is required to store, which can be directly electrical or may require an intermediate transformation process, as is the case of mechanical sources like flywheels. The ESS are in fact divided in two great groups, the indirect and the direct electrical energy storage devices (Fig. 07).

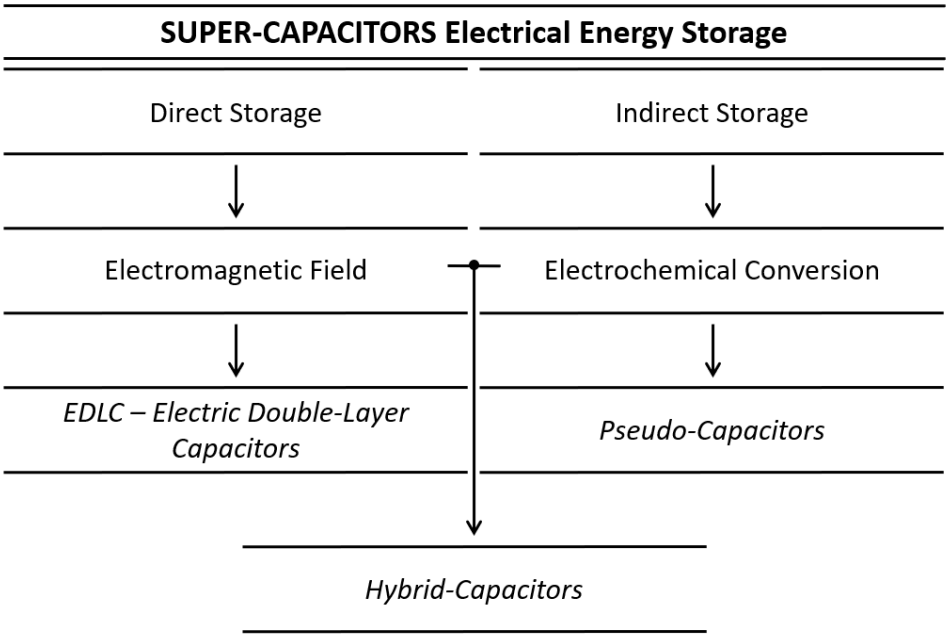

Figure 07 – Direct and indirect supercapacitors technologies [Grbovic13].

Direct Energy Storage Devices

Direct energy storage devices are purely electrical, meaning that the input is of the same nature as its outcome, so no conversion takes place in the storage process. The storage medium that such devices use is either electrostatic or magnetic fields, electromagnetic fields. This group is basically formed by electric capacitors and inductors, as well as their variations. As both technologies are insufficient for most of the high demand applications, supercapacitors and super-conducting magnetic energy storage (SMES) were developed, which possesses greater storage characteristics than their predecessors.

Indirect Energy Storage Devices

The indirect devices technology is based on the usage of secondary mediums which enables the electric energy to be stored as different forms, such as mechanical and chemical, which then is supplied as electricity. In this case, electrical energy is performed via a converter, such as an electric machine (motor or generator) for mechanical energy, and reactors for chemical reactions. As for mechanical energy, it is rather stored as kinetic or potential energy, throughout devices called flywheels (FES) when of kinetic nature,

and hydro pumped (HPES) or compressed air (CAES) energy storage systems for potential energy input.

As for the devices which relies on electrochemical conversion reactions, the electric energy is converted into chemical potential energy, which can be stored in either batteries or fuel cells.

Batteries and Supercapacitors

While electrochemical batteries play an historical and important role worldwide, being lithium ion (Li-ion) batteries its most common representative, supercapacitors are as equally stablished. Both technologies are applicable for contemporary storage needs, however as their characteristics differ so do their applications.

Batteries are devices which storage capability overcome supercapacitors regarding the amount of stored energy (Fig.06). The energy density (*U*), as this property is called, concerns the amount of energy that a device can store in relation to its volume, which its SI unity is stated in joules per cubic meters ($J\ m^{-3}$). Supercapacitors commercial technologies can store only 10% of what is possible by Li-ion batteries, which in fact is the main reason why batteries are widely implemented as the primary source in most applications, from powering small portable devices to electric vehicles. However, their differences are not restricted to energy density nor the batteries are the better solution for all needs.

Among the other characteristics of ESS an equally important one is power density, which concerns the amount of power that such devices can supply per unit of volume, with watts per cubic meters ($W\ m^{-3}$) stated as its SI unity. Supercapacitors surpasses batteries power density by a factor of about 1000, which combined with the fast charge and discharge response time of just seconds while batteries take a much longer time of 1 to many hours, makes this technology vastly implemented in situations where a burst of power is required. However, storage devices are not entirely classified by energy storage alone, but also from the environmental perspective.

Li-ion batteries, as well as the remaining electrochemical batteries technologies, contains chemical compounds as electrolytes characterized as acid solutions, some more aggravating than others. It is common knowledge that chemical waste must be correctly

separated and disposed which requires specialized services and certified procedures. In the meanwhile, supercapacitors do not share from the same concern as at the end of their lifetime they do not leave considerable hazardous traces as batteries. In addition, the service life of both technologies is very much different, while batteries last for up to 10 years, supercapacitors can reach 15 years. As for their cyclability, which a full cycle concerns a charge and discharge period, supercapacitors can reach values several thousand times as much as batteries.

1.3 Motivation – Surpassing Energy Density and Lifespan Current Rates for Electric Vehicles

With regards to applications for batteries and supercapacitors, a vast amount of possibilities can be described, as a promising one being the electric vehicles (EVs) industry. According to the 2019 annual publication of the International Energy Agency [IEA19a], the expansion forecast for such industry is very much promising as it is expanding in an accelerating pace, when in 2018 the global EV fleet have reached more than 5 million units accounting for 2 million more than 2017. As for Europe, by the end of 2018 were accounted a total of 1.2 million electric vehicles, which represented a growth of about 385 thousand units from the previous year.

According to [BMU09], the so-called electric mobility concerns road or street transportation vehicles of all sorts that are powered by an electric motor and charged throughout the power grid. The initiative encompasses battery electric vehicles (BEV), plug-in hybrid electric vehicles (PHEV), as well as range-extended electric vehicles (REEV), which all can be driven by electric means alone and charged at the power stations. In general, the main goal of electric mobility is to promote the reduction of vehicular CO_2 emissions and independence from fossil fuels.

The EU has presented a great interest in this subject and to do so has shared competences with its Member States [EPRS19]. The most recent step to promote the matter was through local, regional and national incentives expressed as tax reductions and free public parking for EVs. The European strategy for low-emission mobility was published by the Commission in 2016 and emphasized the importance of the public charging infrastructure calling the Member States to review their related taxes as an incentive for lowering emissions, which without an EV faces its autonomy drastically reduced [COM16].

Investments in Energy Storage Technology

According to [IEA19b], after three years of noticeable declining behavior, in 2018 the global energy investment has stabilized and for the third consecutive year power investments have exceeded oil and gas supply. However, as the industry has adopted a more cautious behavior in the past years about changing the energy systems, while directing their efforts to projects representing lower long-term risks and shorter construction times, power sector has faced investment reductions which resulted in a capital declining of about 50% in case of battery storage technologies since 2010. Nonetheless, one must first understand that over the same period the energy storage technologies as well as the majority of renewable energy technologies have evolved in a way that their manufacturing costs have dropped considerably, which means that investments are now more effective as the capital invested has relatively more value. In fact, the very same study presents a very interesting comparison which clarifies the previous statement and demonstrates that when such investments are leveled by 2018 costs a spending ascending trend up to 55% is perceived as shown in (Fig. 09).

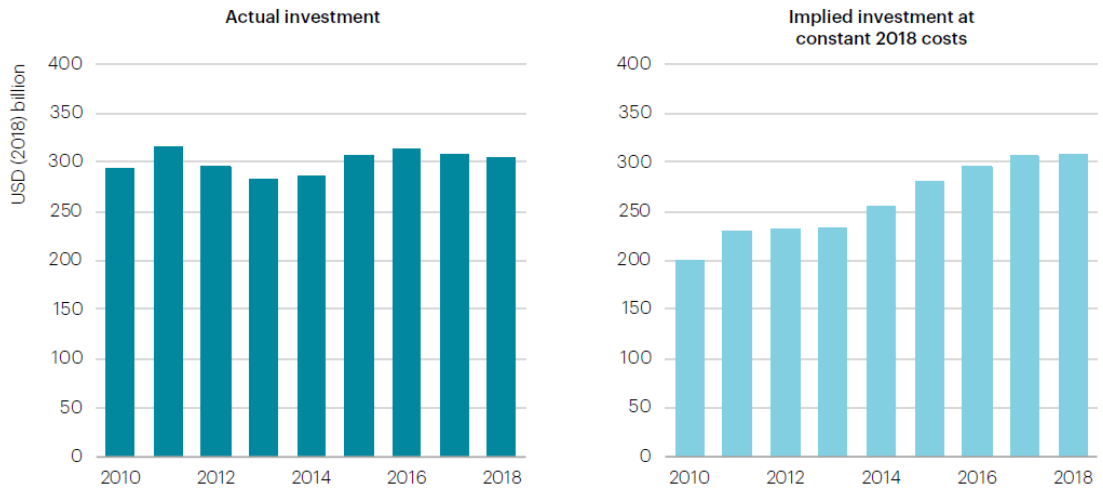

Figure 09 – Investment in renewable power – actual spend vs implied investment at constant 2018 cost levels [IEA19b].

However, the forecasted global high demand for low-carbon power technologies for 2025 to 2030 have demonstrated that the directed investments are not proportional, in fact for

the IEA's Sustainable Development Scenario (SDS) it is required roughly to double the spending in comparison to 2018 [IEA19b].

Therefore, in the pursuit of a greener energy transportation reality financial support is crucial. Regarding this matter the EU provides support through grants from the Connecting Europe Facility (CEF) and the structural investments funds for the development of charging infrastructure. As for research investments, the Horizon 2020 is one of the current possibilities, which is the biggest EU research and innovation initiative accounting with about €80 billion of funding available from 2014 to 2020 [COM19a]. The Commission aims to invest throughout the previously mentioned research programme, a total of €200 million in battery research and innovation from 2018 to 2020 regarding the current long-term contract. As for the upcoming phase, from 2021 to 2027, in June 2018 was proposed by the Commission, which is currently under discussion, to spend about €25 billion of the CEF budget on projects regarding climate matters which includes the expansion and improvement of charging infrastructure [EPRS19].

The European Battery Alliance (EBA) is an initiative started in 2017, led by the Vice President Maroš Šefčovic, which is the result of combined efforts mainly from the EU Commission, interested EU countries and EU Investment Bank. EBA's immediate objective is to get rid of the battery technology dependency from their competitors by creating a more favorable manufacturing value chain for the EU, capitalizing on the development of new technologies, situation which according to some forecasts can lead EU to capture a market share of about €250 billion per year from 2025 onwards. In order to supply the EU batteries, demand alone it is required about 10 to 20 gigafactories, which is the designation for large-scale battery cells manufacturing facilities [COM19b].

With regards to massive Li-ion batteries production, according to [Tesla19b] in 2014 the American electric vehicles manufacturer Tesla has publicly presented the initiative to build the world's first facility of the kind, Gigafactory 1, located in Storey County, Nevada, USA. Having started in the very same year, the unit currently has more 170 thousand m^2 of constructed structure and when taking into consideration the facility's several floors, it accounts for nearly 500 thousand m^2 of operational space. Nevertheless, the structure is still 30% complete and its 2018 manufacturing capability report demonstrated an annualized rate of about 20 GWh. In late 2018, the company started the

construction of its second facility of the kind, Gigafactory 3, located in Shanghai, China [Tesla19a]. However, Tesla's effort and investments on the energy storage market are no limited by batteries production as in early 2019 the company has successfully completed the acquisition of the global leader in supercapacitors manufacturing, Maxwell Technologies [Maxwell19], located in San Diego, California, USA [Tesla19b].

The Interest in Supercapacitors

Supercapacitors, as previously mentioned, are devices which technology provides a relative more efficient energy storage process, in the majority due to their very much faster charging and discharging cycles and greater power density. Such characteristic together with the additional points referred in Section 1.2, have gathered for more than half a decade the global industry and researchers interests with respect to developing a viable substitute to electrochemical batteries [NatGeo13].

In 2006, the government of Heilongjiang province, China, has supported the research and development of the country's first supercapacitor bus [Zhu06]. According to the publication, the intent was to develop an electric bus with supercapacitors as unique energy storage technology. Such research was supported by the device's characteristics and the effects of a daily basis application of such vehicles to society. The proposed bus was suitable for shorter distances up to 20 km autonomy, therefore to city usage only, with its charging time up 15 minutes [Zhu06].

In contrast to China's first supercapacitor bus, the Swiss ABB, a global technology leader company with a diversified market, has presented in 2013 a charging station technology capable of supplying up to 600 kW for 15 seconds, what would completely charge de vehicle [ABB13]. According to [ABB16], the company received in 2016 the first order for their so-called flash-charging technology from TOSA (Trolleybus Optimisation Système Alimentation) electric bus charging infrastructure in Geneva, Switzerland, which was developed by the Swizz vehicles manufacturer Carrosserie HESS in cooperation with ABB itself and intended to supply 12 of their fully electric buses. In 2018 the company received an order from Davos, Switzerland, for their pilot public transportation program set to last the same as the World Economic Forum of the very same year [ABB18].

Under the very same concept, in 2016 the University of Surrey, UK, together with Superdielectrics Ltd. (previous Augmented Optics Ltd.) and in collaboration with the University of Bristol, have announced the development of a novel polymer material with dielectric properties to be implemented as supercapacitors electrolyte which could lead such devices to reach higher energy density rates and to be applied as main source for portable devices to electric vehicles [Bristol16]. In 2018 the very same team made public their material tests data results stating that the new polymer possessed dielectric properties 1 to 10 thousand times greater than the existing electrolyte materials, achieving 4 F cm^{-2} of area normalized capacitance on low-cost metal foil electrodes and up to 20 F cm^{-2} when together with specially treated stainless-steel electrodes [Bristol18].

For supercapacitors technology to gain greater global proportions and acceptance as an individual and self-sufficient energy storage source, there is still a long way to go regarding research and development. Nevertheless, the progress accomplished in the past decade towards that goal is undeniable, with the scientific community interest resulting in more frequent breakthroughs every year.

1.4 Dissertation Outline

1.4.1 Objectives

The aim of this dissertation is to present supercapacitors as a reliable storage technology in order to function in tandem with electrochemical batteries for mobile applications, more specifically as hybrid energy storage system (HESS) for electric vehicles.

Throughout a computational simulation, it is intended to analyze the influence of supercapacitors modules working as complementary energy storage devices to battery packs in a direct parallel configuration. The batteries behavior will be analyzed from three different perspectives: standalone configuration, hybrid battery-supercapacitor storage, hybrid battery-nickel-copper supercapacitor storage.

The intent is to verify if any of these setups can prolong the lifespan of the battery pack by reducing its demand from the system, which would be held by the complementary devices. In addition, the supercapacitors implemented as hybrid storage source are to be compared between each other, as one is defined as a regular commercial model from Maxwell Technologies [Maxwell19], a world market leader, while the second is a

theoretical Ni-Cu electrode [Eugénio13] device calculated and modeled also as part of this work, which its development and theoretical basis is defined in chapter 3.

1.4.2 Dissertation Structure

This dissertation is composed of six chapters which are distributed as follows: introduction; state of the art; supercapacitors theory, calculations and Ni-Cu metallic foam hybrid supercapacitor mathematical and computational modeling; electric vehicles (EVs), electric vehicle modeling; hybrid energy storage system electric vehicle modeling, conclusions and results presentation; conclusions.

In chapter one, the subject is presented as well as the motivations which led to its choice and the objectives which this dissertation aims to achieve.

With regards to the second chapter, it is dedicated to the state of the art encompassing the energy storage systems cutting-edge materials and technologies, as well as their most innovative applications.

The third chapter introduces the supercapacitors technology, for EDLCs, pseudocapacitors and hybrid supercapacitors, as well as the concept of specific surface area (SSA) as target for increasing the device's capacitance, equivalent circuit, laboratorial tests for electrode materials properties analysis, typical equations and the related calculations for converting electrode into cell data. It also includes the mathematical development of a Ni-Cu metallic foam [Eugénio13] implementation as positive electrode for a theoretical hybrid supercapacitor cell, describing the process of gathering dimensional information from a Maxwell 2.3V 300F [Maxwell18a] device to be taken as base for the model, the related calculation describing the data acquisition and the results presentation. Finally, the computational hybrid supercapacitor model is described, which model was made throughout the simulation software Matlab Simulink 2018b.

As for the fourth chapter, it is dedicated to introducing the electric vehicles (EVs) technology, equations, operation, the electric energy supply via hybrid energy storage systems to the vehicle, as well as the EV computational modeling throughout the simulation software Matlab Simulink 2018b.

The fifth chapter is based on [Omar09] and the proposition that a direct parallel connection between batteries and supercapacitors can extend the batteries lifespan. For such, the data collected from [Omar09] were simulated and validated for posterior implementation in the hybrid energy storage system electric vehicle. Finally, it describes the hybrid energy storage system EV computational model, which was modeled throughout the simulation software Matlab Simulink 2018b. The simulation accounted for a variety of physical variables as for real electric vehicles. The model was structured with three different situations as for energy storage sources, battery standalone mode and two hybrid battery-supercapacitor energy storage systems, one with the Maxwell 2.3V 300F PCAP0300 P230 S07 [Maxwell18a] module, and the second with the theoretical Ni-Cu metallic foam electrode supercapacitor cells.

Finally, the obtained results and the relevant findings and conclusions will be presented in chapter six.

1.5 Conclusions

Supercapacitors, as well as EDLCs, are one of the most promising energy storage systems technologies for mobile and several other applications. Such devices properties are very much promising in other to take the energy supply feedback time reduced by a great proportion. With that said, EDLCs are a very promising technology to be applied in a near future as a unique energy storage source for electric vehicles, however some drawbacks must be overcome for this to happen.

Nevertheless, supercapacitors can be of great advantage when implemented in a hybrid storage setup with electrochemical batteries, leading to a smaller demand from these last-mentioned devices, which can lead to a longer lifecycle, advantage that comes to aid solving the environmental discard issue of electrochemical batteries. Besides that, due to supercapacitors great power density this hybridization provides the energy boost characteristic that is not possible by batteries alone.

With regards to overcoming the energy density barriers between both technologies, it is correct to state that the research efforts on new electrode materials is one of the most promising ways to do so. With the same reasoning, it is correct to affirm that taking such materials specific surface area (SSA) characteristic as main research focus, even though

it is not the most effective of them, is still a very promising study subject with very interesting findings presented so far.

Together with EDLCs promises, one can say that electric vehicles (EVs) are a technology yet well stablished, with its market share in an ascending rate but already well defined. The global efforts and incentives let clear that such technology is not just the future but also a solid part of contemporary civilization. However, besides the constant findings that takes their technology manufacturing costs down, the equality to combustion engine vehicles is not yet a fact, which a variety of ongoing researches are attempting to resolve, among them the energy storage systems.

Therefore, with the previous statements in mind, a promising and interesting research subject is presented when taking both technologies together.

CHAPTER 2

State of the Art

This chapter presents the state of the art of supercapacitors technologies as well as their newest applications regarding electrical vehicles. Here are presented the most recent supercapacitors usage as electric vehicles unique or complementary energy storage systems. In completion, newer supercapacitors manufacturing technologies and approaches concerning design, mechanisms and novel materials are mentioned and briefly explained.

2.1 Introduction

The development of novel technologies for electric vehicles and supercapacitors is noticeable, which in the past decade have being reported as several breakthroughs of major importance.

With regards to electric vehicles, this chapter will focus on presenting the most recent supercapacitors applications as individual or complementary energy storage systems for such.

In order to understand the nature of the discoveries, in the case of supercapacitors one must first comprehend the device's characteristics that are susceptible for improvement which can be mainly divided into three main areas: innovative device designs, new findings on mechanisms and material engineering [Wang17].

However, regarding the proposed subject for this dissertation the current section will briefly mention device designs, focusing with more detail on new findings about mechanisms and the engineering of novel materials which are being presented as solutions for supercapacitors improvement.

2.1.1 Electric Vehicles

Even though that at the current technology evolutional state of supercapacitors it is not possible for such devices to replace batteries, a lot has been said about its promising future. Supercapacitors are present in electric vehicles mainly as complementary power source in order to supply the required boost in situations as vehicles acceleration [Horn18]. Among the manufacturers that are already implementing such energy storage system configuration are Hyundai, with the Hyundai Tucson, Chevrolet, with the Chevrolet Equinox and Toyota, with the Toyota FCHV [Carignano17].

As presented in [Zhu06] and in section 1.3, in 2006 the Chinese province of Heilongjiang has supported the development of the country's first supercapacitor bus as unique energy storage source, which clearly can be considered an immense step towards the so commented and expected future of such technology.

2.1.2 Innovative Device Designs

In order to develop new devices, the scientific community is focusing in combining technologies from known devices in order to improve capacitance rates. The redox flow battery (RFB) is a promising energy storage system for large-scale applications due to its high energy efficiency [Menictas14] and was first mentioned by [Thaller76]. While taking the same working principle, [Presser12] has demonstrated that when implementing flowable carbon slurry in electrolytes a capacitive energy storage was made possible, increasing supercapacitors capabilities to be applied for grid purposes, which was then called flow supercapacitor or electrochemical flow capacitor [Wang17].

With regards to energy management, low capacitance aluminum electrolytic capacitors (AECs) are used in order to smoothen the leftover current ripples in alternating current (AC) filters [Wang17]. However, due to their considerable volume such devices are often the largest component in electronic circuits making them an incompatible piece to the increasing miniaturizing trend of wearable electronics [Wang17]. In order to solve this problem, ultrahigh-rate supercapacitors are much more compact and smaller devices which were developed to fit this scenario and are expected to be the future of AC filtering [Sheng12].

Still on the subject of miniaturizing electronics, according to [Kyerematenng17] micro supercapacitors were developed to supply energy storage demands from microdevices having as possible manufacturing processes inkjet printing, screen printing and electrophoretic deposition for integration with the devices, and for *in situ* synthesis the possibilities are laser irradiation, electrode chemical conversion and electrolytic deposition.

As an effective method for increasing EDLCs energy density, the implementation of solvated redox-active species into electrolytes is gathering attention [Wang17]. What occurs is that the resulting aqueous electrolyte provides a pseudocapacitive contribution to the EDL capacitance, which together results in greater energy density rates [Fic12]. It is believed this technique to be of great influence in the supercapacitors research field soon [Senthilkumar13].

Metal ion hybrid supercapacitors are devices that combines the advantages of both supercapacitors and metal ion rechargeable batteries such as Li-ion and Na-ion [Wang17].

This hybrid supercapacitor-battery device results in good rate capability, high energy density, high power output and much longer lifecycles, which makes the metal ion hybrid supercapacitors a potential candidate for the increasing demands of portable devices and electric vehicles industry [Dong19].

2.1.3 Mechanisms

The discovery of new supercapacitors mechanisms concerns in fact the better understanding as well as new findings on how the energy storage occurs in its most subtle aspects. Researchers interests encompasses from the macroscopic interactions to microscopic carrying ions interface with porous electrodes. As for the nature of this dissertation, the main devices taken into consideration in this sector are electric double-layer capacitors (EDLCs).

According to [Wang17], for the past decades, researchers believed that the best approach in order to increase the EDLCs capacitance was to optimize the ions absorption when interfacing with the electrode. Such statement was based on the increase of specific surface area (SSA) of electrode carbon materials which the resulting surface-to-volume ratio, which originates from the high porosity, when applied to (3.3) causes the capacitance to increase. The assumption was that if pores dimensions would decrease so should the capacitance as lesser ions would then enter it due to the lower size, which was stated to measure twice the ions size for an optimum coverage.

However, due to experimentation this last statement, with regards to pores optimum sizes, was negated when the increase in capacitance with the decrease in pores diameters, which sizes were smaller than double of the ions, was reported [Chmiola06]. In fact, there is still not a clear correlation between SSA and specific capacitance specially with regards to pores size when it is now known that the simultaneous increase in both do not result in improvement of specific capacitance. According to [Largeot08], with regards to solvated salts and solvent-free electrolytes, the maximum capacitance for an EDLC was obtained with pore sizes as close as the ions. It was also observed that when the dimensions were increased or reduced, a capacitance drop occurred suggesting that a dimensional correlation between the electrode's pore and electrolyte's ion sizes could be assumed as valid approach when selecting the EDLCs composing materials.

It was demonstrated by [Merlet12] via a microporous carbon electrode model that the electrolyte ions can penetrate sub nanometer pores, which increases the capacitance. This states that carbon nanostructures together with pore sizes play a more important role in the resulting capacitance than previously thought, however, this mechanism remains roughly comprehended. With the same regard, [Jiang11] predicted from a classical density functional theory (DFT) that the capacitance of an ionic-liquid electrolytes inside the electrodes nanopores varies presenting multiples peaks with an exponential decay as the pores sizes diminishes. According to [Hänninen12], the DFT is a quantum mechanical theory used in chemistry and physics in order to investigate the electronic structure of many-body systems such as atoms, molecules and condensed phases.

With regards to quantum-mechanic properties, in the last few years much have being said about such topic and how the respective effects could be implemented to increase the energy storage performance. Regarding such interest, [Ferraro19] describes a quantum supercapacitor mathematical model consisting in two separate chains of electrons and holes, hosted by arrays of double quantum dots (DQDs), model which offers base content for future research and development of cutting-edge devices.

2.1.4 Material Engineering

The most sought focus while developing new materials for supercapacitors energy storage improvement is definitely about novel electrodes. While pursuing a common ideal, researchers' strategies can vary from increasing the traditional SSA throughout new materials to exploring the innovative properties of graphene.

In [Wang17] a variety of electrode materials are quoted, which the ones directed to EDLCs are metal-organic frameworks (MOFs), covalent organic frameworks (COFs), black phosphorous and MXenes. According to [Xia15], MOFs are highly porous materials with a well-defined pore size distribution and high surface areas up to 10 thousand m^2 g^{-1}, are very light and one of the best examples of molecular engineered materials. COFs, as described by [Feng12] are a class of crystalline porous polymers that allows precise integration of organic units at an atomic level to create predesigned nanopores, material which according to [Wang17] were successfully designed by the first time by [Yaghi05] which presented expanded graphitic porous layers, high thermal stability, permanent porosity and high surface areas. Regarding black phosphorous,

[Li14] describes it as a layered material in which single atomic layers are stacked by van der Waals interactions similarly to bulk graphite. Black phosphorous (BP) is a p-type direct-bandgap semiconducting 2D crystal structured material which exhibit rich electronic properties and has shown promising applications as electrode material for energy storage devices including EDLCs [Hao16]. As for MXenes, those two-dimensional materials have opened new possibilities for miniaturized electronics, which are described by [Anasori16] as 2D materials consisting of two to four layers of a transition metal interleaved with carbon layers and which properties such as high conductivity (up to 7000 S cm^{-1}) and hydrophilicity makes them interesting for energy storage applications [Wang17].

In [Raza18] are described a series of promising materials to be applied as EDLCs electrodes, which are carbon-based materials, conducting polymers, metal oxides and composites. With regards to carbon-based materials, [Jayaseelan17] developed mesoporous 3D $NiCo_2O_4$/MWCNT nanocomposite aerogels which reached 1010 F g^{-1} as maximum specific capacitance and very good cyclic stability and within such group of materials for EDLCs electrodes applications there are activated carbon, carbon nanotubes and graphene [Raza18]. As for conducting polymers (CPs), according to [Frackowiak06] are interesting due to their high doping level, fast electrochemical switching and significant capacitance values, the last being improved when such materials are applied in the form of composites with multiwalled carbon nanotubes, with capacitance values ranging from 100 to 300 F g^{-1}.

Graphene based materials are being interestingly implemented as electrodes for supercapacitors presenting much higher performances than commercial devices, however there is still a long financial viability barrier to be overcome [Horn19]. In [Khorasani17] such material is proposed with a nonlinear quantum capacitance design in which the capacitor is formed by a graphene-boron nitride-graphene layered 2D structure. As for [Li19], the publication describes as most recent promising developed materials for supercapacitors electrodes, the all-carbon composites, metal-oxide composites and conducting polymers-carbon. In the all-carbon composites group, the very same paper cites the carbon nanotubes (CNTs) properties as demonstrating high electrical conductivity, great electron transport and electrolyte accessibility, it is also mentioned the interests in graphene for the same application, material which according to [Li19] has an

impressive conductivity and large SSA, however low volumetric capacitance, hard fabrication and commercial production costs are described as disadvantages. Regarding graphene/CNTs materials, [Kim17] describes the development graphene/CNT networks for omnidirectionally stretchable electrodes for supercapacitors aiming to supply the needs of implantable and epidermal electronics, material which presented 152.4 F g^{-1} and 2.9 F cm^{-2} for gravimetric and areal capacitances, respectively. In [Díez18] it is presented the development results for a partially reduced graphene oxide/carbon nanotube composite (prGO/CNT) as films to be implemented as supercapacitors electrodes, presenting interesting values for volumetric capacitance of 250 F cm^{-3} and great retention of 200 F cm^{-3} at 10 A g^{-1}. In [Irwandi16] it was proposed and developed carbon foams throughout fine coal, which the resulting material has presented low density, high strength and temperature tolerance, large external SSA with open cell structure and adjustable thermal and electrical conductivity.

With regards to metallic foams applications as electrodes materials for EDLCs, in [Eugénio13] a team of Portuguese researchers have described the development of Ni-Cu metallic foams throughout the electrodeposition technique resulting in a three-dimensional foam-like structure with promising porosity, which pores have presented a nearly-circular geometry and open dendritic walls. Such material, as mentioned by the very same publication, presented interesting results suitable to be implemented as positive electrodes in supercapacitors and after performing laboratorial tests as cyclic voltammetry (CV) and galvanostatic charge and discharge (GCD) it demonstrated a specific capacitance of 105 F g^{-1} at a current density of 1 mA cm^{-2} and a 90% capacitance retention after 10 thousand cycles at 10 mA cm^{-2}.

2.2 Conclusions

The constant research and development towards new products and technologies can be driven by a variety of motivations, among which profitability and ideological intents. This dissertation brings up a subject that is well fit on such motivational description as green energy is both a necessary and urgent matter as it is financially appealing.

The aforementioned is responsible for unceasing breakthroughs on such subject, presenting society each time with newer outstanding energy storage technologies and increasingly high-tech vehicles. With regards to supercapacitors, their increasing role in

the major energy storage process is prove of such technological evolution, which is certainly directing these devices to reach the much-expected performance where they could be implemented as main storage source.

Therefore, it is safe to say that with the non-resolving energetical scenario regarding our current approach and its harmful consequences, newer technologies will continue to be presented in the pursuit of greener and more effective energy storage devices, which will certainly drive or be driven by such expanding global market share.

CHAPTER

3

Supercapacitors – Concept and Application

This chapter presents an introduction to Supercapacitors technology, with a specific focus on hybrid supercapacitors. Such devices are then deepened explained, from their historical background, technology, structure and operation. In relation to such technology, the property called Specific Surface Area (SSA), which is intrinsic to the porous electrodes, is introduced. For a better understanding of the theoretical operation of supercapacitors, the electric equivalent circuit is presented and explained. Also, the laboratorial electrodes tests, GCD and CV, are presented and briefly explained. The mathematical approaches typically used for supercapacitors properties calculations as well as the development of the equations used to convert laboratorial tests data into proper cells values. Finally, the mathematical and computational modeling of the theoretical Nickel-Copper hybrid supercapacitor is presented.

3.1 Introduction

Electrostatic capacitors (Fig. 3.1), also called parallel plate capacitors, are designed to store electric energy predominantly throughout electrostatic fields. Stating this characteristic to such devices classifies them as direct energy storage devices, which means that there are no intermediate conversion processes from any other form of energy to an electrical output [Conway99].

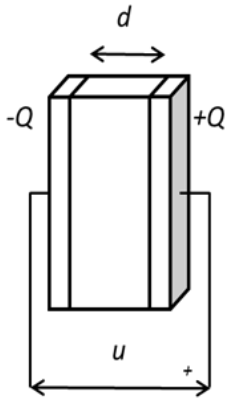

Figure 3.1 – Electrostatic capacitor [Grbovic13].

In order to store energy, an electric potential difference (ΔV) is imposed over the system throughout and external voltage source. During this process the electrons, which have a negative charge, are pulled from the positive electrode, towards the negative, i.e., electric current. When it occurs, the potential difference on such plate increases and the electrons tend to seek balancing the system by returning to the uneven plate throughout a conductor medium, what is made impossible once the conducting channel is interrupted. The electric charge is then accumulated on the electrodes (3.1) [Béguin13].

$$Q = CV\ [C] \tag{3.1}$$

As the electrodes are extremely close to each other, a physical division is required in order to avoid contact between plates, which could lead to a short-circuit and instant transfer of charge. Such separation is called dielectric and can be implemented only by pulling plates apart, leaving air as insulating medium however, its permittivity is rather small. In order to increase such variable, dielectric materials with higher dielectric constants (ε) are implement into the system. Such materials play an important role in capacitors operation, most specifically in the buildup of the device's energy storage capability, the capacitance.

While avoiding contact between electrodes, the existing potential difference occurring on the plates attracts the separator's ions towards its opposite, which polarizes the material. The capacitance formula for a parallel plate capacitor relates the dielectric constant of both the free space (ε_0) and dielectric material (ε_r), the surface contact area of one electrode (A) and the dielectric thickness (d) (3.3) [Béguin13].

$$C = \frac{Q}{V}\ [F] \tag{3.2}$$

$$C = \frac{\varepsilon_r \varepsilon_0 A}{d}\ [F] \tag{3.3}$$

However, the electrostatic capacitors capability does not meet the requirements for most of the high demand storage applications. Aiming to apply such technology to applications of massive storage needs, electrolytic and electrochemical capacitors were developed, which both combine electrochemical characteristics. Electrolytic capacitors are often manufactured with aluminum (Al), tantalum (Ta) or ceramics [Jayalakshmi08], which its cell structure is defined as having an electrolyte, liquid or solid, generically performing as one of the electrodes, more specifically the cathode, while a metal plate forms the second one, while a metal oxide, which is produced as result of a voltage applied to the metal plate, behaves as dielectric material due to its small thickness, parameter defined by the voltage range applied [Venkataraman15]. Electrochemical capacitors (ECs), so-called supercapacitors, also take advantage of the electrolyte properties to store energy. ECs are different from the other capacitors no just regarding its structure but especially due to its far greater capacitance (F) and energy density ($J\ m^{-3}$) values. Mainly, these devices are divided in four different groups: high voltage ceramic capacitors, pseudo-capacitors, electric double layer capacitors (EDLC) and hybrid supercapacitors (Fig. 3.2).

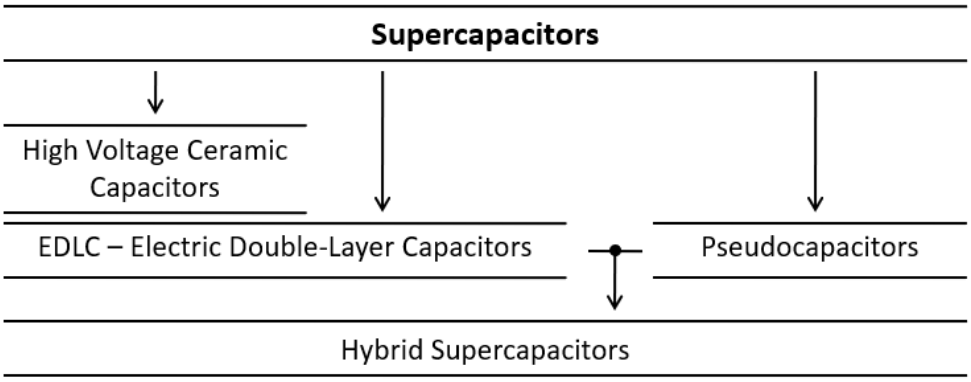

Figure 3.2 – Supercapacitors taxonomy [Grbovic13].

High voltage ceramic capacitors are basically formed from two parallel sheets of electrodes, from metallic of metal-like properties, as for the dielectric material a ceramic layer is placed in between. The middle layer is often made of titanium dioxide (TiO_2) or barium titanate ($BaTiO_3$), however its composition can vary according to the intended characteristics to specific applications. In order to obtain higher capacity values, ferroelectric materials are insert into the ceramic's composition together with specific oxides. Such capacitors are classified in two groups: monolithic and disk type [HEC08].

The electric double layer capacitors (EDLC) are composed of two opposite electrodes which are often made of carbon related materials or other high porous compounds, an electrolyte solution between electrodes and a separator material in the middle. For each electrode, a parallel single layer of electrolyte's ions is formed, and only a few angstroms distant from the electrode's surface. This configuration forms a structure which behavior resembles a parallel plate capacitor, in which the electrolyte layer in between acts as a dielectric, making possible for the charge to be accumulated [Grbovic13].

As for pseudocapacitors, their configuration can be defined as a hybrid between batteries and EDLCs. The structure is mostly the same as electric double layer capacitors, however, the charge storage is made possible by reduction-oxidation (redox) reactions as it happens with batteries [Venkataraman15]. Therefore, the known materials implemented as pseudocapacitors electrodes are conducting polymers and transition metal oxides and sulphides [Upadhyay17], as Ni-Cu metallic foams in [Eugénio13].

Finally, hybrid supercapacitors are generically a combination between EDLCs and pseudocapacitors, which the resulting device retains their best characteristics, presenting higher specific capacitance regarding both technologies [Muzaffar19]. As result of such combination, the applicable materials for such devices encompasses the very same redox and EDLC materials implemented in pseudocapacitors and electric double-layer capacitors [Béguin13]. The combination of two different electrodes often results in a better electrochemical outcome [Muzaffar19].

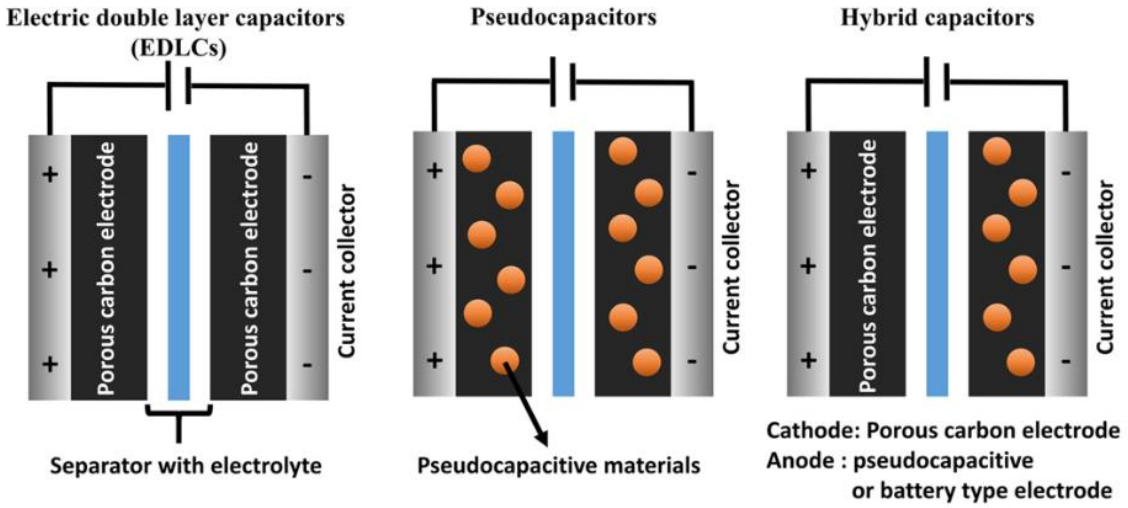

Figure 3.3 – EDLCs, pseudocapacitors and hybrid supercapacitors [Yoon16].

3.2 Hybrid Supercapacitors

Regarding the energy storage scope of this dissertation, which is defined as the implementation of Ni-Cu metallic foams as positive electrodes for supercapacitors, the respective device structure would be hybrid supercapacitors.

As described by [Muzaffar19] and previously mentioned in section 3.1, hybrid supercapacitors are indirect storage devices that combines the storage technologies of both electric double layer capacitors and pseudocapacitors, encompassing their very best characteristics and providing a balance of the system regarding deficiencies or disadvantages from both technologies, i.e., the limiting properties of one is not present in the other. As mentioned by [Béguin13], hybrid supercapacitors were developed in order to take the energy density level of EDLCs up to 20-30 Wh l^{-1} which nowadays stands at 5-10 Wh l^{-1}.

According to [Grbovic13], pseudocapacitors are defined as electrochemical energy storage devices, generically constituted of two opposite conducting electrodes, symmetrically or asymmetrically assembled, which are immersed in an electrolyte solution (Fig.3.4). The device, as such as other capacitors, possesses a porous membrane called separator that acts as an insulator, positioned between both electrodes. This middle layer main purpose is to avoid contact between both sides, as such as in cases of oxidation, when dendrites are formed during charge/discharge cycles by the sprouting of the active material. These commonly called whiskers, are formed during numerous charge and discharge cycles, with a particular increasing rate when the cyclability happens rapidly, which reduces the device's efficiency and in case of interaction with its counterpart can lead to a short circuit, what causes the device to heat and possibly ignite [May18]. The pseudocapacitive electrode behavior is defined as faradaic, i.e., the charge is stored by chemical means, in which the electrons transfer occurs across the electrode's interface [Conway99] and is made by reduction-oxidation (redox) reactions means [Venkataraman15].

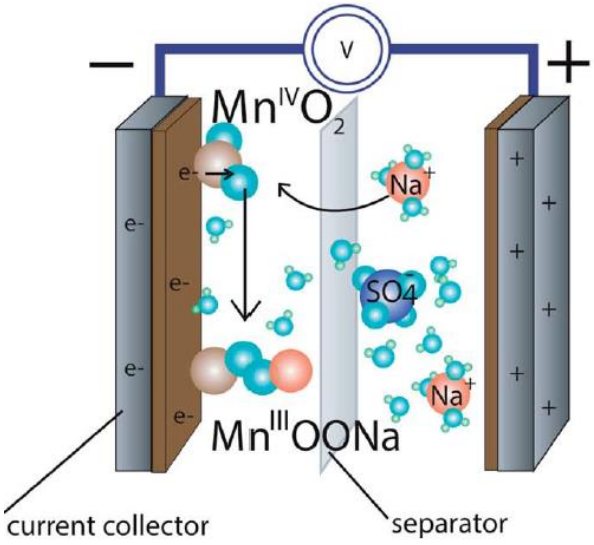

Figure 3.4 – Pseudocapacitor structure [Jost14].

The device's electrode which behaves as EDLCs is carbon-based and during the charging process forms the accretion of electrolyte molecules and charged ions to the electrode's walls, which generates an ordinary capacitor like structure (Fig.3.5) [Conway99]. Just like the typical capacitors, this resulting structure has an equivalent dielectric separator which here is characterized by a electrolyte molecular monolayer that surrounds the

electrode's inner walls, the so-called "inner Helmholtz plane" (IHP), which its diameter poses as the equivalent dielectric thickness (*d*). In completion of this analogy, the charged carrying ions attach themselves to the IHP, behaving as the opposite electrode, which originates the so-called "outer Helmholtz plane" (OHP), therefore the analogous capacitor structure [Grbovic13].

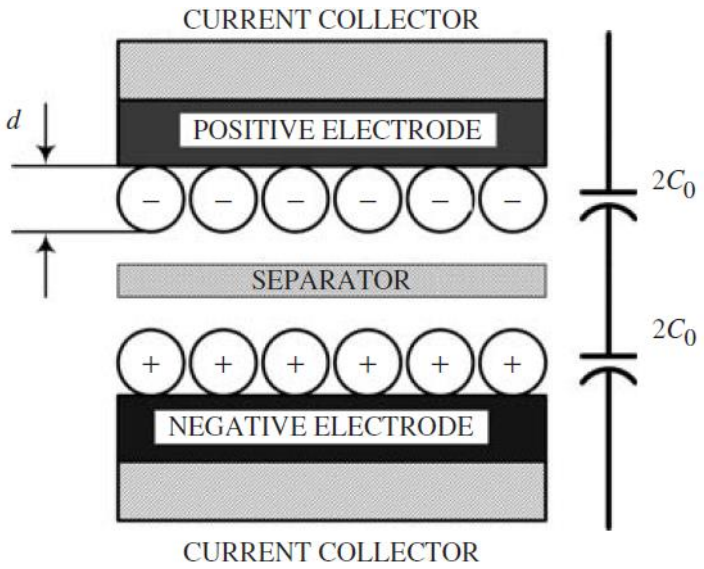

Figure 3.5 – EDLC internal structure [Grbovic13].

3.3 Porous Materials as Electrodes

As described by [Qu14], surface area, pore size and size distribution play an important role in the viability of a suitable candidate for a porous electrode, therefore, porosity is one of the most important factors when designing such materials.

According to [Sing85], the International Union of Pure and Applied Chemistry (IUPAC) classification of pore size is defined as macropores, larger than 50 nm, mesopores, between 2 and 50 nm, and micropores, smaller than 2 nm (Fig.3.6).

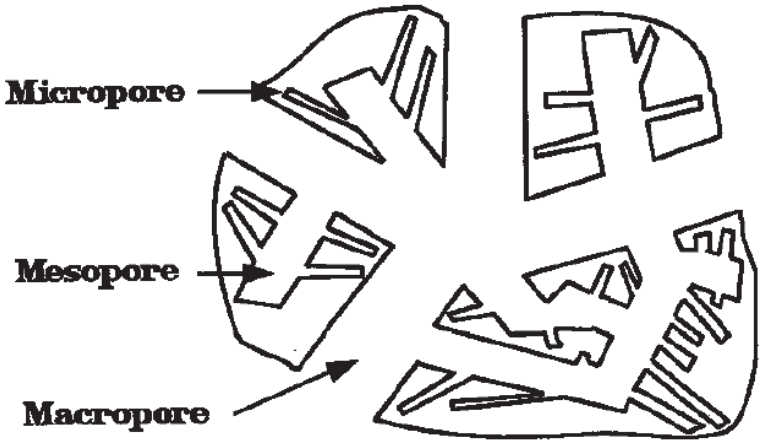

Figure 3.6 – Pore size classification [Qu14].

Nanoporous metallic foams (NMFs), as described by [Eugénio13], are typically three-dimensional structures of interconnected particles which exhibit a porosity of not less than 50% and their sub-micron pores contribute to the specific surface area pores [Tappan10]. NFMs allow the fast diffusion of active species through the material and provide an increase in specific surface area [Eugénio13].

Such materials have been sought in the pursuit of suitable high-surface-area electrodes, which combines properties of metals and nanoarchitectures [Tappan10]. Therefore, the Ni-Cu metallic foam developed by [Eugénio13] is in accordance with such statements, which makes it an interesting candidate for such applications.

3.4 Specific Surface Area - SSA

According to [Amador16], the specific surface area (SSA) is a function of porosity, pore size distribution, shape, size and roughness. In [Porter12] the porosity is described as a ratio between the pore volume and the total volume of a material. The very same publication mentions three primary types of porosity: interganular, joints-fissures, vugular. The intergranular porosity is described by [Porter12] as occurring when pores are formed as spaces between grains or particles in compacted material. While for joints-fissures, also called fractures, the type is attributed to pores formed by fractures in a fine net configuration. Finally, the author defines the vugular porosity as big irregular pores formed due to dissolution of material.

For a better understanding of the SSA concept, based on [BEL19], a simplified geometry (Fig.3.7) such as a cube can be assumed as representing either the base material or the respective particles after subdivision. The scheme represents the increment in surface area (SA) while subdividing the same volume of material, which is obtained by the product of the total surface area of the geometry and the number of resulting particles.

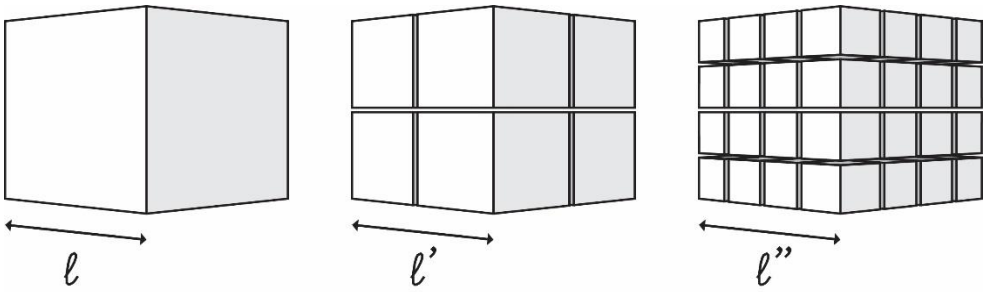

Figure 3.7 – Specific surface area.

The SSA (3.4) is then obtained when the total surface area is divided by the mass of the solid (m_s), therefore assigning a proper material is required, which in supercapacitors is represented by the electrode's active material.

$$SSA = \frac{total\ SA}{m_s}\left[\frac{m^2}{g}\right] \tag{3.4}$$

Supercapacitors electrodes are manufactured from a variety of materials, most commonly carbon based [Svasta17], such as activated carbon and carbon nanotubes. In order to transfer electrons, the electrolyte's carrying ions require a contact surface area for the interaction to occur, thus, as bigger the active material's contact surface area more ions can interact, therefore, greater capacitance values are made possible [Purkait18]. Typically, porous materials are implemented as supercapacitors electrodes which SSA provides the larger contact area needed for high-performance devices.

The theoretical assumption, according to the model proposed by [Stern24], was that all the porous provided by the electrode were dimensionally homogeneous, therefore, providing the same ionic penetration parameters. In reality, as described by [Grbovic13], the pores sizes varies, thus, not all of them can be equally occupied regarding their total depth which causes an ionic irregular penetration rate leading to the conclusion that small porous, regarding the ions average diameter, are not populated (Fig.3.8).

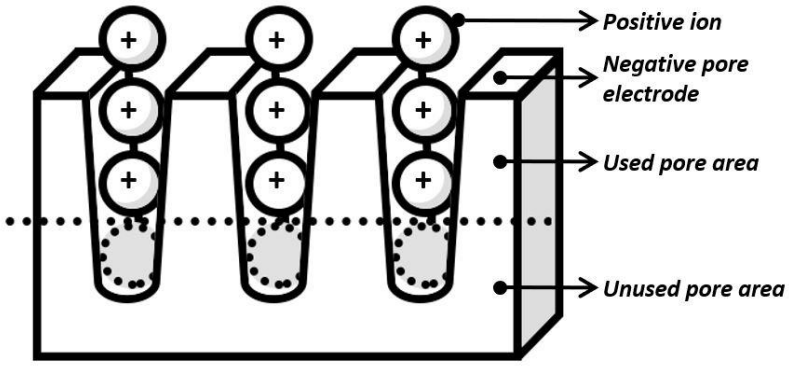

Figure 3.8– Pores non-uniform distribution [Grbovic13].

As described by [Wang17], for decades it was believed that the best approach in order to increase the supercapacitors capacitance was to optimize the ions absorption rates when the double-layer was formed and the resulting interface with the electrode porous structure occurred. The statement is based on the relation of contact area in supercapacitors capacitance equation (3.3), in which the increase of specific surface area (SSA) of active materials results in higher surface-to-volume ratios causing the volumetric capacitance to increase [Wang17]. Thus, the understanding is that with pores dimensions decreasing the absorption rates are therefore affected as a smaller number of ions can interact with the active material due to the reduced pores sizes.

3.5 Electric Equivalent Circuit

3.5.1 Theoretical Model

According to [Grbovic13], the supercapacitor's macro model is used for conversion systems control analysis and design, temperature and losses evaluation for different operating modes. As hybrid supercapacitors encompasses both EDLCs and pseudocapacitors technologies, the respective equivalent circuit can be designed as being composed of two electrodes, one for the double-layer capacitance and a second for faradaic capacitance electrodes (Fig.3.9).

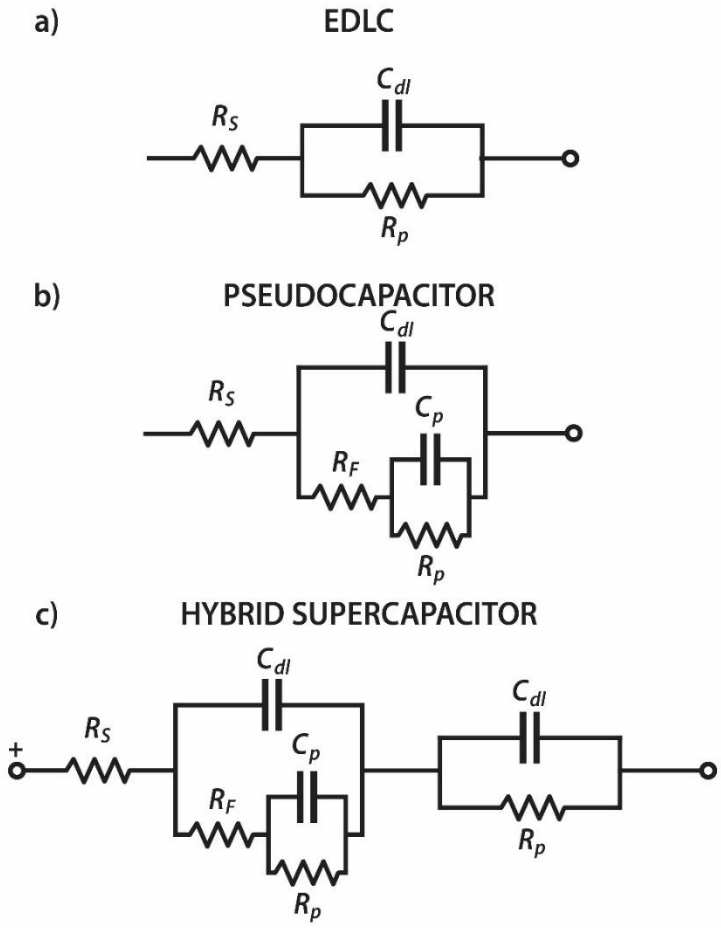

Figure 3.9 – Equivalent circuits of EDLC, pseudocapacitor and hybrid supercapacitor [Béguin13, Fisher13, Venkataraman15].

Where C_{dl} represents the double-layer capacitance, R_P stands for Faradaic charge transfer resistance, C_P for pseudocapacitance, R_F is electrode/electrolyte resistance and R_S is defined as series resistance which in this model represents the combined resistances of electrolyte, electrode and current collectors [Béguin13, Fisher13, Venkataraman15].

Both the EDLC and pseudocapacitor equivalent circuits are the simplified representation of much more complex branches which takes into consideration the electrode's pores (ideal or not) [Kim11] capacitances and resistances representing the double-layer interaction, as generically demonstrated in (Fig.3.10). Such model is composed by a serial N^{th} order connection of a single *RC* leader network, which can resemble either EDLCs or pseudocapacitors circuits [Grbovic13].

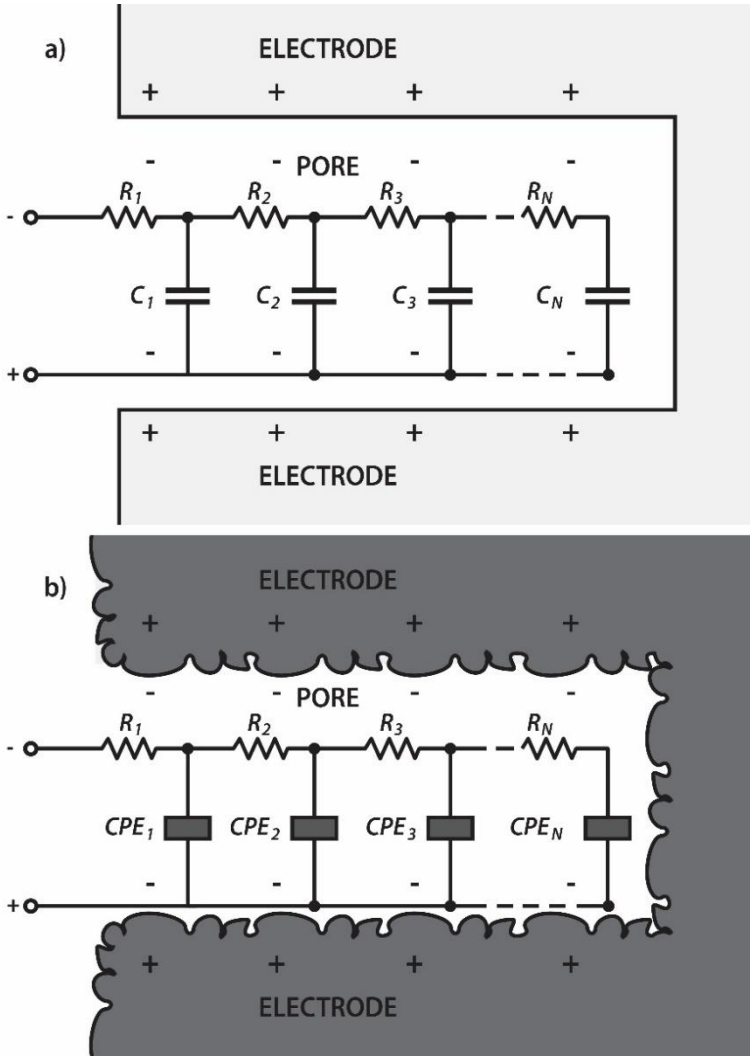

Figure 3.10 – Equivalent circuit electrode pore a) ideal, b) non-ideal [Kim11].

According to [Béguin13], in pseudocapacitors equivalent circuit the faradaic impedance (Z_P) has to be taken into consideration which is represented in the model by C_P in series with R_P (Fig.3.9b). With regards to EDLCs, [Conway99] describes its macroequivalent circuit design emphasizing the correspondence to the real device's structure by the equivalent components implemented.

However, when representing general real electrochemical systems, the proper correspondence from its properties to a mathematical model is not often possible due to the inconsistency of the transposed information between models, as some of the information regarding physicochemical processes involved may be lost or distorted [Torres17]. According to [Kakaei18], capacitances when in solid electrode/electrolyte interfaces are often not purely capacitive, presenting frequency dispersion that due to

behavior incompatibilities cannot be represented as simple capacitors [Jorcin06]. Such cases require a simple distributed circuit element as the constant phase element (CPE) (Fig.3.11), which its function was introduced by [Fricke09] and [Cole41] and is widely used for situations of this very same nature [Torres17].

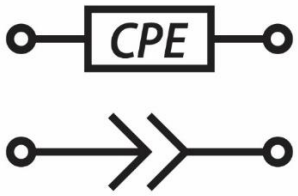

Figure 3.11 – CPE element [Kakaei18, Hosseini15].

The impedance for CPE (Z_{CPE}) is expressed as in (3.5) [MacDonald84, Parigi13, Torres17].

$$Z_{CPE} = \frac{1}{T(j\omega)^{\beta}} \ [\Omega] \tag{3.5}$$

Where T (F $cm^{-2}s^{\alpha-1}$) stands for the CPE parameter, β represents the CPE exponent with values set in the range of $0 < \beta < 1$, j is the imaginary number, ω is the angular frequency [Jorcin06, Torres17]. When β =0, T presents conductance behavior, as for β =1, the behavior is defined as an ideal capacitor and when β = -1 it behaves as an inductor [Parigi13, Torres17]. As described by [Parigi13], at ω= 1 rad s^{-1} (0.159 Hz), the impedance magnitude is set as $|Z|=1/Q$, therefore, from experimental impedance data, the value of Q is then defined as 0.0064 s^{β}/Ω.

The impedance for the CPE can be calculated from (3.6), which possess two independent parameters, α and β. When β=1, α has the dimensions admittance, as for β=0, α behaves as a resistance, otherwise the value of Q is defined as Ω/s^{β} [Parigi13].

$$Z_{CPE} = \frac{\alpha}{s^{\beta}} \ [\Omega] \tag{3.6}$$

When β=0.5, the exponent is referred as a Warburg impedance element (Fig.3.12), Z_{CPE}= Z_W, which definition was presented the German physicist Emil Warburg in 1899 and it is an equivalent circuit component which is implemented to model diffusion processes of ionic species in dielectric spectroscopy [Huang18, Metrohm11].

Figure 3.12 – Warburg element [Metrohm11].

The independent parameter α is defined by (3.7).

$$\alpha = \frac{RT}{\sqrt{2}n^2FA}\left(\frac{2\times10^3}{C_0\sqrt{D_C}}\right) \tag{3.7}$$

Where R stands for the gas law constant of 9.314 $J\ Kmol^{-1}$, F is the Faraday's constant of 96485 $C\ mol^{-1}$, n is defined as the number of electrons exchanged set to 1, T is the absolute temperature defined as 298 K, A is the electrode area defined in cm^2, the electrolyte concentration is C_0 defined as 1 $mol\ L^{-1}$ and D_C is the ion diffusion constant [Parigi13].

When considering a semi-infinite diffusion layer, Z_W is defined as (3.8), while for a finite assumption Z_W is modelled as (3.9).

$$Z_{W,s.i} = \frac{1}{Y_0\sqrt{j\omega}}\ [\Omega] \tag{3.8}$$

$$Z_{W,f} = \frac{1}{Y_0}\tanh\left(B\sqrt{j\omega}\right)\ [\Omega] \tag{3.9}$$

Where Y_0 is the diffusion admittance and B is defined by (3.10).

$$B = \frac{\delta}{\sqrt{D}} \tag{3.10}$$

Where δ is the diffusion layer thickness and D stands for the diffusion coefficient.

The Warburg impedance has as definition identical values for real and imaginary contributions which defines the phase angle at 45º [Metrohm11].

The impedance function definition for the supercapacitor CPE equivalent circuit (Fig.3.13) is presented in (3.11).

$$Z(w) = Z'(w) - jZ''(w) \tag{3.11}$$

Where Z' and Z'' are defined in (3.12) and (3.13), respectively.

$$Z' = R_e + \left[\frac{\frac{R_C}{w^2 C_1^2} + \frac{\alpha w^{-(\beta+2)}}{C_1^2} \cos\left(\frac{\pi\beta}{2}\right)}{R_C + \frac{1}{w^2 C_1^2} + \alpha^2 w^{2\beta} + 2\alpha w^{-\beta}\left(R_C \cos\left(\frac{\pi\beta}{2}\right) + \frac{1}{wC_1}\sin\left(\frac{\pi\beta}{2}\right)\right)} \right] \tag{3.12}$$

$$Z'' = -\frac{\left[\frac{R_C^2}{w^2 C_1} + \frac{\alpha^2 w^{-(2\beta+1)}}{C_1} + \frac{2\alpha R_C w^{-(\beta+1)}}{C_1}\cos\left(\frac{\pi\beta}{2}\right) + \frac{\alpha w^{-(\beta+2)}}{C_1^2}\sin\left(\frac{\pi\beta}{2}\right)\right]}{\left[R_C + \frac{1}{w^2 C_1^2} + \alpha^2 w^{-2\beta} + 2\alpha R_C w^{-\beta}\cos\left(\frac{\pi\beta}{2}\right) + \frac{2\alpha}{C_1} w^{-(\beta+1)}\sin\left(\frac{\pi\beta}{2}\right)\right]} \tag{3.13}$$

From (3.7) it is possible to determine the magnitude of α, D_C is found by rearranging (3.6) with (3.7) together with the supercapacitor's cell parameters.

Based on [Rakhi14] hybrid supercapacitor equivalent circuit, [Darowicki17] fuel cell CPE model, [Fisher13] pseudocapacitor equivalent circuit representation, the CPE equivalent circuit for a Li-ion battery from [Westerhoff16], the equivalent circuit for an oxide film electrode in [Pan98] and (Fig.3.9), the CPE equivalent circuit for a hybrid supercapacitor is described in (Fig.3.13).

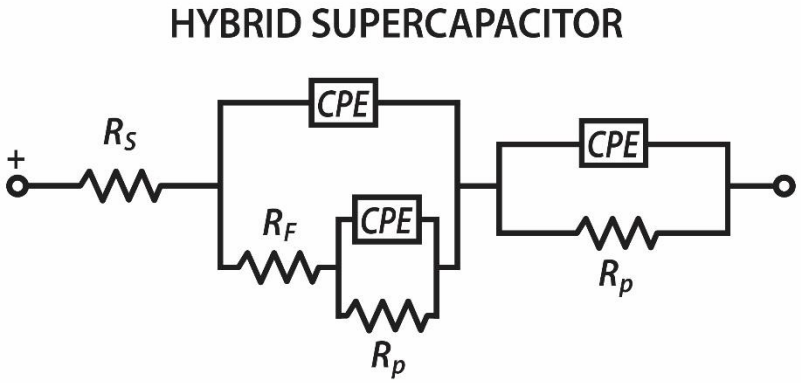

Figure 3.13 – CPE equivalent circuit for hybrid supercapacitor [Westerhoff16, Béguin13, Fisher13, Venkataraman15].

The electrode's laboratorial tests and manufacturing procedure, cyclic voltammetry (CV), galvanostatic charge and discharge curves (GCD) and electrodeposition, are described in annex 5.

3.6 Electrodes and Cells Associated Expressions

3.6.1 Typical Equations

The equations used to perform calculations for supercapacitors are based on the parallel plate capacitor's formula for capacitance (3.3). As an equivalent structure is formed in the double-layer interactions [Grbovic13] and the storage mechanism in both devices, in an ideal case, is purely electrostatic with a current independent of the voltage, the general formula to calculate the ideal supercapacitors cell capacitance (3.14), which has constant proportion, is obtained from (3.2) [Roldán15].

$$C_{cell} = \frac{\Delta q}{\Delta V} = cte\ [F] \tag{3.14}$$

Where C_{cell} stands for the cell capacitance, q is the charge and ΔV the voltage.

However, the cell capacitance is best determined from the related GCD cell capacitance formula (3.15), which takes into consideration the discharge current curves [Allagui16] and can be rearranged (2.16) based on [Roldán15].

$$C_{cell} = \frac{I}{\left(\frac{dV}{dt}\right)}\ [F] \tag{3.15}$$

Where I stands for the discharge current, dV/dt as the slope of the time-voltage curve, also called scan rate (υ) [Stoller10].

$$C_{cell} = \frac{i.\Delta t}{\Delta V}\ [F] \tag{3.16}$$

Where i stands for the current density, Δt is the time and ΔV the voltage.

The cell specific capacitance is defined as the device's total capacitance in relation to its active material mass, which SI unit is defined ($F\ g^{-1}$). Based on that and throughout the capacitance equations (3.14-3.16), the general formula for specific capacitance (3.17) can be obtained.

$$C_{sp,cell} = \frac{I.\Delta t}{m_{total}.\Delta V}\left[\frac{F}{g}\right] \tag{3.17}$$

Where $C_{sp,cell}$ states for the specific capacitance of the cell and m_{total} is the total mass of both active materials (electrodes) [Roldán15].

With regards to the equivalent series resistance (*ESR*), according to [Béguin13], it is deduced by the voltage drop (V_{drop}) (Fig.3.14) in a GCD, which occurs over the current inversion (Δi) and is obtained by (3.18).

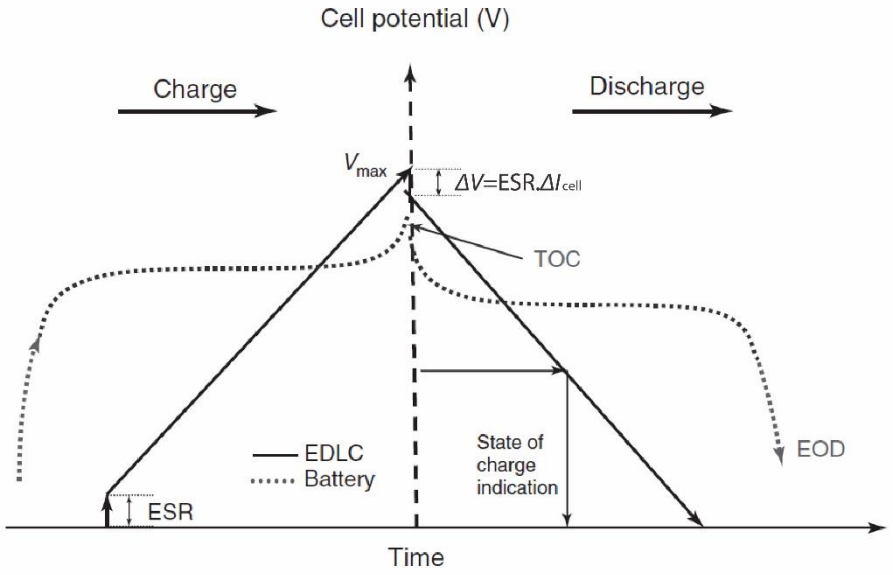

Figure 3.14 – Equivalent series resistance identified in GCD [Béguin13, Vicentini19].

$$ESR = \frac{V_{drop}}{\Delta I} = \frac{\Delta V}{\Delta I}\ [\Omega] \tag{3.18}$$

The maximum energy stored (*E*), as described by [Béguin13], is given by (3.19) and stated in joules (*J*). As for a more usual convention, *E* can be defined in watt-hour (*Wh*) (3.20).

$$E = \frac{CV^2}{2}\ [J] \tag{3.19}$$

$$E_1 = \frac{\left(\frac{1}{2}CV^2\right)}{3600}\ [Wh] \tag{3.20}$$

The energy density (*U*) is defined by the relation of energy and the device's total mass (m_{cell}) [Maxwell18a].

$$U = \frac{E_1}{m_{cell}}\left[\frac{Wh}{kg}\right] \tag{3.21}$$

With regards to power (*P*), it can be obtained by (3.22), which is stated as power density ($W\ kg^{-1}$) when in relation to the device's total mass (3.23).

$$P = \frac{E_1}{\Delta t}\ [W] \tag{3.22}$$

$$P = \frac{E_1}{\Delta t . m_{cell}}\ \left[\frac{W}{kg}\right] \tag{3.23}$$

3.6.2 From Electrode to Cell Data

In order to transpose laboratorial data into approximate real values so a device can be modeled and simulated, a correct interpretation of basic equations is required [Roldán15]. For this, the test procedure from which the specific capacitance was measured as well as the prototype cell electrode configuration must be known due to each technique particularities.

For cyclic voltammetry (CV) technique, the test result, called voltammogram, displays a characteristic curve of the imposed varying electrochemical potential (E^0) between two voltage limits, which evolves in accordance to the scan rate (υ) resulting in a current (I) profile, as displayed in Annex 5, A5.2 [Béguin13].

For galvanostatic charge and discharge curves (GCD) method, the test result, as mentioned in annex 5, A5.3, displays the charge and discharge characteristics of a certain species subjected to an imposed current density (i), a determined voltage (V), whether positive or negative, against time (t) [Béguin13].

Therefore, specific capacitance formula can be adapted regarding the nature of available data, whether it is CV of GCD derived.

The scan rate (υ) is characteristic from voltammograms, which its SI unit is defined in mV/s and it determines the speed of linear potential variation during the test [Elgrishi18]. Thus, the general specific capacitance formula for CV tests (3.25) can be adapted from (3.15) [Roldán15].

$$C_{sp,CV} = \frac{i}{m\left(\frac{dV}{dt}\right)}\ \left[\frac{F}{g}\right] \tag{3.24}$$

$$C_{sp,CV} = \frac{i}{m . \upsilon}\ \left[\frac{F}{g}\right] \tag{3.25}$$

Where *m* states for the mass of active material depending on the test nature and calculation intent. The mass correlation is defined as (3.26) for asymmetric cells.

$$m_{total} = m_{+} + m_{-}\ [g] \tag{3.26}$$

For GCD, no adaptation is necessary as (3.16) requires the same data as provided by such test results.

In order to define the specific capacitances equations for both symmetric and asymmetric configurations, firstly, the correlation between cell and both electrodes capacitances must be defined. As described in [Roldán15], such correlation can be defined as a series equivalent circuit (3.27), consisting of two electrode-electrolyte interfaces represented as single capacitors C_{+} and C_{-} for the positive and negative electrodes, respectively [Ratha18].

$$\frac{1}{C_{cell}} = \frac{1}{C_{+}} + \frac{1}{C_{-}}\ \left[\frac{1}{F}\right] \tag{3.27}$$

With regards to each electrode's capacitance, if the configuration is symmetric, it will be defined as (3.28):

$$C_{elec} = C_{+} = C_{-}\ [F] \tag{3.28}$$

Therefore, from (3.27), (3.29) is obtained.

$$C_{cell} = \frac{C_{elec}}{2}\ [F] \tag{3.29}$$

This equation is in accordance with [Stoller10] and [Conway03] which stated that with regards to a symmetric device's capacitance, each electrode necessarily defines half of it, which generates a reciprocal relation between the total capacitance of the device and that of a single electrode.

However, for an asymmetric configuration such statement doesn't apply due to both electrodes being different. Therefore, in an asymmetric EDLC configuration (as well as for symmetric) the respective relation is defined by (3.30), however, in hybrid supercapacitors it is defined by the electrode with smaller capacitance (if $C1 >> C2$, $C_{cell} \approx C2$) [Eliaz19].

$$C_{cell} = \frac{C_+ . C_-}{C_+ + C_-} [F] \tag{3.30}$$

Following the stated in [Eliaz19], as the grater capacitance is not predefined as either positive or negative, *C1* and *C2* are hereafter defined as $C_{elec}{}^{c>}$ and $C_{elec}{}^{c<}$, respectively. Consequently, C_{cell} is defined as (3.31).

$$C_{cell} = C_{elec}{}^{c<} [F] \tag{3.31}$$

Therefore, with regards to asymmetric cells, the specific capacitance can be obtained from (3.32-3.33), taking into consideration the total mass (m_{total}) of both active materials.

$$C_{sp,asymm.cell} = \frac{C_{cell}}{m_{total}} = \frac{C_{cell}}{m_+ + m_-} \left[\frac{F}{g}\right] \tag{3.32}$$

$$C_{sp,asymm.cell} = \frac{C_{elec}{}^{c<}}{m_+ + m_-} \left[\frac{F}{g}\right] \tag{3.33}$$

Based on (3.31) and (3.33) it is possible to correlate the cell's specific capacitance to the specific capacitance of $C^{c<}$ by considering the cell's total mass as a sum of $m^{c>}$ and $m^{c<}$, defined by (3.34-3.37).

$$\frac{C_{cell}}{m_{total}} = \frac{C_{cell}}{m^{c>} + m^{c<}} = \frac{C_{elec}{}^{c<}}{m^{c>} + m^{c<}} \left[\frac{F}{g}\right] \tag{3.34}$$

$$\frac{C_{cell}}{m^{c>} + m^{c<}} * \frac{1}{m^{c<}} = \frac{C_{elec}{}^{c<}}{m^{c>} + m^{c<}} * \frac{1}{m^{c<}} \left[\frac{F}{g}\right] \tag{3.35}$$

$$\frac{C_{cell} * (m^{c>} + m^{c<})}{m^{c<} * (m^{c>} + m^{c<})} = \frac{C_{elec}{}^{c<}}{m^{c<}} = C_{sp.elec}{}^{c<} \left[\frac{F}{g}\right] \tag{3.36}$$

$$C_{sp.elec}{}^{c<} = \frac{C_{cell}}{m^{c<}} \left[\frac{F}{g}\right] \tag{3.37}$$

From the equations above it is possible to stablish a relation between two (C_{cell}) and three-electrodes (C_{elec}) results for specific capacitance.

3.7 Modelling of a Nickel-Copper Supercapacitor

In order to model the theoretical Ni-Cu foam hybrid supercapacitor it was required an appropriate basis of comparison regarding optimal dimension, materials and weight.

Therefore, a Maxwell pseudocapacitor cell of reference PCAP0300 P230 S07, 2.3 V, 300 F [Maxwell18a] was chosen as basepoint for the generic cell volumetric modelling.

3.7.1 Generic Geometry of a Supercapacitor

The dimensional information was obtained from the chosen Maxwell pseudocapacitor datasheet [Maxwell18a] as presented in (Fig.3.15) (Table 3.1).

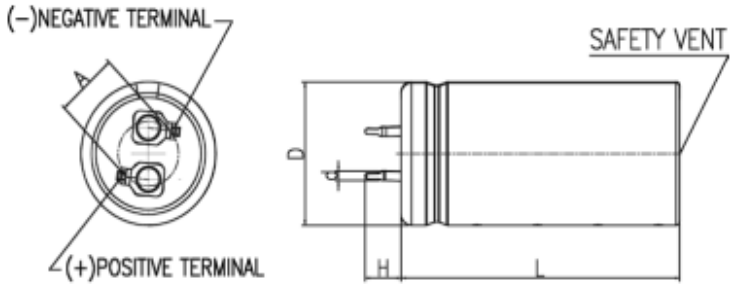

Figure 3.15 – Maxwell pseudocapacitor geometry [Maxwell18a].

Table 3.1 - Maxwell PCAP0 300 P230 S07 Dimensional Information

Item	Value
D	22 mm
H	6 mm
d	1.5 mm
L	46 mm
A	10 mm^2
Mass	24 g
Vn	2.3 V
Emax	0.22 Wh
Esp	9.10 Wh kg
Psp	1.4 kW/kg

As for the cell structure, it was based on [Gualous11], [LS17], [Béguin13] and [Obreja10] representations of the inner layer's definition and distribution. Therefore, a computational 3D model (Fig.3.16) was developed via the 3D modeling software Rhinoceros (version 5 SR9) in order to obtain dimensional information about each component part.

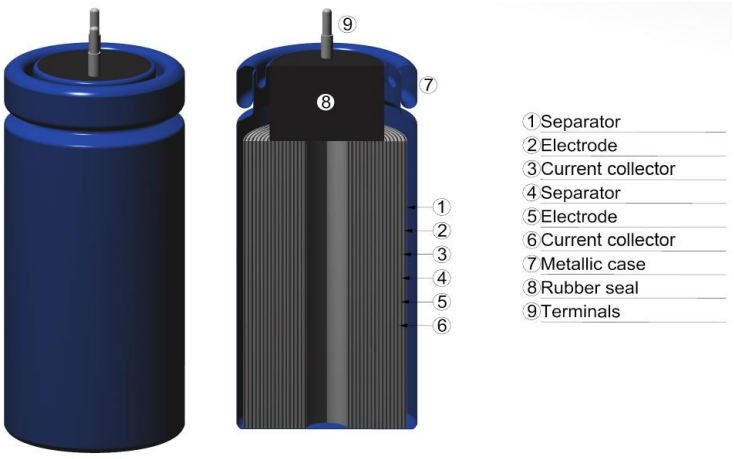

Figure 3.16 – Hybrid supercapacitor proposed 3D model.

As presented in (Fig.3.16) the device is composed of a metallic case, positive and negative metallic terminals, a rubber seal, a rolled stack of positive and negative electrodes films, separators and current collector.

Metallic Case

Supercapacitors, as well as other electric components, possesses a metallic casing made of aluminum alloys [Yassine17], which according to [Indalco13] and [AzoM13] is typically implemented in electrical and chemical industries, which properties are described in (Table 3.2).

Table 3.2 – Aluminium 1070 properties [Indalco13, AZoM13]

Item	Value
Density (20º C)	2.70 g cm^{-3}
Tensile strength	95 MPa

According to [Herrmann15] the typical housing thickness range for electrochemical cells and batteries is in the range of 20 to 100 µm, which maximum value was here implemented as the hybrid supercapacitor case thickness.

Terminals

According to [Vishay17] and [IC19], it is possible to assume the implementation of brass as generic material for supercapacitors terminals, which properties are presented in (Table 3.3) and based on the data sheet of CuZn37 (brass) alloy [Arubis13].

Table 3.3 – CuZn37 R300 properties [Arubis13]

Item	Value
Density	8.44 g cm^{-3}
Melting point	920 ºC
Tensile strength	300-380 MPa

Rubber Seal

As for the rubber seal applied for sealing such devices, the most typical material used is Ethylene Propylene Diene Monomer (EPDM) [Xu12], which properties are described in (Table 3.4) [Delta19].

Table 3.4 – EPDM DRE80 properties [Delta19]

Item	Value
Density	1.40 g cm^{-3}
Temperature range	-35 to 120 ºC
Tensile strength	5 MPa

Electrodes

In [Girard15] the faradaic electrodes were described with thickness ranging from 20 to 500 nm. However, from the Ni-Cu electrode scanning electron microscopy (SEM) it was possible to identify a varying thickness from 71.6 to 123µm (Fig.3.17), therefore a thickness of 70 µm was here defined as positive electrode thickness parameter for the model.

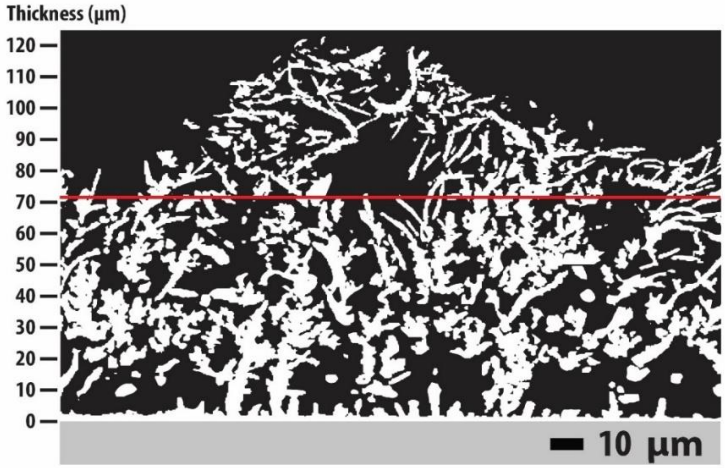

Figure 3.17 – Ni-Cu electrode SEM thickness.

With regards to the Maxwell pseudocapacitor's electrode material, as no information was found regarding its specification, the alternative was to focus on commercial

pseudocapacitive electrode materials. According to [Viswanathan17], manganese dioxide (MnO_2) is among the commonly implemented pseudocapacitors electrode materials, therefore, it was here implemented for such application, which parameters are presented in (Table 3.5) [GSMDS15].

Table 3.5 – Manganese dioxide (MnO_2) properties [GSMDS15]

Item	Value
Density	5.02 g cm^{-3}
Melting/freezing point	535 ºC

Current Collector

With regards to the current collector, [Obreja10] described the application of an aluminum foil, thus, it was here implemented as such, which parameters can be found in (Table 3.6) [Loba16].

Table 3.6 – Generic aluminum foil current collector properties [Loba16]

Item	Value
Density	2.70 g cm^{-3}
Melting point	660.37 ºC
Boiling point	2327 ºC
Auto-ignition	760 ºC

The chosen thickness was based on [Obreja10] which stated a thickness for the aluminum substrate at 30 μm, therefore, implemented here for such application.

Electrolyte

As for the electrolyte, [Viswanathan17] describes potassium hydroxide (KOH) as an aqueous electrolyte commonly used in pseudocapacitors, therefore, here implemented as such, which parameters can be found in (Table 3.7) [Merck06].

Table 3.7 – Potassium hydroxide (KOH) properties [Merck06]

Item	Value
Density	1.58 g cm^{-3}
Water solubility	20 ºC

The electrolyte thickness was based on [Girard15], which stated it as 2 μm for the pseudocapacitor modeling.

Separator

With regards to the separator, its thickness was based on [Kroupa16] and [Verbrugge05], which defined it as 25 μm.

According to [Liivand15], Celgard 2400 is defined as commercial separator material supercapacitors, which is defined as a monolayer polypropylene. Therefore, based on [Tabatabaei09] a 25 μm generic monolayer polypropylene was considered here as separator which properties are described in (Table 3.8) [Celgard19, Tabatabaei09].

Table 3.8 – Celgard 2400 separator properties [Celgard19, Tabatabaei09]

Item	Value
Density	0.9 g cm^{-3}
Pore size	0.043 μm
Porosity	40%

3.7.2 Dimensional Model

As described in section 3.8.1, in order to obtain the approximate volumetric information for the generic supercapacitor geometry, a 3D model was developed (Fig.3.16). The model took into consideration the dimensional information gathered from the Maxwell pseudocapacitor PCAP0300 P230 S07 [Maxwell18a] as well as material characteristics and definitions form a variety of publications.

The model was developed by first accounting for the casing, terminals and rubber seal dimensions. Once this step was concluded, the layers stacking order was defined based on [Obreja10] and an areal unit was defined for the complete stack by accounting the remaining metallic case internal height (36.3 mm) and stack width.

From the areal unit and materials densities, a linear optimization (LP) model was developed via the Microsoft Excel plug-in Solver, which resulted in an optimal stack length in order to meet the Maxwell pseudocapacitor total mass (Table 3.1).

3.7.3 Data Extraction

From the three-dimensional model developed, individual volumetric values for each of the electrodes, electrolytes, current collectors and separators layers were defined, which can be found in (Table 3.9).

Table 3.9 – Generic volumetry for the supercapacitor cell

Item	Volume (mm^3)	Mass (g)
Metallic Case	439.40	1.20
Terminals	49.80	0.42
Rubber Seal	1421.00	2.00
Electrodes	3329.30	16.70
Electrolyte	133.20	0.24
Separator	832.30	0.74
Current Collector	998.80	2.70
Total	7203.80	24.00

Therefore, the generic supercapacitor geometry developed met the dimensional and mass specifications derived from the Maxwell pseudocapacitor which then can be used as basis for the Ni-Cu hybrid supercapacitor modelling.

3.7.4 Ni-Cu Hybrid Supercapacitor

In order to physically model the Ni-Cu hybrid supercapacitor, the electrode, electrolyte and current collector materials information implemented in [Eugénio13] as well as the information regarding its capacitive response, gathered from CV and GCD tests for the sample material electrodeposited at a current density of 1.8 A cm^{-2} during 180 s, were applied in the development.

As hybrid supercapacitors typically combine faradaic and carbon-based electrodes, the theoretical device was proposed with a Ni-Cu metallic foam as positive electrode together with activated carbon as negative electrode. In accordance to [Eugénio13] and convention, the electrolyte implemented for both electrodes, positive (Ni-Cu) and negative (AC) [Shabeeba16], was potassium hydroxide (KOH), as for the current collector aluminum foil was implemented in both cases.

Activated Carbon Electrode

In order to properly implement activated carbon as negative electrode, the typical thickness was considered in accordance to [Kroupa16] and [Verbrugge05], which defined it as 50 μm.

With regards to the electrolyte volume, the approach here implemented was to define it as the activated carbon electrode porosity in relation to its rough volume. According to

[Ekpete11], the bulk density, which is related to the pressed powder into an electrode, is stated as 0.66 g cm^{-3} (±0.05), while its porosity is 77% (±5). As [Girard15] divided electrodes and electrolytes in two separated thickness, the value of both in (Table 10) must be accounted here, which for the activated carbon electrode and its electrolyte half of the sum of the volumes, 1731.25 mm^3, will be implemented as described in (3.38-3.39).

$$Electrolyte_{vol1} = 1731.25 * 0.77 = 1333.06 \ [mm^3] \quad (3.38)$$

$$A.C.Electrode_{vol} = 1731.25 - 1333.06 = 398.19 \ [mm^3] \quad (3.39)$$

As for KOH 1M solution concentration, according to [Merck06] at 20 ºC its density is stated as 1.58 g cm^{-3}, which when applied to the respective volume results in a total mass of 2.106 g (3.40).

$$Electrolyte_{mass1} = 1.33306 \times 1.58 = 2.106 \ [g] \quad (3.40)$$

The mass of activated carbon electrode was calculated by applying the acquired volume to its respective density (3.41).

$$A.C.Electrode_{mass} = 0.39819 \times 0.66 = 0.2628 \ [g] \quad (3.41)$$

Ni-Cu Foam Electrode

With regards to the Ni-Cu metallic foam positive electrode, its thickness was considered proportional to the respective generic model layer.

Therefore, the same procedure implemented for the determination of the activated carbon electrode volume was here used. In order to define the Ni-Cu foam porosity a 3D model of the electrode was developed based on [Eugénio13], more specifically in both the scanning electron microscopy (SEM) electrode section (Fig.3.18) and the graph of variation in surface pore area and number of surface pores (Fig.3.19), taking as geometry a cube of 100.10^4 μm^3.

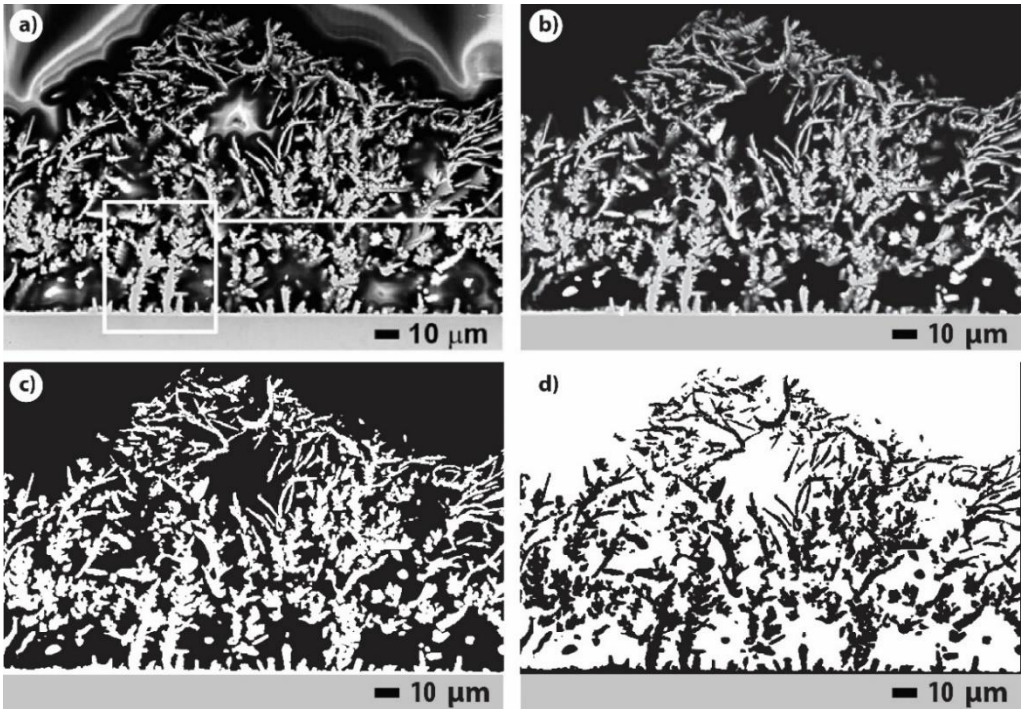

Figure 3.18 – a) SEM 1.8 A cm^{-2} 180 s, electrode section, b)-d) image enhancing and cleanup [Eugénio13]

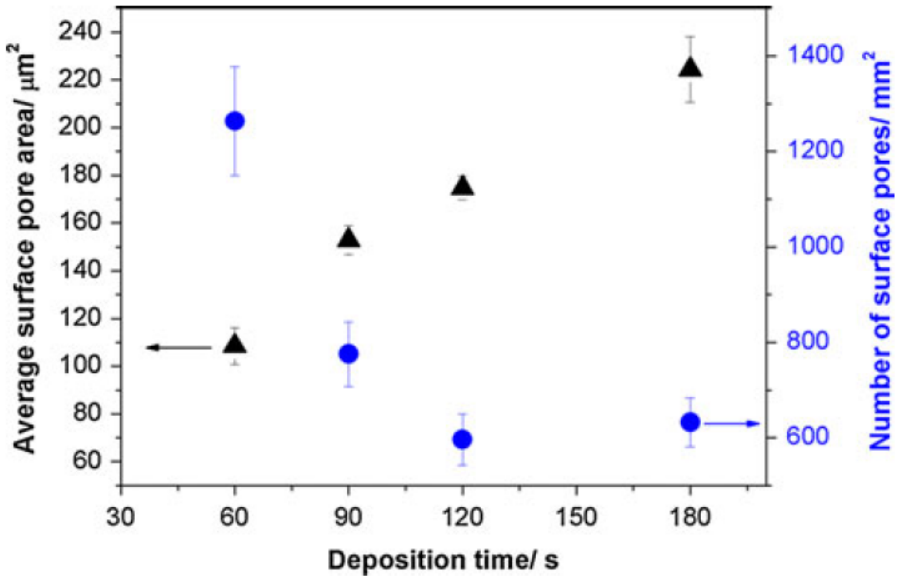

Figure 3.19 – Variation in surface pore and number of surface pores [Eugénio13]

As displayed in (Fig.3.18) the electrode section was enhanced and cleaned via the graphic software Adobe Photoshop and Adobe Illustrator CS6, which was then exported in a drawing exchange format (DXF) to be modelled in Rhinoceros 5.0 as a representation for the cube lateral sides. With regards to the (Fig.3.19) [Eugénio13] described the average

surface pore area for the sample deposited ate 1.8 A cm^{-2} during 180 s as 225 μm^2, which makes it is possible to determine an approximate pore average diameter of 17 μm when considering nearly circular pore geometries (3.42).

$$Pore\emptyset = 2\sqrt{\frac{225}{\pi}} \approx 17\ [\mu m] \tag{3.42}$$

From (Fig.3.19) it is possible to determine that the superficial pore density is approximately 630 pores/mm^2 which together with the pores dimeter and area were implemented to design the top and bottom profiles of the electrode sample cube. Therefore, a resulting volume of more than 89.10^4 μm^3 was obtained as a prediction of the actual electrolyte volume (Fig.3.20) inside a total volume of 100.10^4 μm^3 which consequently defines the Ni-Cu foam porosity to over 89% when measured only in the range of macropores (section 3.3), as the images only supply such sort of information.

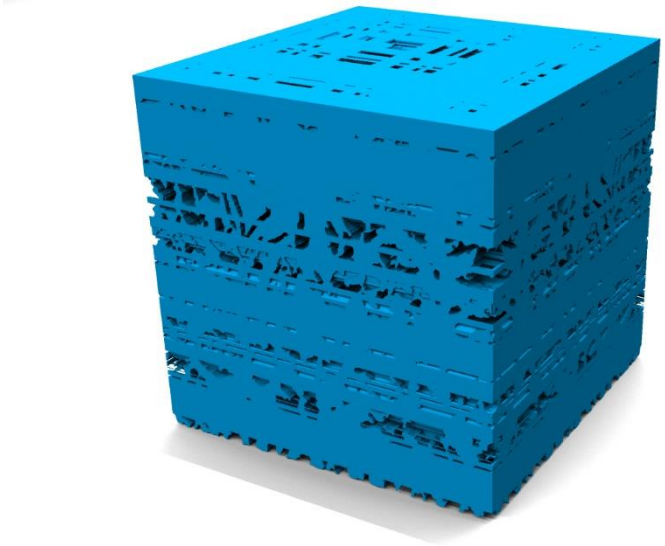

Figure 3.20 – Electrolyte volume from electrode porosity modelling

Despite the difference of foams manufacturing process, when comparing the obtained result with the information gathered from [AE19], a commercial Ni-Cu metallic foams supplier, which stated the material's porosity in the range of 75 to 95%, and based on the statement of [Eugénio13] that metallic foams porosity values are above 50%, it is safe to say that the value acquired is sufficiently in accordance, what would be increased with more detailed image samples, taking it into the range of micro porosity.

Therefore, by assuming the porosity values from the manufacturer, 95%, it was possible to calculate the respective electrolyte and electrode volumes (3.43-3.44) from (3.38-3.39) by replacing the activated carbon porosity value.

$$Electrolyte_{vol2} = 1731.25 \times 0.95 = 1644.69 \ [mm^3] \quad (3.43)$$

$$Ni - Cu.Electrode_{vol} = 1731.25 - 1644.69 = 86.56 \ [mm^3] \quad (3.44)$$

According to [Corun19] the density of Ni-Cu metallic foams is defined in the range of 0.15 to 0.45 g cm^{-3}, which when applied to the calculated volume was used to determine the electrode's mass (3.45). As for the electrolyte, the mass (3.46) was obtained by changing the respective volume in (3.40).

$$Ni - Cu.Electrode_{mass} = 0.08656 \times 0.45 = 0.039 \ [g] \quad (3.45)$$

$$Electrolyte_{mass2} = 1.64469 \times 1.58 = 2.60 \ [g] \quad (3.46)$$

Ni-Cu Foam Hybrid Supercapacitor

From the data calculated above it was possible to theorize the device regarding its volume and, by also applying the formulas from section 3.6.2, its storage capabilities.

The resulting device's volume and mass distribution is described in (Table 3.10).

Table 3.10 – Ni-Cu hybrid supercapacitor volume and mass distribution

Item	Volume (mm^3)	Mass (g)
Metallic Case	439.40	1.20
Terminals	49.80	0.42
Rubber Seal	1421.00	2.00
AC.Electrode	398.19	0.26
KOH.Electrolyte	1333.06	2.11.
Current Collector (Al)	998.80	2.70
Ni-Cu.Electrode	86.56	0.04
KOH.Electrolyte	1644.69	2.60
Separator	832.30	0.74
Total	7203.80	12.07

From (Table 3.10) in comparison to (Table 3.9), it is possible to notice that when occupying the same volume, the Ni-Cu hybrid supercapacitor presented a mass decrease in approximately 50%.

With regards to storage capabilities, from (3.26) the total active material mass, which is defined as the sum of electrodes and electrolytes masses, was calculated by differing the cathode and anode contributions (3.47).

$$m_{total} = 2.37 + 2.64 = 5.01\ [g] \tag{3.47}$$

From [Eugénio13] were collected the approximate values for discharge time, potential, current density, electrode area and specific capacitance, 362.5 s, 0.45 V, 1 mA cm^{-2}, 1.65 cm^2 and 105 F g^{-1}, respectively. The positive electrode capacitance (C_{elec+}) was obtained by (3.48-3.49).

$$C_{sp,elec+} = \frac{C_{elec+}}{m_{elec+}}\ [F] \tag{3.48}$$

$$C_{elec+} = C_{sp.elec+}\, m_{elec+} = 105 \times 2.64 = 277.2\ [F] \tag{3.49}$$

According to [Shabeeba16], the specific capacitance for activated carbon electrodes is in the range of 65 to 70 F g^{-1}, even though some researchers have presented higher laboratorial results. From (3.49) it was possible to determine the capacitance for the negative electrode (activated carbon) as described in (3.50).

$$C_{elec-} = C_{sp.elec-}\, m_{elec-} = 70 \times 2.37 = 166\ [F] \tag{3.50}$$

Therefore, the cell capacitance (C_{cell}) was defined by assuming the smaller capacitance value ($C_{elec}{}^{c<}$) between both electrodes as described in section 3.7.2 [Eliaz19] (3.51).

$$C_{cell} = C_{elec}{}^{c<} = 166\ [F] \tag{3.51}$$

It is noticeable that the capacitance value for the theoretical Ni-Cu pseudocapacitor is smaller than Maxwell's product. However, it is important to notice that even though the resulting volume and mass of the generic model in section 3.8.3 are the same as the

Maxwell's pseudocapacitor, their storage characteristics are not proportionally comparable as the materials implemented are not equivalent due to the lack of information.

With that said, two different approaches can be made, by matching the total Ni-Cu hybrid supercapacitor layers volumes to the maximum space available in the generic model, 14740 mm^3 and meeting the intended total mass of the generic model.

For the first case, the values are presented in (Table 3.11).

Table 3.11 – Case 01 - Ni-Cu hybrid supercapacitor volume redistribution

Item	**Volume (mm^3)**	**Mass (g)**
Metallic Case	439.40	1.2
Terminals	49.80	0.42
Rubber Seal	1421.00	2
AC.Electrode	1020.37	0.67
KOH.Electrolyte	3416	5.41
Current Collector (Al)	2559.45	6.92
Ni-Cu.Electrode	221.81	0.10
KOH.Electrolyte	4214.57	6.66
Separator	2132.79	1.90
Total	15475.19	25.27

From the data in (Table 3.11) and the very same calculation made from (3.48-3.51), a new capacitance value was found for the device (3.52).

$$C_{cell} = {C_{elec}}^{c<} = \ 426\ [F] \tag{3.52}$$

Regarding the second case, to meet the total mass of the generic model, the layers volume occupied was of 14686.53 mm^3 (Table 3.12).

Table 3.12 – Case 2 - Ni-Cu hybrid supercapacitor mass redistribution

Item	Volume (mm^3)	Mass (g)
Metallic Case	439.4	1.2
Terminals	49.8	0.42
Rubber Seal	1421	2
AC.Electrode	903.12	0.60
KOH.Electrolyte	3730.26	5.89
Current Collector (Al)	2265.34	6.12
Ni-Cu.Electrode	196.32	0.09
KOH.Electrolyte	3793.592	5.99
Separator	1887.7	1.70
Total	14686.53	24.00

From the data in (Table 3.12) and according to (3.52), a new capacitance value was found for the device (3.53).

$$C_{cell} = {C_{elec}}^{c<} = \ 454.3\ [F] \tag{3.53}$$

As the hybrid supercapacitor with mass redistribution provided a better comparative by maintaining the rated mass, the calculations (3.54-3.60) were focused on such option.

Equivalent Series Resistance (ESR)

In order to calculate de equivalent series resistance (ESR) to the Ni-Cu device, according to [Vicentini19], such parameter is calculated by the voltage drop when the charging is interrupted therefore obtaining the discharge profile. The calculation was made by the data interpreted from the galvanostatic charge and discharge curves (GCD) from [Eugénio13] for the 1.8 A cm^{-2} at 180 s sample (Fig.3.21).

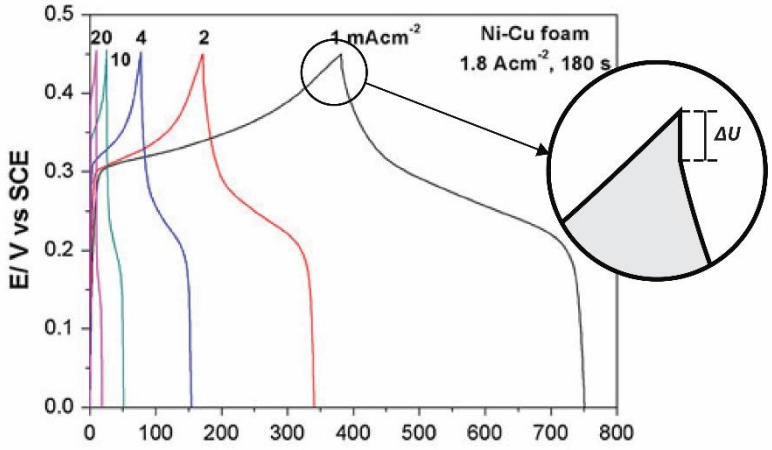

Figure 3.21 – GCD curves, voltage drop [Eugénio13]

The ESR can be obtained from (3.54), where ΔU is the voltage drop determined as approximately 18.4 mV and I is the current applied, stated as 1 mA cm^{-2}.

$$ESR \approx \frac{18.4}{2 \times 0.001} = 9.2\ [m\Omega] \tag{3.54}$$

Cell Voltage

From the galvanostatic charge and discharge curves (GCD) in [Eugénio13] (Fig.A5.6) it is possible to analyze that the potential range is presented as from 0.0 to 0.45 V with t= 370 s, potential which is in accordance to 0.5 V present in [Jeong12]. However, in the hybrid device, activated carbon (AC) was implemented as negative electrode, therefore, the value assumed as potential range was obtained from [Shabeeba16] (Fig.3.22) for a prepared AC.

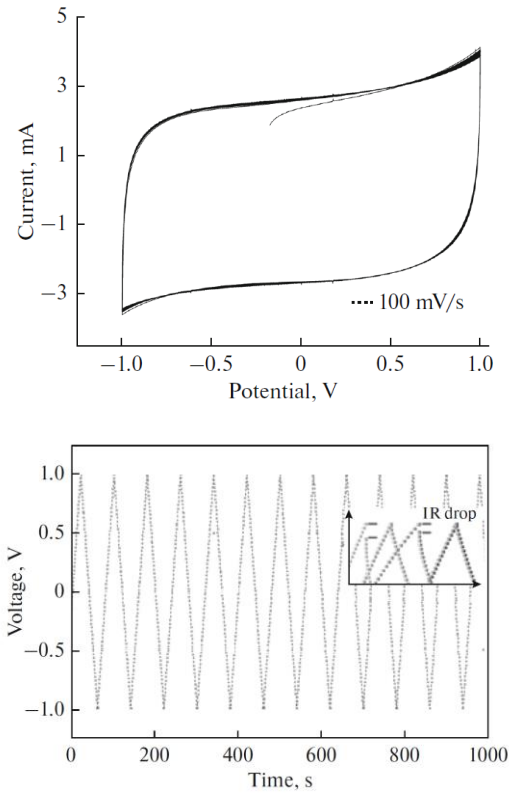

Figure 3.22 – a) Cyclic voltammetry and b) Galvanostatic charge and discharge curves of activated carbon [Shabeeba16]

The cell voltage was proposed according to [Dai15], which stated the maximum charging voltage (MCV) as presented in (Fig.3.23).

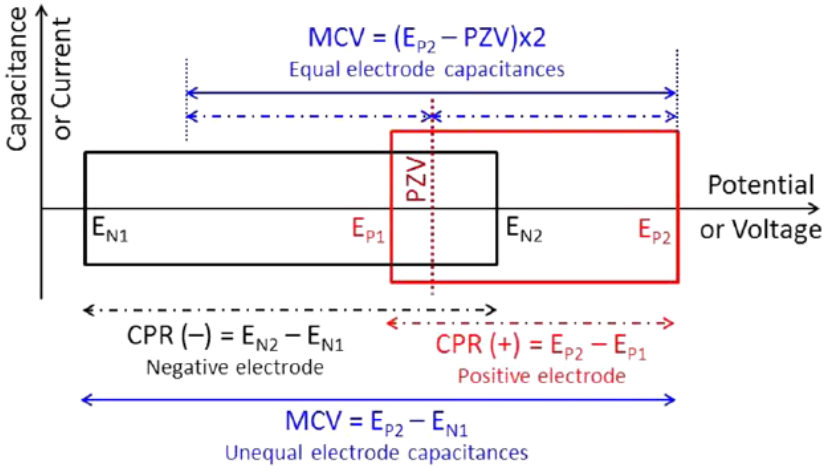

Figure 3.23 – Supercapacitor cell voltage [Dai15]

Where CPR is the capacitive potential range, E_N and E_P represent the negative and positive electrodes respectively and PZV is the potential of zero voltage or equipotential.

The MCV is defined as a result of different situations. When the two electrodes CPRs overlap, where $E_{N2} > E_{P1}$, the MCV is defined as being narrower than both CPRs summed. A second case is defined as when one of the CPRs completely covers the other, where the result is described by $E_{N1} < E_{P1}$ and $E_{N2} > E_{P2}$ for wider negative electrode CPRs and $E_{P1} < E_{N1}$ and $E_{P2} > E_{N2}$ for wider positive electrode CPRs, which MCV is defined by the narrower available CPR. If the electrode's CPRs are not connected at all, $E_{N2} < E_{P1}$, the cell assumes a minimum discharging voltage (MDV) defined by (3.55). Besides the previously mentioned cases, another aspect may define the MCV, which is the PZV. The potential of zero voltage arise if the two electrodes have the same potential, the total discharge of the supercapacitor occurs and the confirmation of V=0 by the validation of $E_{N2} \geq E_{P1}$. In case of asymmetric supercapacitors, if the capacitances of both electrodes are the same, the PZV must be analyzed according to two situations, PZV-$E_{N1} > E_{P2}$-PZV or PZV-$E_{N1} < E_{P2}$-PZV, which defines the voltage determining electrode as either the positive or negative respectively. If the voltage if defined by the positive electrode, MCV is calculated by (3.56), if negative by (3.57).

$$MDV = E_{P1} - E_{N2}\ [V] \tag{3.55}$$

$$MCV = (E_{P2} - PZV)\ 2\ [V] \tag{3.56}$$

$$MCV = (PZV - E_{N1})\ 2\ [V] \tag{3.57}$$

Therefore, CVs and GCDs from both [Eugénio13] and [Shabeeba16], were overlapped (Fig.3.24) as described in [Dai15] ($E_{N1} < E_{P1}$ *and* $E_{N2} > E_{P2}$) and the cell rated voltage (V_R) of 2V was assumed.

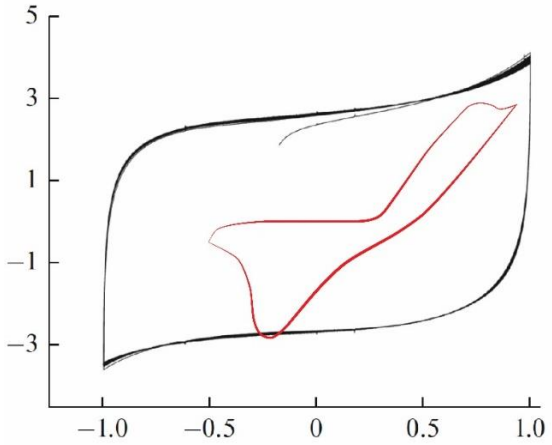

Figure 3.24 – Proposed CV of Ni-Cu/AC hybrid supercapacitor

Maximum Energy Storage

The following formulas were taken from [Maxwell18a] as providing a proper comparison basis. The maximum energy storage capability for the device is described in (3.58).

$$E_{max.hybrid} = \frac{\frac{C\ V_R^2}{2}}{3600} = \frac{\frac{454.3\ \times\ 2^2}{2}}{3600} = 0.25\ [Wh] \tag{3.58}$$

The energy calculation presented above is related to EDLCs, however in [Maxwell18a] it is implemented for a faradic device, peseudocapacitor. According to [Kakaei19], due to faradaic supercapacitors characteristics, such devices energy must be calculated by (3.59), where the initial voltage (V_1) is greater than 0, differently from EDLCs devices that for the energy calculation assume V_1 as 0, due to its triangular profile when in relation to the voltage/time graph (Fig.3.25). The trapezoidal electrochemical curve of faradaic materials can be understood in (Fig.A5.6), while in (Fig.3.22) for the triangular curve.

$$E_{hybrid.asymm} = \frac{C\ V_2^2}{2} - \frac{C\ V_1^2}{2}\ [Wh] \tag{3.59}$$

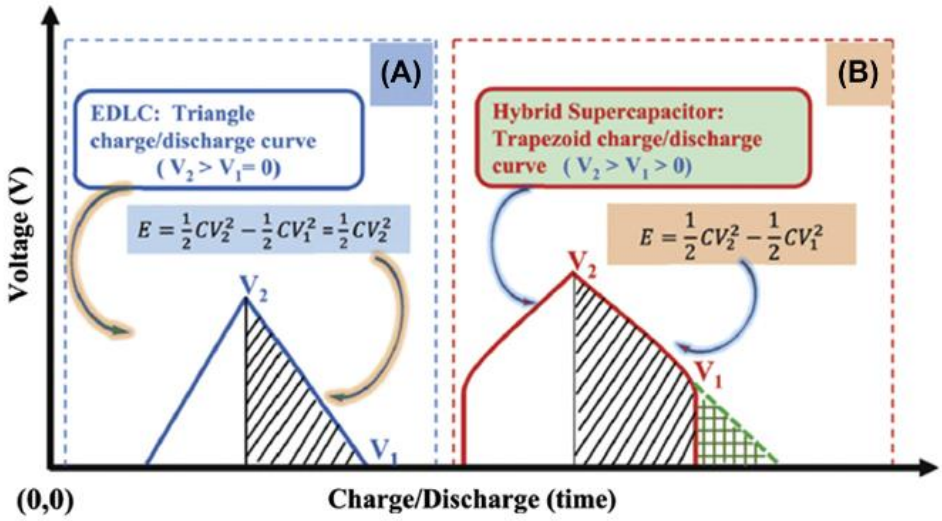

Figure 3.25 – Charge and discharge curves of a) EDLCs and b) Hybrid supercapacitors [Kakaei19]

However, in this dissertation the energy calculated was based on (3.58) as it is presented in [Maxwell18a] for pseudocapacitors and in [Ye18] when modeling hybrid supercapacitors.

Gravimetric Specific Energy

The gravimetric specific energy (E_{sp}) can be calculated from the maximum energy stored and the device's total mass as presented in (3.60).

$$E_{sp.hybrid} = \frac{E_{max}}{m} = \frac{0.25}{0.024} = 10.42 \left[\frac{Wh}{kg}\right] \tag{3.60}$$

Usable Specific Power

As for the usable specific power (P_{sp}), the calculation was implemented as in (3.61), based on [Maxwell18a].

$$P_{sp.hybrid} = \frac{0.12\, V_R^2}{ESR\, m} = \frac{0.12 \times 2^2}{9.2 \times 0.024} = 2.17 \left[\frac{kW}{kg}\right] \tag{3.61}$$

The Ni-Cu hybrid supercapacitor computational simulation was developed with the aid of the software Matlab Simulink 2018b, which is detailed described in annex 6.

3.8 Conclusions

The supercapacitor cell modeling procedure described in this chapter has shown to be sufficient for the intent of this dissertation, by entirely allowing the data extraction from a basis device and the proposed electrode material, therefore providing consistent data to be compared, analyzed and implemented in a computational simulation. The modeled nickel-copper metallic foam hybrid supercapacitor cell has presented superior results when compared to the Maxwell 2.3V 300F pseudocapacitor by achieving higher capacitance values (454.3F) while maintaining the same rated mass as proposed by the generic model. In completion, as mentioned in annex 5, A5.4, the Ni-Cu electrode's manufacturing procedure, electrodeposition, has relative lower costs when compared to other processes for the same material, which works as another positive comparison point when analyzing the feasibility of the obtained results.

With regards to the device's modeling, besides the differences between theoretical circuits of supercapacitors, pseudocapacitors and hybrid supercapacitors, the model chosen for implementation was a generic Matlab Simulink block due to the assumption that major relevant behavior aspects and characteristics of such devices would be reflected in their primary parameters such as voltage, capacitance, resistance, energy and mass. Therefore, by implementing the supercapacitors parameters identification procedure [MathWorks18b], generic data regarding the device's primary specifications were generated so the block could be implemented in further simulations (chapter 5). The strategy proposed in order to extract the required data without a real supercapacitor cell and equipment has proven itself successful, once the simulated parameters sufficiently matched the digitally manipulated voltage curve. Also, for further validation such device was implemented in different simulations (chapter 5), therefore providing complementary comparative results.

CHAPTER 4

Electric Vehicles - EVs

This chapter presents an introduction to Electric Vehicles, their dynamic equations, structure, propulsion and possible Energy Storage Systems (EES) to be implemented with a focus on Hybrid Energy Storage Systems (HEESs). Finally, it is presented the development of its computational model with the software Matlab Simulink 2018b.

4.1 Introduction

According to [Ehsani05], electric vehicles (EVs) are driven by electric motors, which are supplied by a variety of electric energy sources as electrochemical batteries, supercapacitors, fuels cell, and many others. The EVs can rely on one or more motors as components of the vehicle's drive system, directed for traction or secondary functionalities [Mahmoudi14]. Among the advantages of such transportation technologies, the most acknowledged are the reduction or even the inexistence of pollutant emissions and increased efficiency, characteristics which makes the EVs more and more attractive. As described by [Mahmoudi14], the most common or publicly known electric vehicles technologies are Hybrid Electric Vehicles (HEVs), Plug-in Hybrid Electric Vehicles (PHEVs), Fuel Cell Electric Vehicles (FCEVs) and Solar Electric Vehicles (SEVs).

With regards to the electric vehicle's classification, as described before, there is a second characterization method made through the degree of electrification as described in (Fig.4.1).

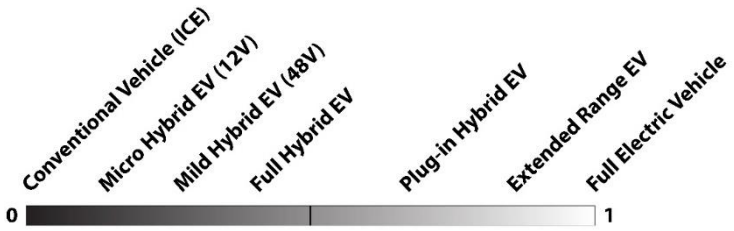

Figure 4.1 – Degree of Electrification [Mahmoudi14]

4.2 Equations of a Generic Vehicle

The electric vehicles as well as any other four wheeled vehicles are generically ruled by the same basic equations, which therefore are adaptable to specific configurations, hence, vehicles specifications.

4.2.1 Acting and Resulting Forces

The vehicle, as any other object, is susceptible to the basic laws of physics. Therefore, each acting force must be considered whether it is applied to or caused by the vehicle. In (Fig.4.2-4.3) the acting and resulting forces of a vehicle dynamics are described [Ehsani05].

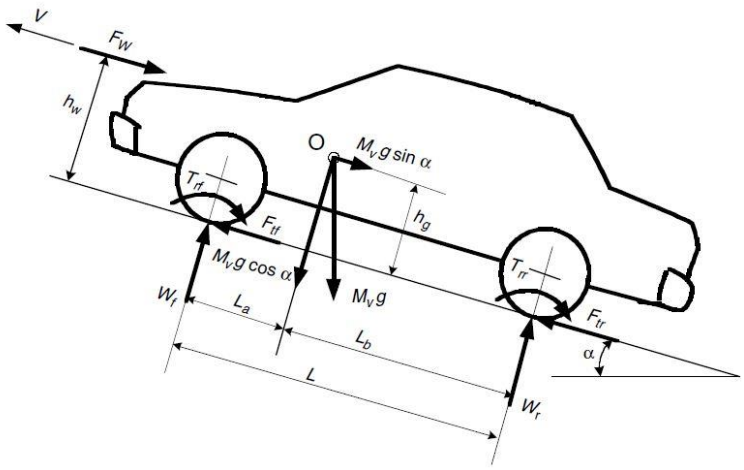

Figure 4.2 – Vehicle acting forces - Inclined [Ehsani05]

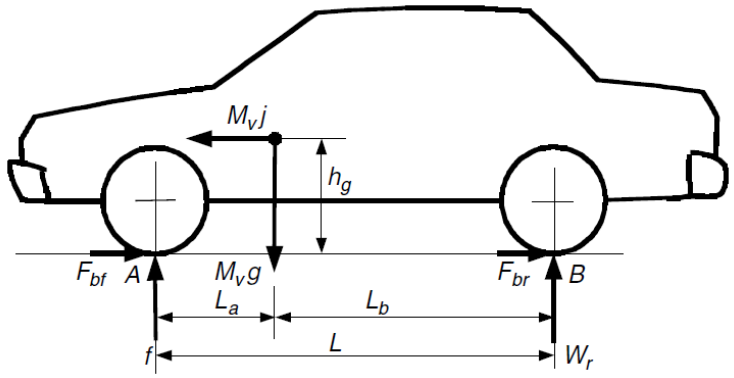

Figure 4.3 – Vehicle acting forces - Horizontal [Ehsani05]

Where V, stands for velocity, F_w is the aerodynamic drag, h_W is the height of the center of application of aerodynamic resistance (F_w) and is often assumed as equal to h_g, which stands for the height to center of gravity [Ehsani05]. The frontal and rear tires rolling resistances are referenced by T_r and T_f respectively. As for L_t, L_a and L_b, they represent the total distance between axles, the distance from the frontal axle to the center of gravity (CG) and from CG to the rear axle [Ehsani05]. The frontal axle contact to the ground is referenced as A, while B stands for the rear one. In A and B, the frontal and rear loads are

described as W_f and W_r respectively. With regards to the break forces, those are described as F_{bf} and F_{br} while the tractive efforts are represented as F_{tf} and F_{tr} for the front and rear wheels respectively. The vehicle also is influenced by the normal force, which is described as $M_v g$ where M_v is the vehicle's mass and g stands for the gravitational acceleration, also known as standard gravity or standard acceleration, 9.81 m s^{-1}. While $M_v g.sin(\alpha)$ and $M_v g.cos(\alpha)$ are the resulting forces in relation to terrain inclination angle α. In (Fig.4.3) it is possible to notice $M_v j$ which is defined as the forward force [Ehsani05].

4.2.2 Equations

With the intent to calculate and predict the expected behavior of a vehicle, the following equations are implemented, in which the previously mentioned variables are used [Ehsani05].

The vehicle acceleration is described by Newton as (4.1).

$$\frac{dV}{dt} = \frac{\sum F_t - \sum F_{tr}}{\delta M_v} \tag{4.1}$$

Where δ is the effect of the powertrain components described as mass factor.

The aerodynamic drag is calculated according to (4.2) and is used to account the interference of air masses against the vehicle, resulting in a deaccelerating force.

$$F_w = \frac{1}{2}\rho A_f C_D (V + V_W)^2 \tag{4.2}$$

Where ρ stands for the air density, A_f is the vehicle frontal area, C_D is the aerodynamic drag coefficient, and V_w is the wind speed [Ehsani05].

As for the calculation of a vehicle displacement in an inclined plane, the grading resistance is defined as (4.3) and can be simplified if the angles are small as in (4.4).

$$F_g = M_v \sin\alpha \tag{4.3}$$

$$m = \frac{H}{L_t} = \tan\alpha \approx \sin\alpha \tag{4.4}$$

Where m is the inclination grade and H is the height of the opposite side of the triangle that represents the plane inclination [Ehsani05].

The road resistance (F_{rd}) is defined as the sum of both the tire rolling resistance (F_f) and the grading resistance (F_g) (4.5), also simplified for smaller angles as (4.6) [Ehsani05].

$$F_{rd} = F_f + F_g = M_v g(f_r \cos\alpha + \sin\alpha) \tag{4.5}$$

$$F_{rd} = F_f + F_g = M_v g(f_r + m) \tag{4.6}$$

Where f_r is the rolling resistance coefficient.

With regards to the vehicle motion, the equation to describe the longitudinal displacement is defined as (4.7) [Ehsani05].

$$M_v \frac{dV}{dt} = \left(F_{tf} + F_{tr}\right) - \left(F_{rf} + F_{rr} + F_w + F_g\right) \tag{4.7}$$

Where F_{rr} and F_{rf} describe the rolling resistances for the rear and front tires.

The normal loads on the front and rear axles are described by (4.8) and (4.9), respectively.

$$W_f = \frac{M_v g L_b \cos\alpha - (T_{rf} + T_{rr} + F_w h_w + M_v g h_g \sin\alpha + M h_g dV/dt)}{L_t} \tag{4.8}$$

$$W_r = \frac{M_v g L_b \cos\alpha - (T_{rf} + T_{rr} + R_w h_w + M_v g h_g \sin\alpha + M_v h_g dV/dt)}{L_t} \tag{4.9}$$

Which can be simplified as considering h_w as h_g (4.10) and (4.11).

$$W_f = \frac{L_b}{L_t} M_v g \cos\alpha - \frac{h_g}{L_t}\left(F_w + F_g + M_v g f_r \frac{r_d}{h_g}\cos\alpha + M_v \frac{dV}{dt}\right) \tag{4.10}$$

$$W_r = \frac{L_a}{L_t} M_v g \cos\alpha + \frac{h_g}{L_t}\left(F_w + F_g + M_v g f_r \frac{r_d}{h_g}\cos\alpha + M_v \frac{dV}{dt}\right) \tag{4.11}$$

Where T_{rf} and T_{rr} are the frontal and rear rolling resistance torques, F_w is the aerodynamic drag and r_d is referred as the wheel radius [Ehsani05].

From (4.10) and (4.11) can be rearranged as (4.12) and (4.13).

$$W_f = \frac{L_b}{L_t} M_v g \cos\alpha - \frac{h_g}{L_t}\left(F_t - F_r\left(1 - \frac{r_d}{h_g}\right)\right) \tag{4.12}$$

$$W_r = \frac{L_a}{L_t} M_v g \cos\alpha + \frac{h_g}{L_t}\left(F_t - F_r\left(1 - \frac{r_d}{h_g}\right)\right) \tag{4.13}$$

The total tractive effort F_t of the vehicle is defined as (4.14), as for the total rolling resistance is represented by F_r.

$$F_t = F_{tf} - F_{tr} \tag{4.14}$$

There are differences, as expected, in relation to the tractive axles of a vehicle due to the distribution of forces applied and vehicle's mass. For a vehicle driven by a front-wheeled drive system, the total tractive effort, which is the limiting applicable force before the loss of the tire-ground connection, can be described as (4.15), as for the rear traction driven vehicle it is described in (4.16) [Ehsani05].

$$F_{t\,max} = \frac{\mu M_v g \cos\alpha \left[L_b + f_r\left(h_g - r_d\right)\right]/L_t}{1 + \mu h_g L_t} \tag{4.15}$$

$$F_{t\,max} = \frac{\mu M_v g \cos\alpha \left[L_a + f_r\left(h_g - r_d\right)\right]/L_t}{1 + \mu h_g L_t} \tag{4.16}$$

Where f_r stands for the rolling resistance coefficient.

Besides the vehicle dynamics, it is necessary to understand the equations that governs the power train, which are described above.

The torque generated by the driving wheel axle, T_w, is defined as in (4.17).

$$T_w = i_g i_0 \eta_t T_p \tag{4.17}$$

Where i_g is defined as the gear transmission ratio (4.18), i_0 stands for the gear ratio of the final drive, η_t is the transmission efficiency accounted from the motor output to the driving wheel, which torque if described as T_p [Ehsani05].

$$i_g = \frac{N_{in}}{N_{out}} \tag{4.18}$$

Where N_{in} is described as the rotational speed input and N_{out} is the output.

The tractive effort for the drive wheel is described by (4.19) and (4.20). As for the rotating speed for the same reference, it can be described as in (4.21).

$$F_t = \frac{T_w}{r_d} \tag{4.19}$$

$$F_t = \frac{T_p i_g i_0 \eta_t}{r_d} \tag{4.20}$$

$$N_w = \frac{N_p}{i_g i_0} \tag{4.21}$$

In (4.22) the equation for the translational speed, measured from the wheel center accounting the wheel radius, is described [Ehsani05].

$$V = \frac{\pi N_p r_d}{30 i_g i_0} \left[\frac{m}{s}\right] \tag{4.22}$$

4.3 EVs Structure – Understanding its Operation

4.3.1 Structure and Configuration

Electric vehicles are generically composed of electric propulsion, energy source and auxiliary subsystems (Fig.4.4).

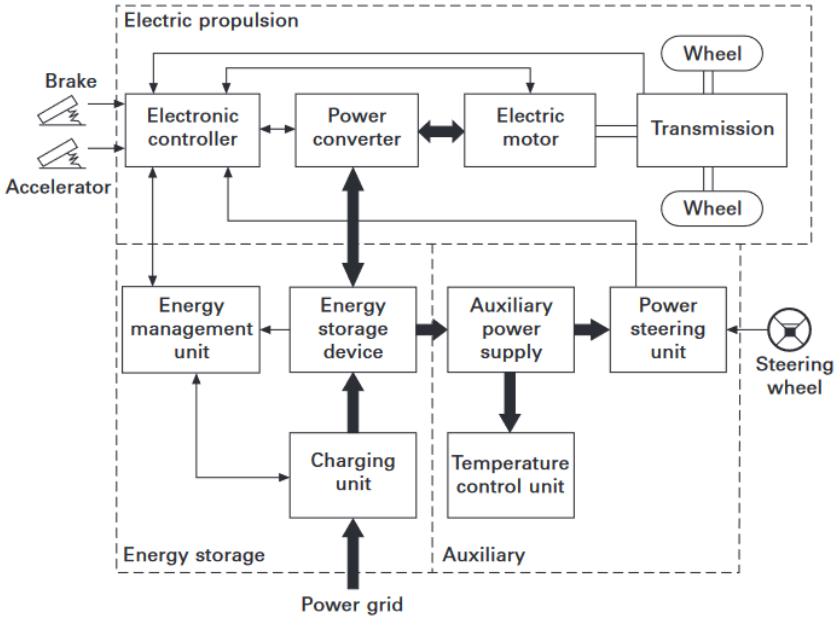

Figure 4.4 – EV general structure [Chau14]

With regards to the electric propulsion subsystem, it is composed of a controller, power converter, electric machine and mechanical power transmission connected to the driving

wheels. As for the energy source, it encompasses the energy source, charging unit and management. Finally, the auxiliary subsystem is composed of a power steering unit, auxiliary power supply and climate control. In fact, the configuration is not definitive as it can be customized regarding the intent [Chau14].

4.3.2 Operation and Performance

As this dissertation takes into consideration only pure electric vehicles, just such operation will be described.

In (Fig.4.4) the thick arrows are related to the electrical link between subsystems components, as for the thin arrows, these indicate the control relation. The brake and accelerator pedals trigger different signal s to the controller which acts directly to the power converter in order to level the power flow from the energy storage system to the motor. As for the energy management unit, it interacts with the controller with regards to energy recovery from regenerative braking, monitors the energy storage device and manages the charging input. In order to supply the auxiliary requirements of the vehicle, the auxiliary power supply is responsible for meeting the different needs presented, specially supplying the temperature control and power steering [Chau14].

The performance of an EV is usually defined by acceleration performance and maximum speed [Ehsani05]. The author also describes drive train design, motor power rating and proper transmission parameters as primary concern in order to meet the proposed specifications, specifications which are dependent of the motor torque characteristics.

4.4 Electric Propulsion

For electric vehicles, the motors are required to offer high torque, high power density, high efficiency, good control capabilities, increased reliability and as minimum as possible maintenance [Chau14].

The existing and most common electric motors implemented in EVs drive are direct current (DC) drives, induction drives, switched reluctance (SR) drives, and permanent magnet (PM) brushless drives, motors which comparison is presented in (Table 4.1) as a point grading system, where the evaluation ranges from 1 to 5 points, as 1 being the lowest score and 5 the maximum.

Table 4.1 – Point grading system [Chau14]

Item	DC	Induction	SR	PM Sync	PM BLDC
Power density	2	3	3.5	4.5	5
Efficiency	2	3	3.5	4.5	5
Controllability	5	4	3	4	4
Reliability	3	5	5	4	4
Maturity	5	5	4	5	4
Cost level	4	5	4	3	3
Noise level	3	5	2	5	5
Maintenance	1	5	5	5	5
Total	25	35	30	35	35

4.5 Electric Energy Storage Systems

Electric vehicles rely on energy storage systems in order to supply its driving system. Typically, electrochemical batteries are the EVs storage choice mainly due to its great energy density rates, which is directly connected to the vehicles autonomy. However, there are a variety of energy storage options, from independent configurations to hybrid setups, which encompasses specially batteries and supercapacitors.

Batteries and supercapacitors are commercially available as individual cells which, in order to meet a specific load requirement, are combined in packs or modules respectively, which setup is possible either in series, parallel or both.

In the case of batteries, the cell specification comprises a variety of information among which the most common are capacity (Q) in Ah, voltage (V), charge and discharge currents (A), internal resistance (Ri), charging time in h, mass in kg and lifecycle. With regards to the discharge characteristic, the discharge C_{rate} defines the current supply capability of such cell, for a certain period, measured in hours and obtained by (4.23) [Ehsani05].

$$C_{rate} = \frac{Q}{Idc} \tag{4.23}$$

The state of charge (SOC) of batteries (4.24), which is defined as the remaining battery charge in a certain time, is measured in percentages and its variation in a time interval is defined by (4.25).

$$SOC = SOC_0 - \int \frac{i\,dt}{Q(i)}\ [\%] \tag{4.24}$$

$$\Delta SOC = \frac{i\,dt}{Q(i)}\ [\%] \tag{4.25}$$

There are several commercially available batteries, which the most common types are lithium-ion (Li-ion) and lead-acid (Pb-acid) [Chau14].

Among the different supercapacitor's types, the typically commercialized are EDLCs, pseudocapacitors and hybrid supercapacitors. The specifications of such storage devices cells typically encompass the rated voltage (*V*), capacitance (*C*), series resistance (ESR), mass in *g*, energy in *Wh*, specific energy in *Wh kg*$^{-1}$ and specific power in *W kg*$^{-1}$. As the voltage is relatively low, supercapacitors are usually connected in series in order to reach a specific load requirement [Chau14].

When speaking of EVs, the charge and discharge cycles present different behaviors as the requirements of starting and baking are different. At the starting moment as well as in an inclined plane, the EV demand high and translated as a peak of energy from the storage device, while when in an horizontal steady trajectory it is relatively lower, difference which can often represent a 10:1 ratio [Ehsani05].

4.6 Electric Energy Consumption

With regards to electric energy consumption, much relies on such subject as vehicle autonomy can be increased due to a better management system and better practices. As described in [Ehsani05], for EVs the energy is usually mentioned in kilowatt-hour (*kWh*) the same as the battery's capacity, hence, the energy consumed in a certain trajectory is kilowatt-hour per kilometer (*kWh km*$^{-1}$). In order to bake the inertial state of a vehicle, the battery output power (4.26) must overcome the resistance, transmission, electronics and motor power losses.

$$P_{b-out} = \frac{V}{\eta_t \eta_m}\left(M_v g(f_r + i) + \frac{1}{2}\rho_a A_f C_D V^2 + M_\delta \frac{dV}{dt}\right)\ [W] \tag{4.26}$$

Where η_t and η_m are the transmission and motor losses, respectively.

As for the regenerative braking, which is the recovery of energy through the braking moment by conducting the motor as a generator, it can be described as (4.27).

$$P_{b-in} = \frac{\alpha V}{\eta_t \eta_m}\left(M_v g(f_r + i) + \frac{1}{2}\rho_a A_f C_D V^2 + M_\delta \frac{dV}{dt}\right) [W] \quad (4.27)$$

Where α is the braking total energy in percentages that can be applied by the motor, described as regenerative braking factor, which is in the range of $0 < \alpha < 1$.

Finally, the net energy consumed from the energy storage source is described as (4.28).

$$E_{out} = \int_{traction} P_{b-out} dt + \int_{braking} P_{b-in} dt \ [Wh] \quad (4.28)$$

4.7 Hybrid Energy Storage Systems in Electric Vehicles

Energy storage systems have an individual set of characteristics which cannot accommodate every consumption requirement as it varies. Therefore, in order to fulfil a certain demand, storage technologies are commonly combined in a better configuration. Such hybridizations often combine great energy and power density outputs as a solution to batteries and supercapacitors weakest points.

The operation of such systems is described in (Fig.4.5).

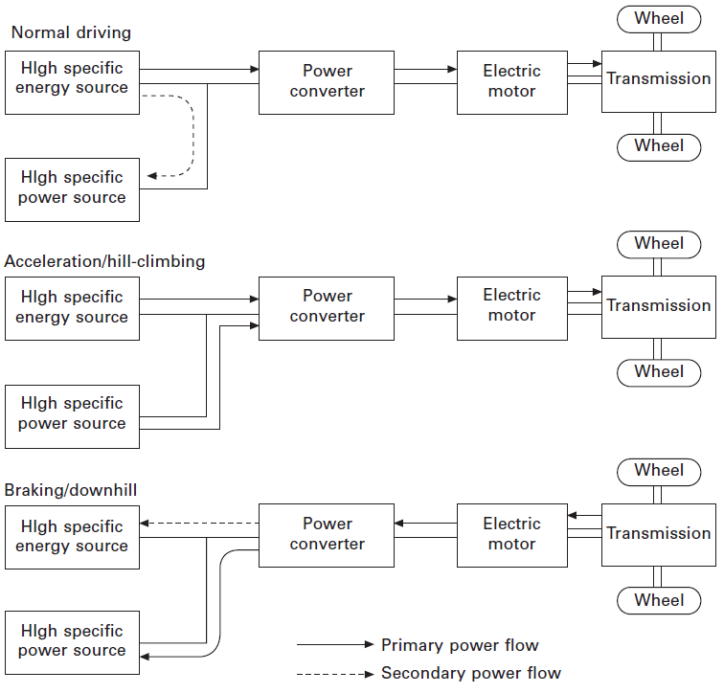

Figure 4.5 – Hybrid energy storage system operation [Chau14]

A common configuration among the possible hybrid energy storage systems is the combination between battery packs and supercapacitor modules, which combined will supply great amounts of energy for longer periods and larger power peaks when in high power demand mode [Zhang16].

4.7.1 Batteries and Supercapacitors – An Efficient Solution

According to [Zhang16], batteries have an average peak power efficiency of about 50% due to its thermal losses dissipated in the equivalent series resistance (ESR), while for supercapacitors, the efficiency stands in 95%.

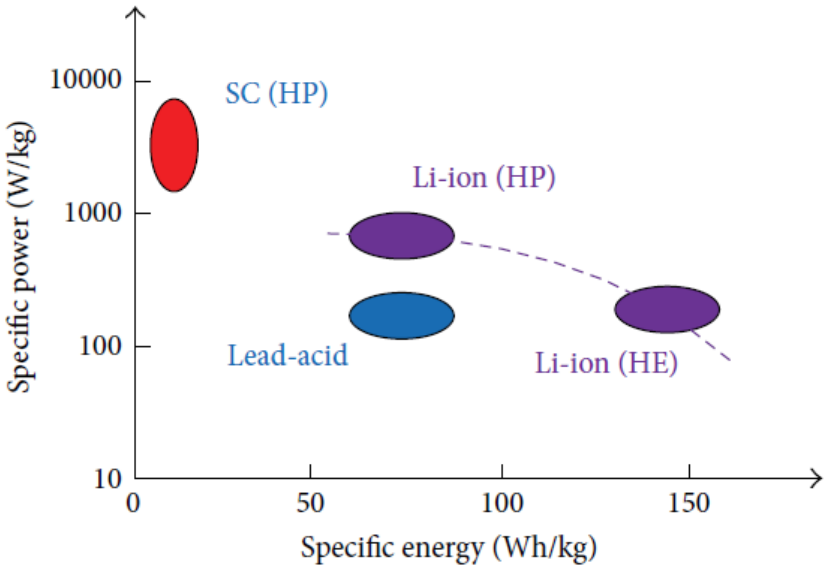

Figure 4.6 – Energy comparison between batteries and SCs [Zhang16]

In supercapacitors, the energy is available almost instantly, at 0.01s, while for batteries the time is increasingly longer due to its storage method.

For hybrid energy storage systems (ESS) the equations for energy density (E_D) and power density (P_D) are described in (4.29) and (4.30) [Niu15].

$$E_{D\_total} = \frac{\sum_{i=1}^{n} E_{D\_i} M_i}{\sum_{i=1}^{n} M_i} \left[\frac{Wh}{kg}\right] \tag{4.29}$$

$$P_{D\_total} = \frac{\sum_{i=1}^{n} P_{D\_i} M_i}{\sum_{i=1}^{n} M_i} \left[\frac{W}{m^3}\right] \tag{4.29}$$

Where M_i stands for the device's masses.

The most common batteries and supercapacitors hybridization setups are depicted in (Fig.4.7-4.10).

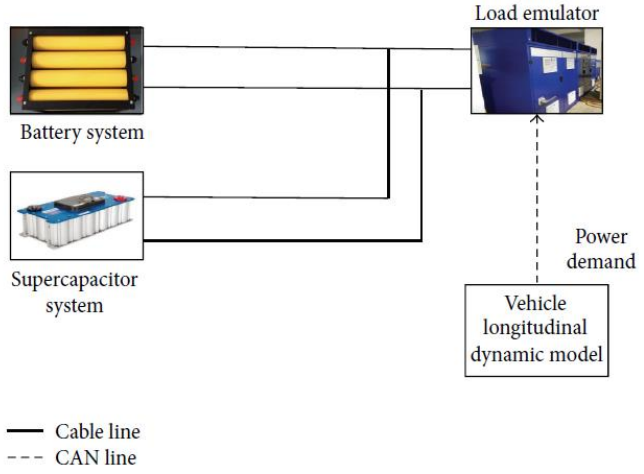

Figure 4.7 – Passive topological structure [Zhang16]

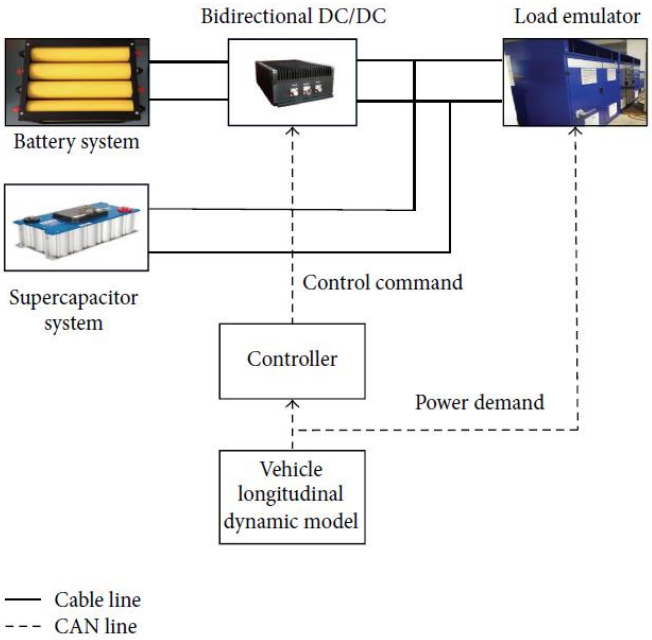

Figure 4.8 – Semiactive topological structure-1 [Zhang16]

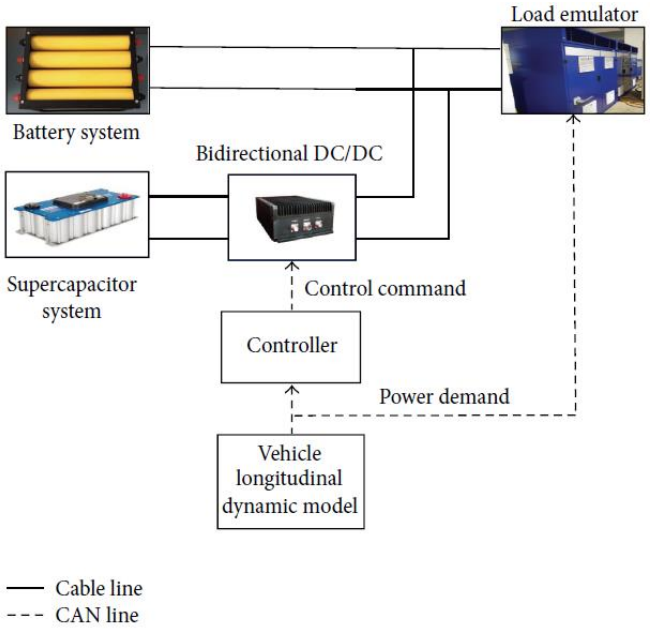

Figure 4.9 – Semiactive topological structure-2 [Zhang16]

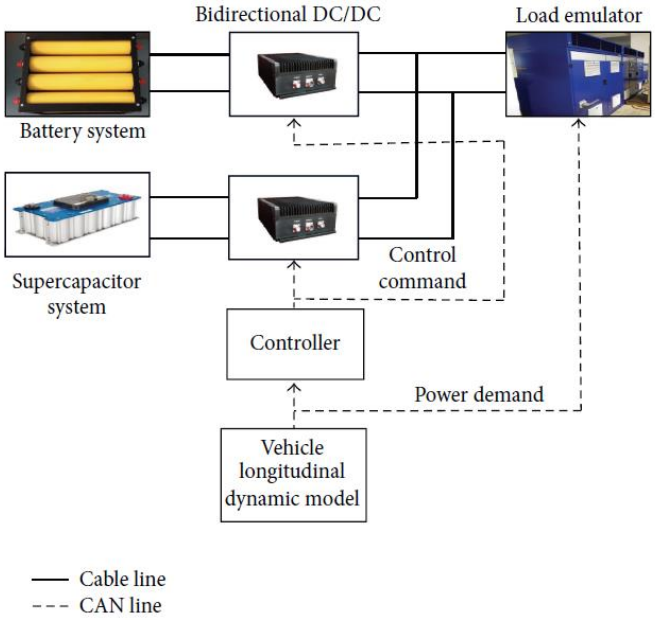

Figure 4.10 – Fully active topological structure-2 [Zhang16]

The passive topological structure is a setup where both devices are directly connected in parallel and, besides being simpler to make, the power distribution is limited by internal resistances. As for the semiactive-1 configuration, the battery pack is connected to a DC-DC boost converter with the intent of reducing the total volume and weight of the pack and better voltage output control. The third structure is with respect to the semiactive-2

configuration, which stands for the same principle of the last setup, however with the DC-DC boost converter connected to the supercapacitor's module. Finally, the fully active structure presents individual DC-DC controller for each of the power sources, representing a more stable and efficient voltage control and power distribution structure [Zhang16].

4.8 Electric Vehicle Computational Model

In order to implement the proposed energy storage systems and understand their interactions with the electric vehicle dynamics, it was chosen to develop a virtual vehicles model so the variants could be simulated. The modelling was performed throughout the software Matlab Simulink 2018b, and it was based mainly in an official simulation example released by the software's developer, MathWorks, more specifically by their Student Competitions Team [MathWorks18a].

With regards to the basis example [MathWorks18a], it concerns the modelling of a Formula SAE car type, with a half vehicle configuration (Fig.4.11) which was considered enough for this dissertation intent as it possesses all the intrinsic and essential vehicle parts, therefore allowing the simulation to be performed within the expected parameters.

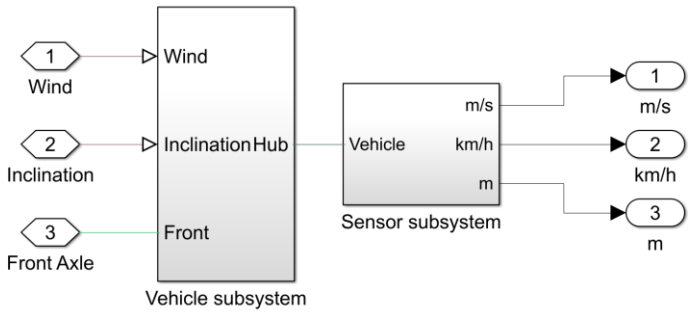

Figure 4.11 – Vehicle block –General view

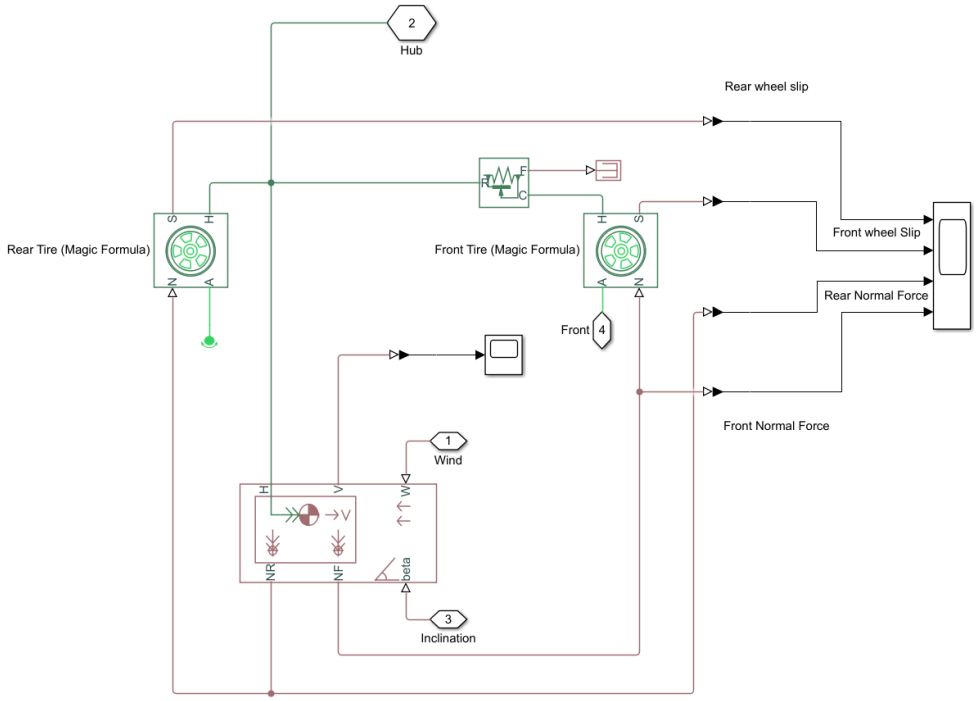

Figure 4.12 – Vehicle subsystem – Half vehicle configuration

The simulation is composed of a vehicle body subsystem (Fig.4.12) which possess the standard two-axle vehicle body block (Fig.4.13-4.15). Such block allows the input of reactionary parameters as mass, gravitation acceleration, axle distances, gravity center and drag coefficient (Fig.4.14-4.15).

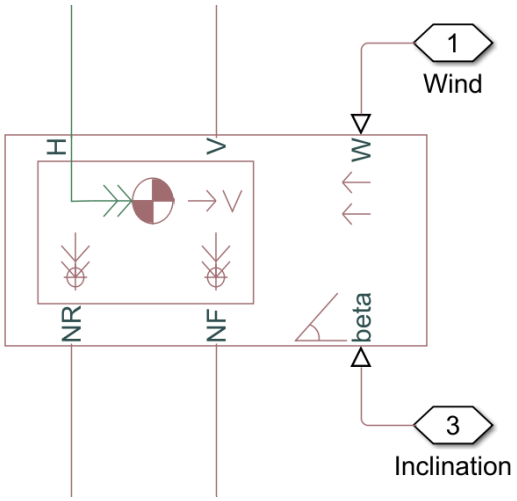

Figure 4.13 – Vehicle body block

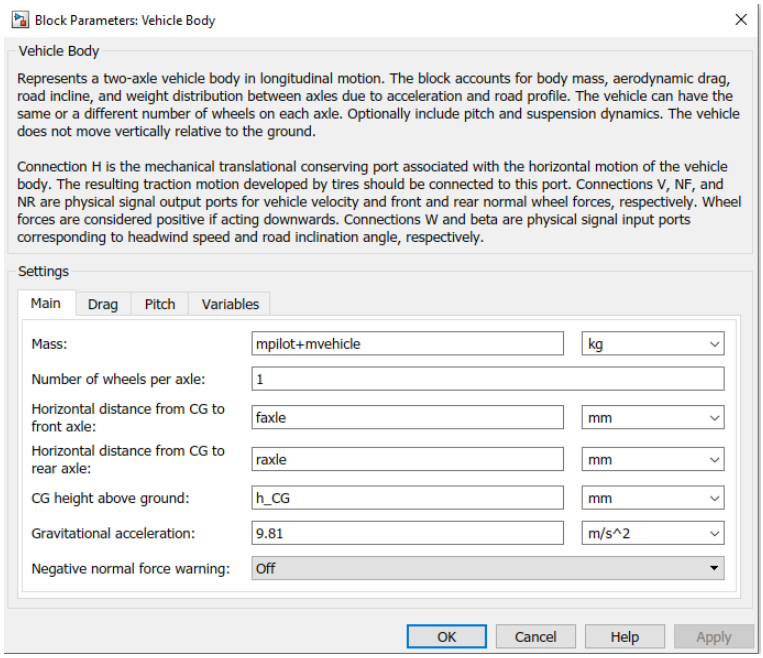

Figure 4.14 – Vehicle body block - Parameters

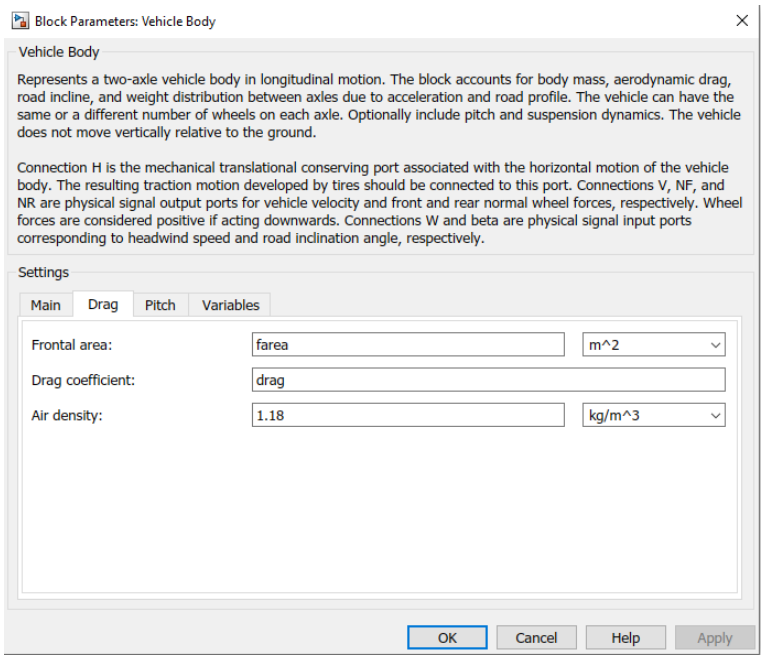

Figure 4.15 – Vehicle body block - Parameters

The subsystem complementary possess two tires (Magic Formula) blocks (Fig.4.17), rear and front, which allows the mechanical integration between the vehicle's motion dynamics and the terrain resistance. Even though the base vehicle model was presented as a Formula SAE car, its structure is considered generic meaning that it can be modified

as suitable once the proper parameters are inserted. With that said, the vehicle type chosen for such simulation was a Carer Electric Forklift, model R45NCF, which was based on [Omar09] and will be further explained in chapter 5. Such vehicle is front driven, configuration which was then represented in the simulation by leaving the rear tire as coupled with a rotational free end block, while the front tire receives an external driving input (Fig.4.12). The parameters implemented in this block are presented in (Table 4.2) and were obtained from [Carer2017] and [Omar09]. In order to obtain the proper gravity center height and frontal area information, a 3D model of the forklift (Fig.4.16) was made according to the dimensional information of both [Carer2017] and [Omar09].

Table 4.2 – Vehicle body parameters

Description	**Parameter**	**Value**
Pilot mass	mpilot	80 kg
Vehicle mass	mvehicle	6950 kg
Gravity center height	h_CG	870 mm
Drag coefficient	drag	1.2
Front axle distance from CG	faxle	800 mm
Rear axle distance from CG	raxle	1150.5 mm
Frontal area	farea	2.25 m^2

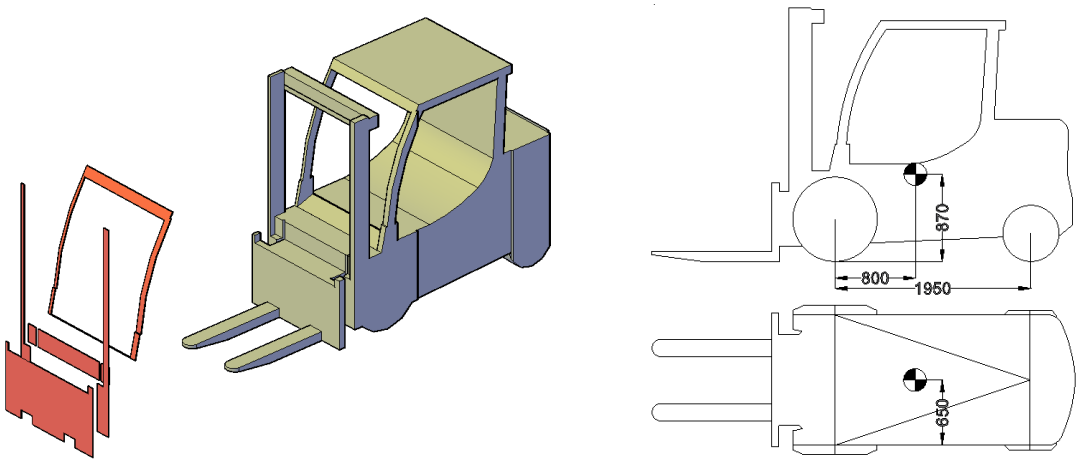

Figure 4.16 – Carer R45NCF electric forklift 2D technical drawing & 3D model

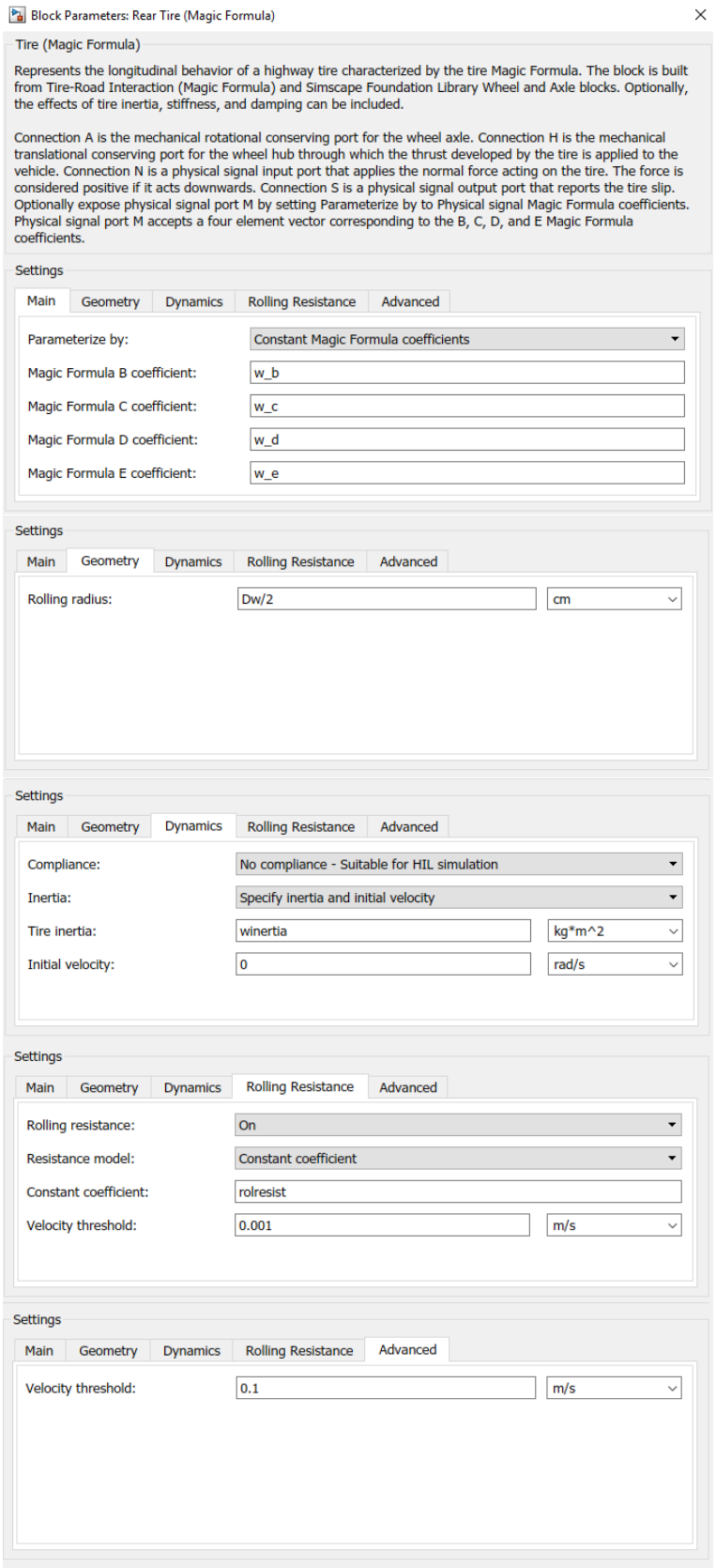

Figure 4.17 – Tyre block - Parameters

The hub (H) ports of each tire are then connected to the ideal force sensor block (Fig.4.12) which transmits the thrust generated by the tires to an output connection (Hub) that, in turn, will be used to measure translational information in the sensor subsystem.

As for the sensor subsystem (Fig.4.18) it receives the thrust input from the vehicle subsystem, which feeds the ideal translational motion sensor (Fig.4.18), with an initial position set as 0 m.

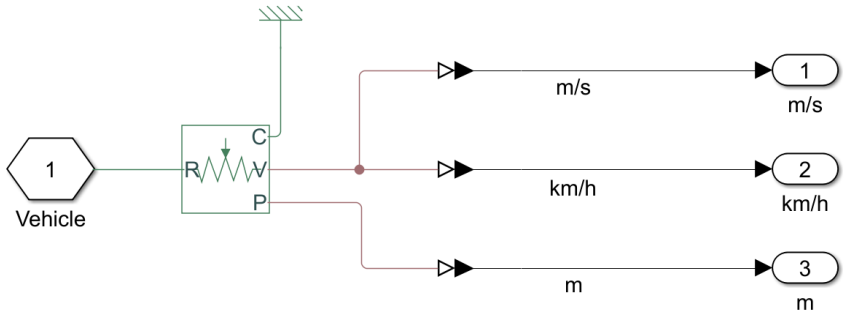

Figure 4.18 – Sensor subsystem

The velocity (*V*) and position (*P*) ports are then connected to scopes allowing the analysis of the outcome.

As noticeable in (Fig.4.11), the complete vehicle subsystem receives three external inputs defined as wind speed, terrain inclination and torque to the frontal axle, parameters which will be further explained in chapter 5.

4.9 Conclusions

The proposed electric vehicle simulation, throughout its subsystems and blocks demonstrates that the mechanical and dimensional structure can be assumed as generic, which allowed the implementation of the Carer forklift's data without any corrective modifications from the basis example.

With regards to the vehicle's dynamic equations, the parametric and prebuilt Simulink blocks mentioned in the previous section performed them automatically by just requiring dimensional and mechanical inputs specific to the study case.

Therefore, the modelled electric vehicle structure was considered enough towards the dissertation intent. With that said, the block interaction with the complete simulation model will be presented in chapter 5, together with the simulation results.

CHAPTER 5

Simulation – Electric Vehicle with Hybrid Energy Storage System

This chapter presents the development of the required computational models in order to observe, analyze and evaluate the interaction effects of a battery-supercapacitor hybrid energy storage system with regards to a certain demand, in this case requested by an electric vehicle. Therefore, a validation simulation of the direct parallel configuration was made to evaluate the effectiveness of the proposed hybridization configuration model towards the hole system. Finally, the gathered data were implemented as hybrid energy storage system to drive the electric forklift model developed in chapter 4.

5.1 Introduction

The electric vehicle considered as basis for this simulation was an electric forklift from the Italian manufacturer Carer, more specifically the model R45NCF (Fig.5.1), however, due to the lack of information regarding this specific model the missing dimensions were assumed to be similar to their newer RC45 H^2 version from the RC45 series, which specifications are presented in (Table 5.1).

Figure 5.1 – Carer R45NCF electric forklift [Carer2019]

Table 5.1 – Carer electric forklift R45 H^2 [Carer2017]

Description	Value
Vehicle mass	6950 kg
Rated capacity	4500 kg
Battery voltage	80 V
Battery capacity	960 Ah
Driven electrical motor	17 kW
Travel speed (laden/unladen)	14.6/17.2 km/h

In [Omar09], the forklift was subjected to an energy storage hybridization between batteries and supercapacitors performing a direct parallel connection, in which the equivalent supercapacitors module was composed of 30 Maxwell 650F 2.7V [Maxwell10] cells connected in series, which parameters are presented in (Table 5.2).

Table 5.2 – Module - Maxwell 650F 2.7V BCAP0650 [Maxwell10]

Parameter	Value
Capacitance	650 F
Voltage	2.7 V
ESR	0.8 mΩ
Cells in series	30

The simulation scheme from [Omar09] (Fig.5.2) presented a traction load current (Fig5.3) interacting with the vehicle hybrid energy storage system.

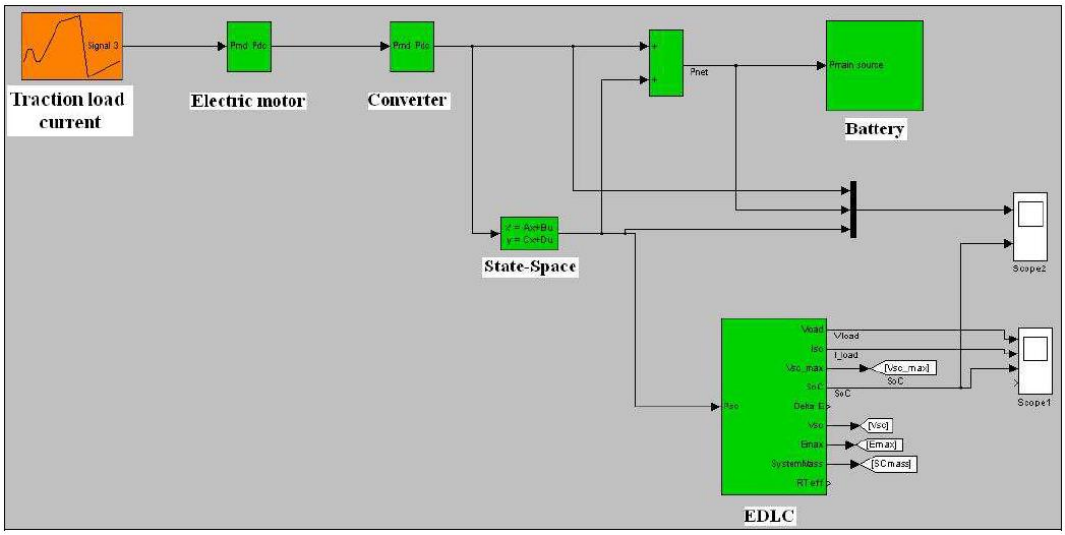

Figure 5.2 – Hybrid battery-supercapacitor forklift simulation scheme [Omar09]

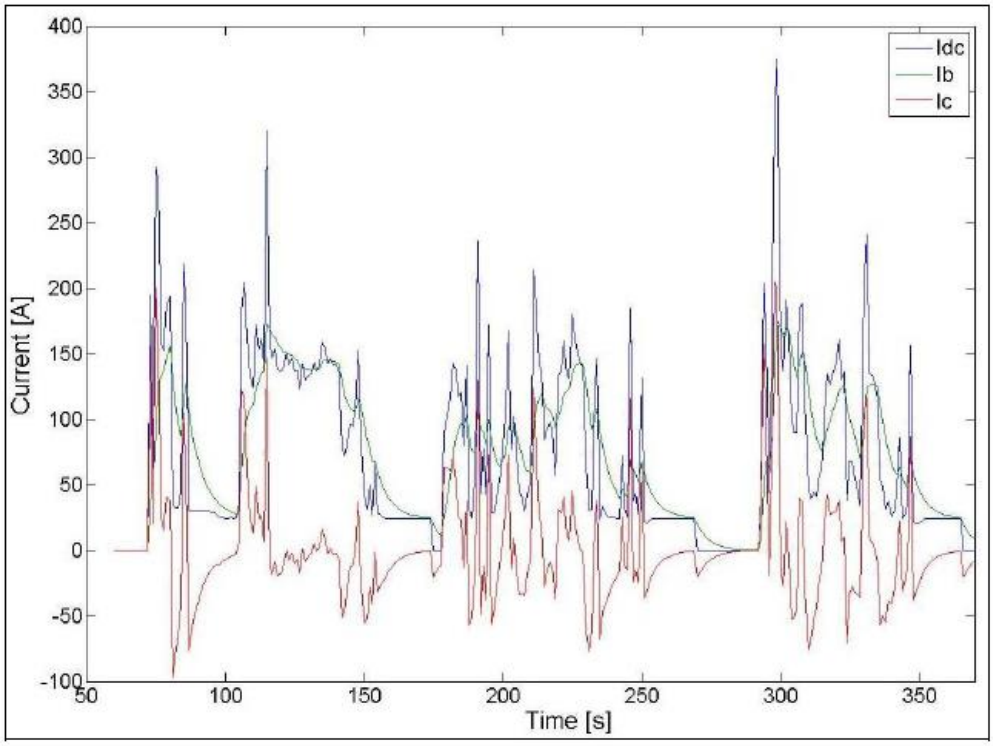

Figure 5.3 – Hybrid battery-supercapacitor forklift simulation current load [Omar09]

Where *Idc* (blue) corresponds to the required current to perform the proposed traction profile, while *Ib* (green) and *Ic* (red) corresponds to the batteries and supercapacitors currents, respectively.

In a battery standalone simulation *Idc* would be entirely required as a battery income, where in the hybridization the supercapacitors module supplied part of the required current, what in theory would contribute to slowing the batteries aging process.

5.2 Hybrid Battery-Supercapacitor Data Validation

In order to validate the experiment proposed in [Omar09], the *Idc* load profile was extracted from (Fig.5.3) throughout the software AutoCAD 2014 and implemented in a corresponding simulation structure performed in Matlab Simulink 2018b (Fig.5.4).

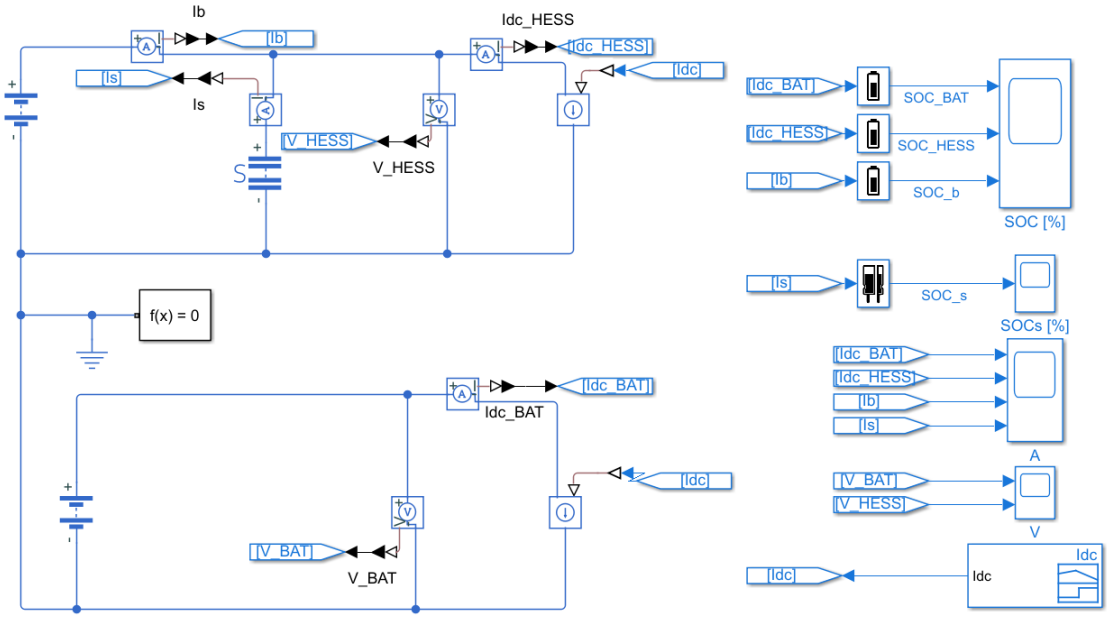

Figure 5.4 – Hybrid battery-supercapacitor test simulation - Validation [Omar09]

Where the upper composition corresponds to the hybrid energy storage system, while the bottom one is related to the battery in a standalone configuration. The *Idc* profile was implemented throughout a signal builder block supplying both systems.

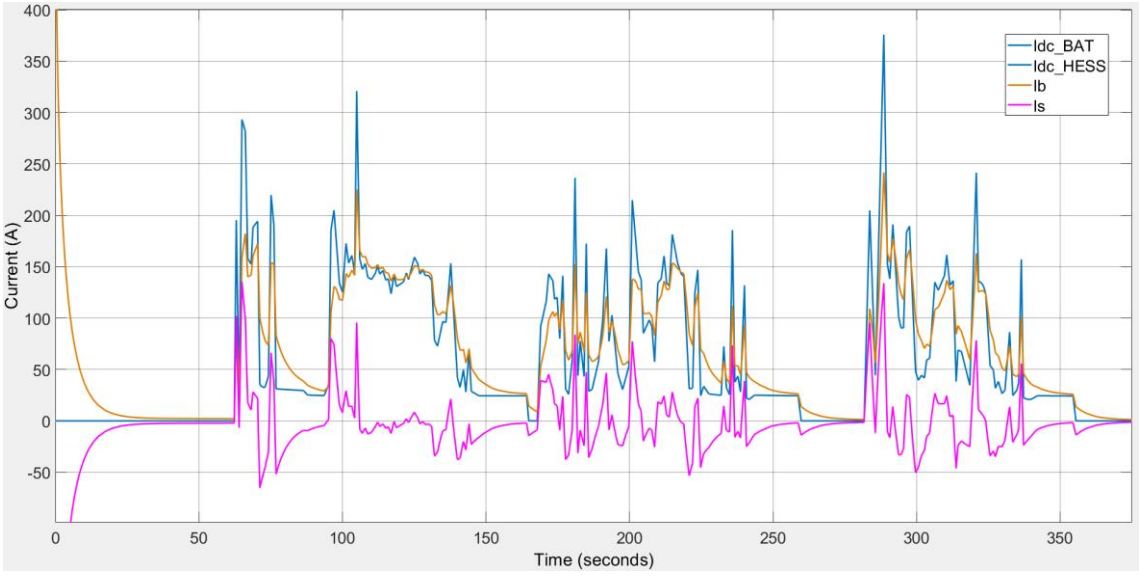

Figure 5.5 – Idc load profile - Validation

Despite the lack of information, the similarity between the extracted *Idc* (blue), *Ib* (orange), *Is* (*Ic* in [Omar09]) (magenta) (Fig.5.5) and the original from [Omar09] (Fig.5.3) was considered sufficient to perform the intended simulation. In (Fig.5.5) it is

possible to notice that the supercapacitor current is supplying part of the load demand just as described in [Omar09]. From such results one can hypothesize that the reduction in current demand from the battery contributes for the increasing in its life cycle as such property is directly related to state of charge time when interpreted by the Coulomb counting method (5.1) [Murnane17]. It was verified that the currents in the hybrid configuration are in fact a decomposition from the load current implemented, which values correspond to the sum of both batteries and supercapacitors currents.

$$SOC = SOC(t0) + \frac{1}{Q_{rated}} \int_{t0}^{t0+\tau} i(t)\, dt \ \ [\%] \tag{5.1}$$

As for the required voltage, the hybrid battery-supercapacitor simulation (red) reduced the voltage peaks and drops, in a way smothering the profile when compared with the standalone setup (blue) (Fig.5.6). For the analysis, four different moments were selected, *t1* = 60 s, *t2* = 104.9725 s, *t3* = 167.854 s and *t4* = 288.587 s. The related measurements for the hybrid configuration (red) have shown a reduction in voltage in the initial moment (*t1*), characterized by a steady situation before the start of load demand, of 0.2V, not reaching the same as for the battery standalone configuration, 76.4V. This occurs due to the supercapacitors initial charge supplied by the battery, as it can be observed in (Fig.5.5). In both *t2* and *t4* a voltage retention was noticed, with 6.8V and 9.5V respectively towards the alone configuration. This is consequence of the reduction in current with regards to the battery's internal resistance. Finally, in *t3* a charge characteristic is presented which demonstrated a reduced demand in the hybrid setup towards the battery alone, which peak is reached with a less oscillating curve, caused by the very same reason as described for *t2* and *t4*.

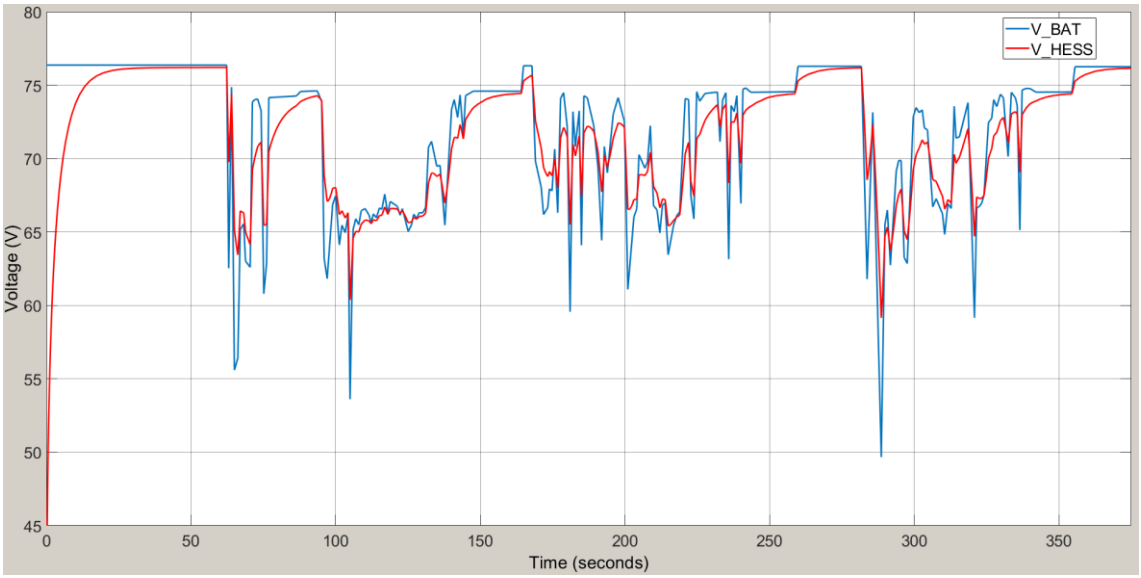

Figure 5.6 – Required voltage – Validation

As one can observe, the requested voltage is then filtered when subjected to hybridization due to the supercapacitor's module. Such reduction, as this result is interpreted, causes a battery stress reduction. According to [POWER16], high voltages tend to drive the battery towards higher positive plate corrosion rates. Therefore, that is a valid experiment result when considering the extension in the device's life cycle.

5.3 Hybrid Battery-Supercapacitor Lifespan Extension Hypothesis Analysis

In order to analyze the supposed lifespan extension of a battery under hybridization, a constant current (*CC*) charge and discharge (full cycle) simulation, performed in Matlab Simulink 2018b, was designed concerning the resulting difference in the amount of possible full cycles per a total period of 30 hours (108.10^3 s) (Fig.5.7).

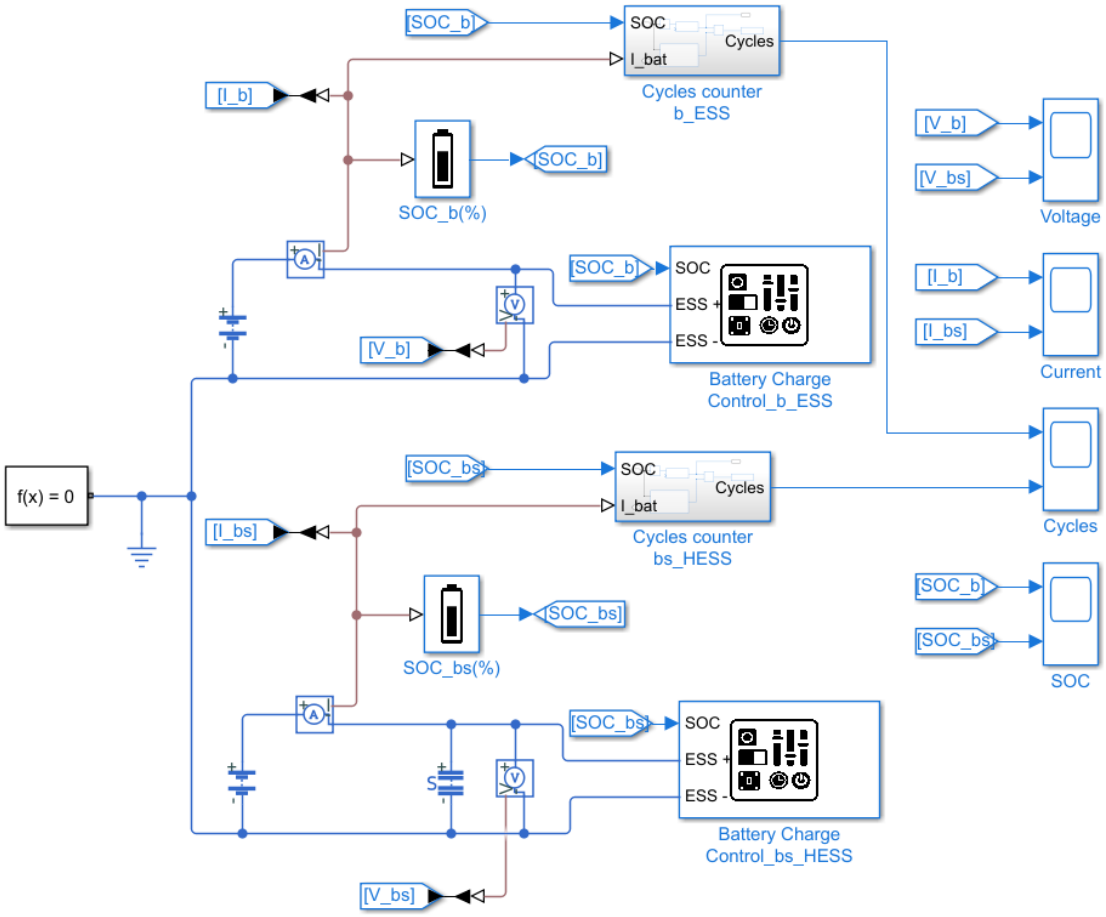

Figure 5.7 – Charge and discharge simulation at constant current

As one can notice, the simulation is composed of two separated compositions (Fig.5.7). The top structure concerns the battery standalone scenario, where the bottom one is designed to represent the hybrid energy storage system.

As components, both compositions possess, besides the energy storage systems, a charge control and cycles counter subsystems (Fig.5.8-5.11).

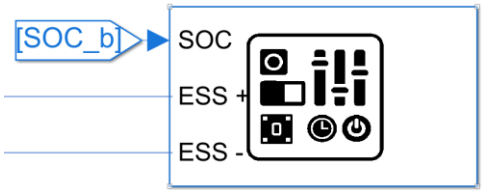

Figure 5.8 – Charge control subsystem

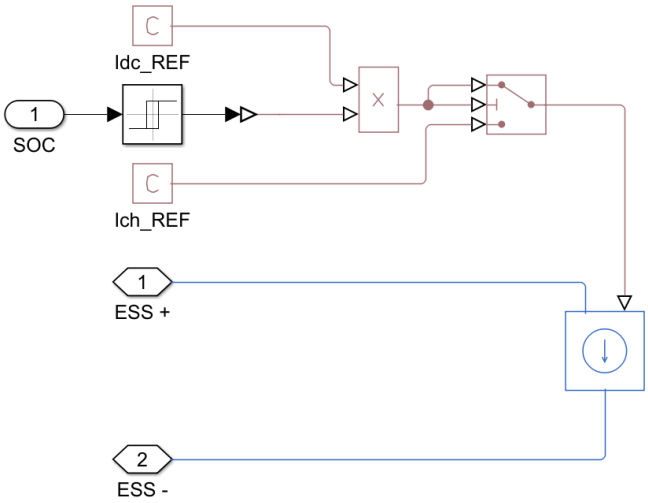

Figure 5.9 – Charge control subsystem

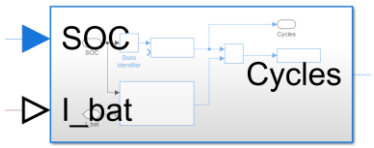

Figure 5.10 – Cycles counter

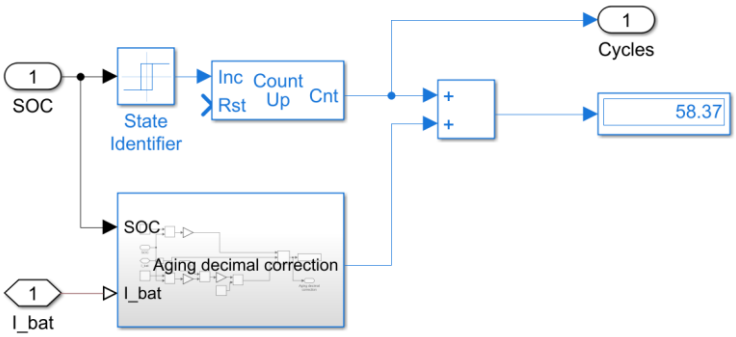

Figure 5.11 – Cycles counter

The current control subsystem (Fig.5.9) is controlled by the state of charge of the battery, which is then connected to a relay with switch on value set as 80% and switch off as 20%, battery lifetime increasing SOC range [Surendar15]. When the switch is defined as opened, the output is set to 1, while 0 is forwarded when closed. The relay output is then multiplied by the discharge current (*Idc*) resulting in either a null value or the current itself. This reference is then input as threshold into a switch. For values greater than or equal to it, the switch is then connected to the first input (*Idc*), while for negative values

it be connected to the second input (*Ich*). This series of events will define the full cycle profile.

As for the cycles counter (Fig.5.11), it was designed in order to count each complete cycle so its evolution in relation to the time could be analyzed. This subsystem is composed of a relay (state identifier) that works in the very same way as previously described for the current control subsystem. The state identifier output is then counted by the count up block, which then outputs integer values. With the intent of computing the fractional values from incomplete cycles, the aging decimal correction block was designed based on (5.2) for *i(t)* > 0 (*Idc*) and (5.3) for *i(t)* <= 0 (*Ich*), developed empirically by experimentation throughout Simulink battery block (*Simscape / Electrical / Specialized Power Systems / Electric Drives / Extra Sources*) behavior analysis.

$$CCR_{Idc} = \frac{SOC_{max} + SOC(t)}{\Delta SOC} . \tau dc . 100\ [\%] \tag{5.2}$$

$$CCR_{Ich} = \left(\left(1 - \frac{SOC_{max} + SOC(t)}{\Delta SOC} \right) \tau ch + \tau dc \right) 100\ [\%] \tag{5.3}$$

Where *CCR* stands for complete cycle rate, SOC_{max} is the upper state of charge limit, *SOC(t)* is the instant state of charge value supplied by external input, *ΔSOC* is the difference between the upper and lower state of charge limits and *τdc* and *τch* are the proportionality coefficients of a complete cycle (5.4-5.5).

$$\tau dc = 1 - a \tag{5.4}$$

$$\tau ch = a \tag{5.5}$$

Where a is defined as the relation between charge and discharge current proportions towards the total current (5.6).

$$a = \frac{Idc}{Idc - |Ich|} \tag{5.6}$$

Therefore, with the presented simulation and according to the battery and supercapacitor values for the bench test [Omar09] the parameters were defined. However, it is important to say that even though the energy storage devices were mentioned, there was a difficulty in interpreting the remaining parameters which led to the assumption of some values as charging current and cycle profile. The parameter implemented into the simulation are presented in [Table 5.3].

Table 5.3 – Charge and discharge simulation at constant current - Parameters

Parameter	**Value**
Battery Voltage	12 V
Battery capacity	57 Ah
Battery resistance	2.5 mΩ
Battery - Series	1
Battery - Parallel	1
Supercapacitor Voltage	2.7 V
Supercapacitor capacitance	600 F
Supercapacitor - Series	6
Supercapacitor - Parallel	2
Simulation time	30 h

The simulation was performed as previously described, which the hybrid energy storage system results corresponded to the expectations with the relative smothering of battery current curves (blue) supported by the supercapacitor input (black) when compared with the system load (red) (Fig.5.12), wider cycles (charge and discharge events) (Fig.5.14) and prolongation of the time to reach the hypothetical maximum cycles limit (Fig.5.15).

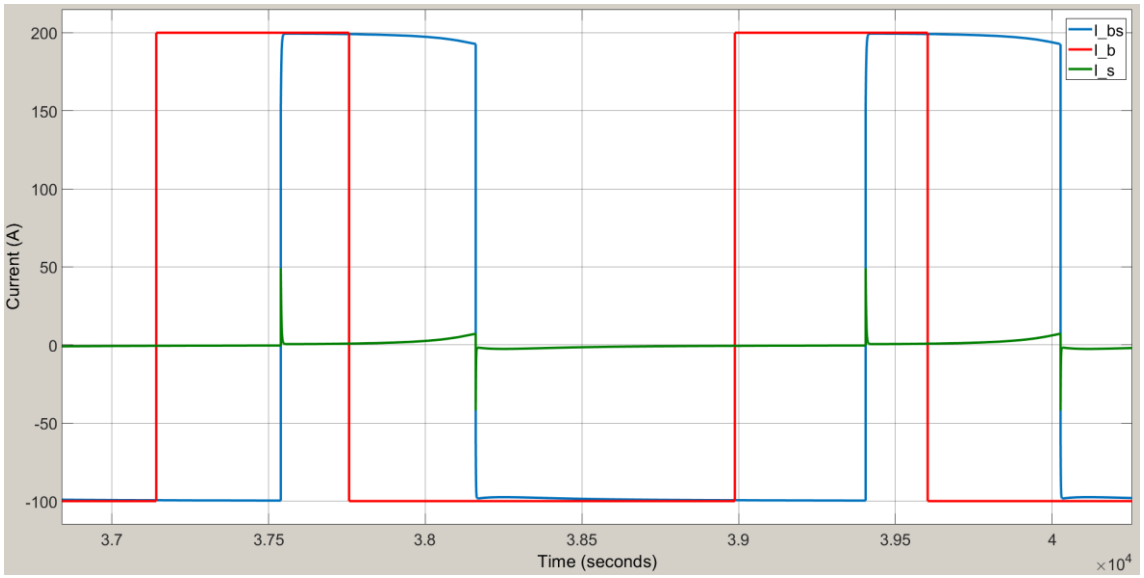

Figure 5.12 – Charge and discharge simulation at constant current - Current

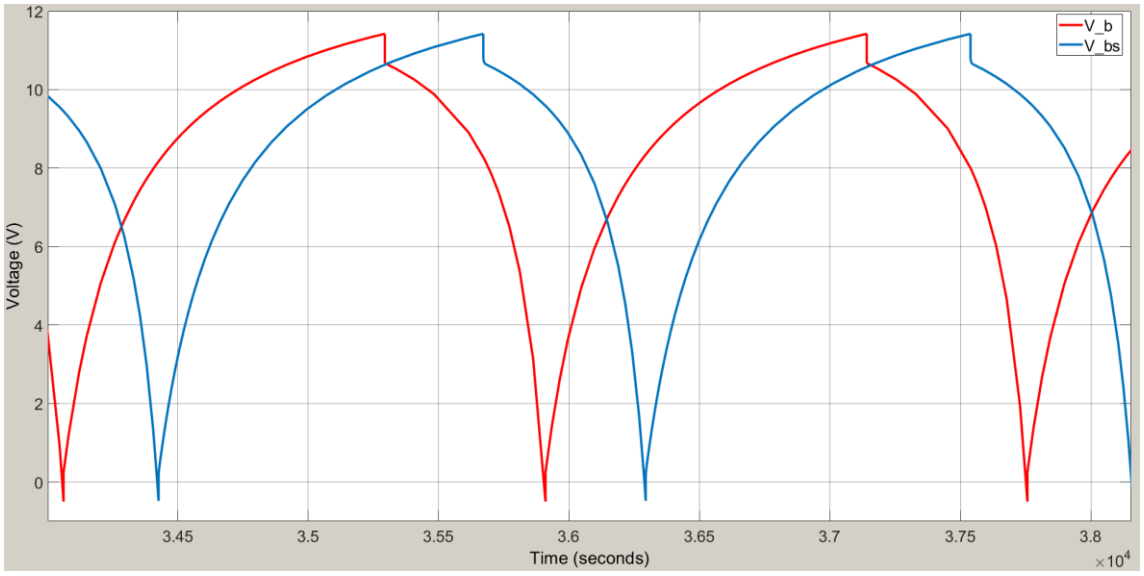

Figure 5.13 – Charge and discharge simulation at constant current - Voltage

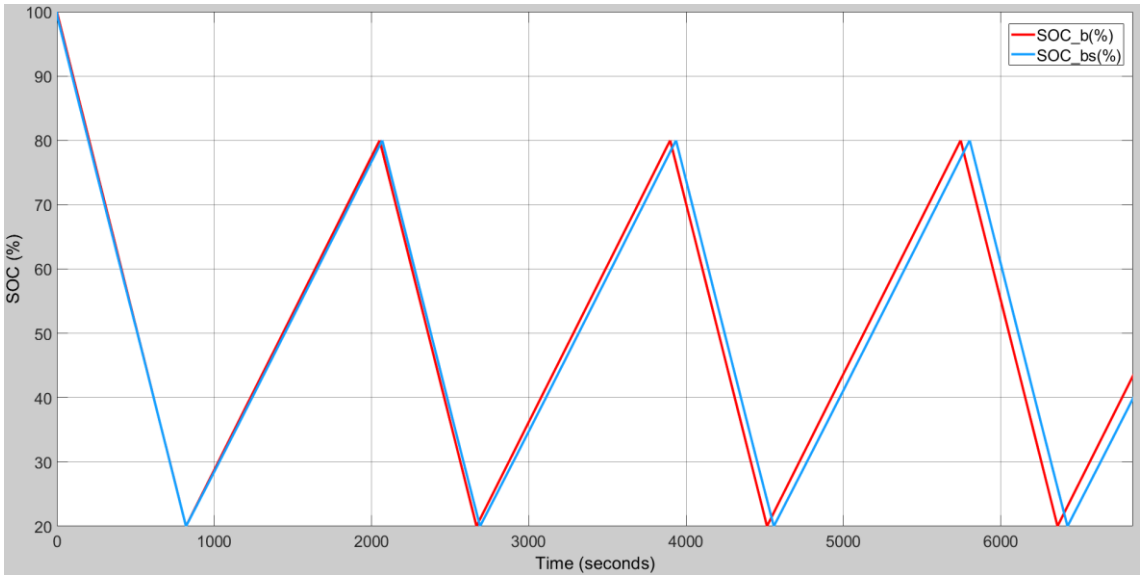

Figure 5.14 – Charge and discharge simulation at constant current - SOC

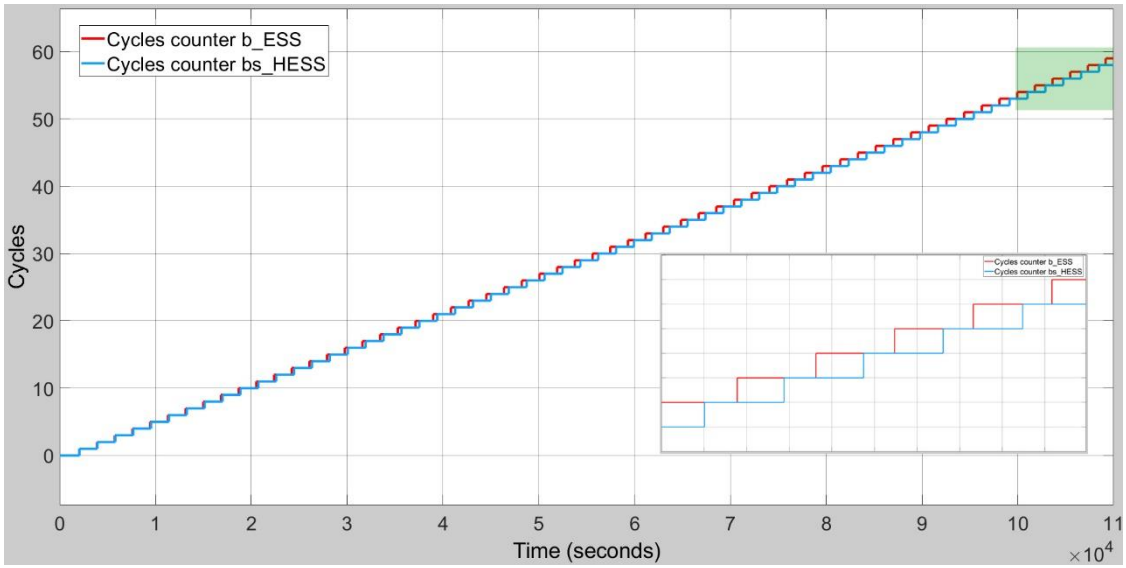

Figure 5.15 – Charge and discharge simulation at constant current - Cycles

In (Fig.5.12) the currents behavior is essentially reproducing what was presented by [Omar09] and validated in (Fig.5.5), where the supercapacitor supplies part of the system demand. For the battery standalone simulation, the implemented discharge and charge currents (red) were of 200 A and -100 A, respectively, while for the battery in hybrid configuration (blue) the registered was 199 A and -99.6 A. As for the supercapacitors (green), they supplied an auxiliary discharge current of 49.1 A at the very same moment of the battery initial discharging peak, instantly dropping to 0.572 A and smoothly increasing until it reached 7.35 A, at the end of the discharge cycle. From that point the

current initialized then its charging cycle decreasing to -42 A. This interaction is reflected in the round corners of the battery current profile for the hybrid setup and reduction in peak-to-peak size, where it supplies the charge cycle of supercapacitors.

With regards to the voltage (Fig.5.13), both systems presented the same peak-to-peak profile and values of 11.4 V and -0.5 V, however with different wave periods due to the reduction in battery demand while in hybrid configuration, 1847 s and 1885 s for the battery alone and hybrid setups, respectively.

The resulting state of charge (SOC) comparison of both setups (Fig.5.14) reflected the current demand reduction in the case of hybridization, where the SOC wave period was enlarged (blue) when compared to the battery standalone output (red). For the standalone configuration the full cycle was obtained with $\Delta t \approx 1847$ s, while for the hybrid setup the battery registered a full cycle period of $\Delta t \approx 1885$ s, reflecting an extension of more than 2%.

Hence, the increased state of charge period caused the number of cycles (Fig.5.15) to be reduced over the total simulation time, from 58.4 to 57.3 cycles. The result can be interpreted as a hypothetical increase in the battery life due to the possibility of performing its role to the system with lesser charging and discharging events, therefore, postponing the deduction of cycles from the device's total rated cycle lifetime. Thus, the state of charge extension was proportionally reflected here as a number of cycles reduction, 2% over the same period, causing the battery under the supercapacitors support to only reach the same number of cycles of the standalone setup after additional 2176 s, i.e. 36 minutes, approximately.

Therefore, based on the simulations results so far it is valid to conclude that the direct parallel hybridization between battery packs and supercapacitor modules generate promising results towards the extension in electrochemical batteries lifespan by the reduction of battery current demand over the requested current load from the system.

5.4 Electrical Forklifts with Hybrid Battery-Supercapacitor Energy Storage System

Finally, in order to evaluate the effect of previously mentioned and simulated data, either from [Omar09] or as result of this dissertation, an electric forklift simulation was developed in Matlab Simulink 2018b.

The simulation (Fig.5.16) was configured as a passive topological structure (chapter 4, section 4.7.1) divided in two configurations, battery standalone and hybrid energy storage system, under the vehicle's parameters mentioned in chapter 4, however subjected to the supercapacitors definitions presented in chapter 3, for both the Maxwell 300F 2.3V pseudocapacitor and the Ni-Cu hybrid supercapacitor modeled. Complementary electrical definitions extracted from [Omar09] and presented in section 5.2 were implemented, such as current load and battery pack definition.

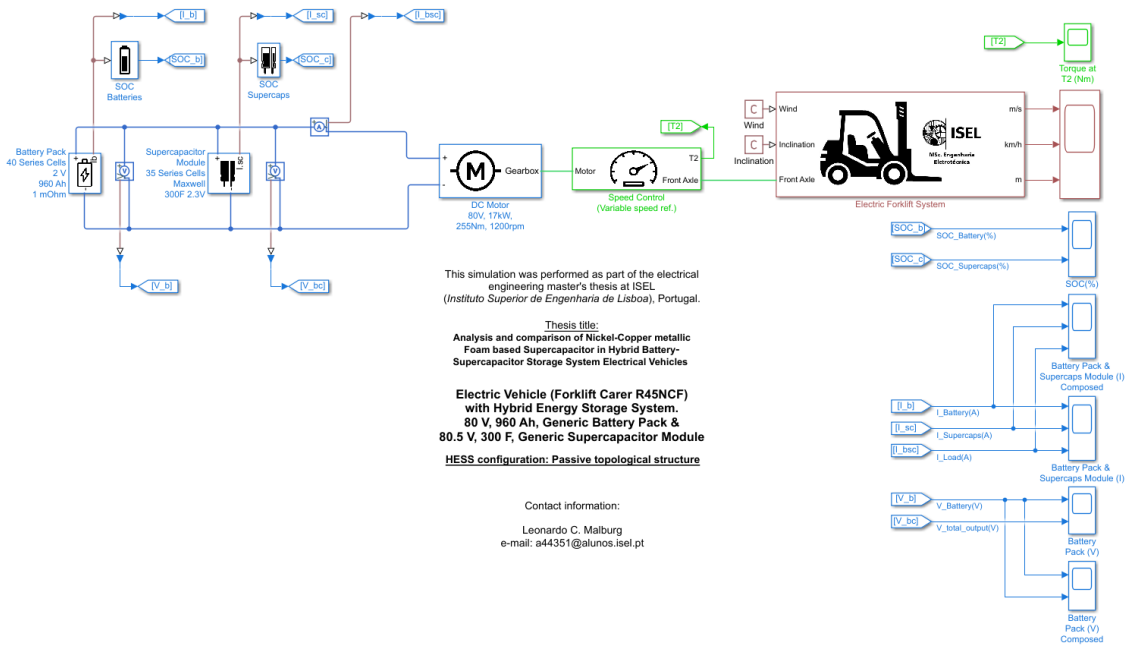

Figure 5.16 – Electric Forklift with hybrid battery-supercapacitor energy storage system

Besides the aforementioned components, the simulation presents two other subsystems, the DC 17 kW 80 V motor and the speed controller.

The motor definitions were based on the Carer R45NCF specification [Omar09] and [Carer2017] and, due to the lack of information regarding is properties, supported by the combination of definitions from three different manufacturers suppliers of similar products, the Italians AMRE [AMRE15] (Fig.5.17) and Sicmemotori [SICME02] and the German Baumüller [BAUM13]. In order to implement a DC motor into the simulation structure, the DC motor block (Fig.5.18) was chosen which required several input parameters obtained from the previously mentioned references and described in (Table 5.4).

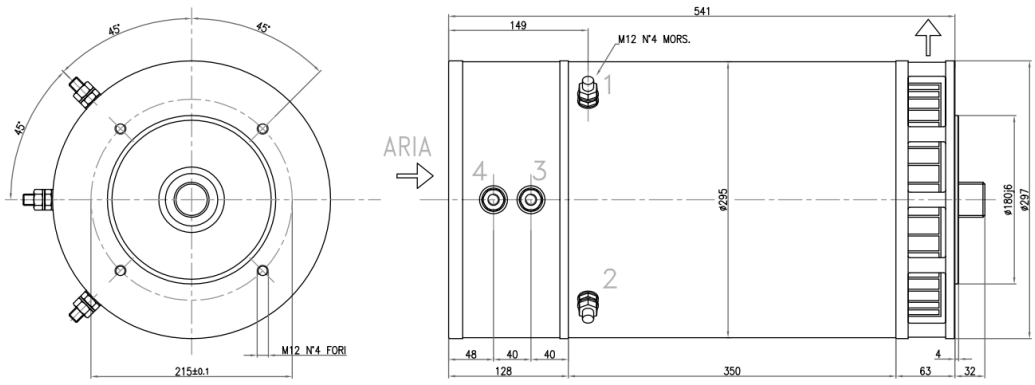

Figure 5.17 – AMRE 17kW 80V forklift DC motor [AMRE15]

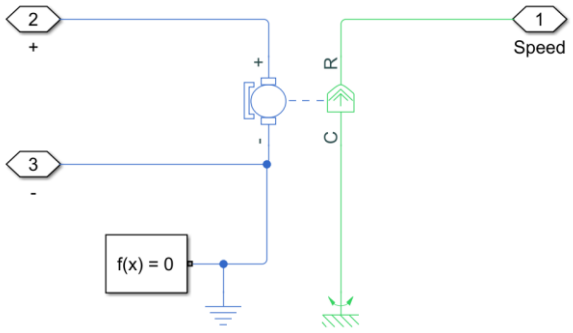

Figure 5.18 – Simulink DC motor block

Table 5.4 – Simulink DC motor block - Parameters

Parameter	Value
Power	17 kW
Voltage	80 V
Current	259 A
Armature inductance	26.86 mH
Torque	255 N.m
No-load speed	1200 rpm
Rotor inertia	44.1 kg m^2

From the implemented block parameters, armature inductance, torque and rotor inertia were obtained from [SICME02] and [BAUM13].

The armature inductance was based on the GNA 132 SN DC motor of Baumüller [BAUM13] with a value of 22.5 mH, (5.7) and the American Wire Gauge (AWG) standard sizes [POWERSTREAM19].

$$L = \frac{\mu N^2}{l} A\ [H] \tag{5.7}$$

Where L is the inductance, μ is the medium permittivity, N is the number of turns, l is the length of the conducting wire (m) and A stands for the wire area (m^2).

As the motor from [AMRE15] has a rated current of 259 A and the one from [BAUM13] 42 A, similar references were chosen in [POWERSTREAM19]. For a maximum current of 47 A the minimum conductor's diameter and area should be 2.3038 mm and area of 4.17 mm^2, while for a maximum of 283 A, 9.266 mm and 67.4 mm^2. The increase in diameter and area, 4.3 and 16.2 times, respectively, were proportionally scaled for the AMRE motor based on (5.7-5.9).

$$l = N\sqrt{c^2 + p^2}\ [m] \tag{5.8}$$

$$H = N.p\ [m] \tag{5.9}$$

Where c is the circumference of the coil, p is the pitch, here considered as the wire diameter D and H is the core's height.

By considering that the total height of the coil, regarding its winding on a generic core, will not change since the structure is the same, with a proportionality approach it's possible to estimate that the required N (N_p) will be only 0.23 times of its original value for a pitch increase of 4.3 times (5.10).

$$N_p = \frac{H}{p \times 4.3} = \frac{1}{1 \times 4.3} = 0.23 \tag{5.10}$$

From that, considering no change in the circumference of the coil (c), the decrease in l was calculated as 71.8% of its original value (5.11-5.13).

$$l_p = N\sqrt{c^2 + p^2} = 1\sqrt{1^2 + 1^2} = 1.414 \tag{5.11}$$

$$l'_p = N.N_p\sqrt{c^2 + (p \times 4.3)^2} = 1\ x\ 0.23\sqrt{1^2 + (1 \times 4.3)^2} = 1.0154 \tag{5.12}$$

$$l'' = \frac{l'_p}{l_p} = 71.8\ [\%] \tag{5.13}$$

Therefore, as the permittivity does not change, based on the same idea and on (5.7), the proportional inductance was 26.86 mH (5.14-5.15).

$$L_p = \frac{\mu(N \times 0.23)^2}{l \times 0.718}\ (A \times 16.2) = 119.36\ [\%] \tag{5.14}$$

$$L_{new} = 0.0225 \times 1.1936 = 0.02686\ [H] \tag{5.15}$$

The rotor inertia was assumed the same as for the GNA 132 SN DC motor [BAUM13], 44.1 kg m2, as both motors are sufficiently similar when considering external dimension and total masses, once no other values should affect the resulting inertia when based on (5.16) [Protec60, Protec91].

$$J = m\left(\frac{D}{2\pi}\right)^2 \ [kg\ m^2] \tag{5.16}$$

Where m is the total moving mass (kg) and D is the lead screw diameter (m).

In order to implement the load current profile from [Omar09], the current values were converted into angular velocity (rad s^{-1}) input reference (Annex 3). The procedure was made by tracing the voltage profile for the hybrid setup presented in [Omar09] throughout AutoCAD 2018, values which when multiplied by the current resulted in a power value for the instant t ($P(t)$). The proportionality of $P(t)$ towards the nominal power was calculated and then applied to the unladen maximum speed of the forklift [Carer17], 17.2 km/h, i.e., 11.37 rad s^{-1}.

The speed control subsystem (Fig.5.19) was designed in a way that a signal builder could input the speed reference into the system. For that to be made, an ideal angular velocity source block was used, which is based on (5.17).

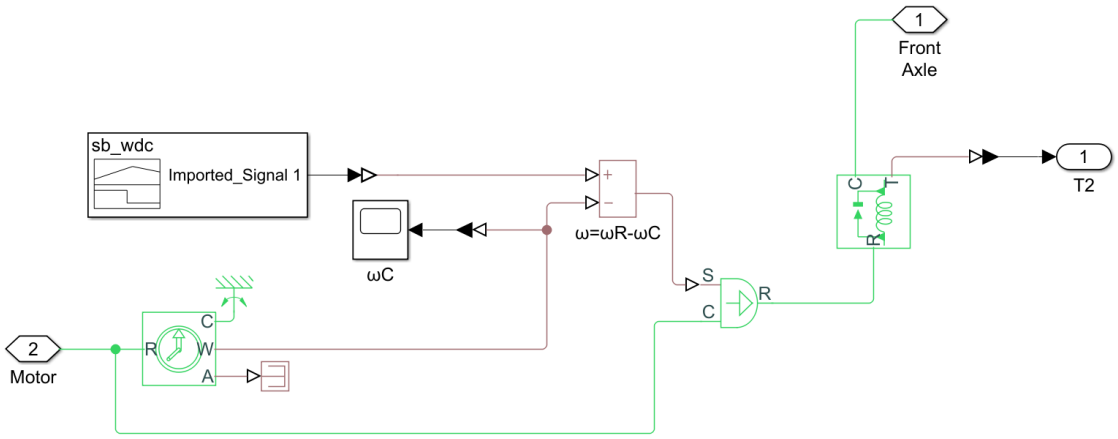

Figure 5.19 – Speed control subsystem block

$$\omega = \omega R - \omega C \ \left[\frac{rad}{s}\right] \tag{5.17}$$

Where ω is the input speed reference, ωC and ωR are the absolute angular velocities of terminals C and R, respectively.

The hybrid energy storage system is described in (Table 5.5).

Table 5.5 – Electric Forklift with hybrid battery-supercapacitor - Parameters

Parameter	Value
Battery Voltage	2 V
Battery capacity	960 Ah
Battery resistance	1 mΩ
Battery - Series	40
Battery - Parallel	1
Supercapacitor volt. Maxwell	2.3 V
Supercapacitor cap. Maxwell	300 F
Supercapacitor – Series - Maxwell	30
Supercapacitor – Parallel - Maxwell	1
Supercapacitor volt. Ni-Cu	2 V
Supercapacitor cap. Ni-Cu	454 F
Supercapacitor – Series – Ni-Cu	40
Supercapacitor – Parallel – Ni-Cu	1
Simulation time	375 s

The resulting current profile with both Maxwell and Ni-Cu supercapacitors, (Fig.5.20) displays the same behavior observed on [Omar09] and validated in section 5.2, with significant reduction in the battery pack current demand (magenta) towards the load current (black), caused by the supercapacitor's support (blue). With regards to the resulting current difference between both devices, four points on the graph were analyzed, *t*= 172.89, 198.08, 201.88, 375 s, where it was verified that in the case of the Maxwell pseudocapacitor it displayed reduced current values while in charging mode (198.08 s, 375 s), 154.745 A and 49.294 A, towards the observed at the very same moments for the Ni-Cu simulation, 161.4 A (+4.3%) and 50.016 A (+1.46%). These datapoints are characterized by descending patterns, which can be interpreted by a reduced load current and moments of supercapacitors charging, where the Maxwell device has demonstrated lesser current contributions to the battery during charge peaks. However, in discharging operation modes (172.89 s, 201.88) the hybrid Ni-Cu supercapacitor displayed smaller current demand from the battery, 499.247 A and 559.938 A, towards the Maxwell

pseudocapacitor, 509.976 A (+2.15%) and 581.187 A (+3.8%), therefore a greater contribution regarding the implemented load. It is an expected output as the charge is greater for the Ni-Cu device and in the immediate branch it is related to the current as described in (5.18-5.19) [Lahyani13, Zubieta00].

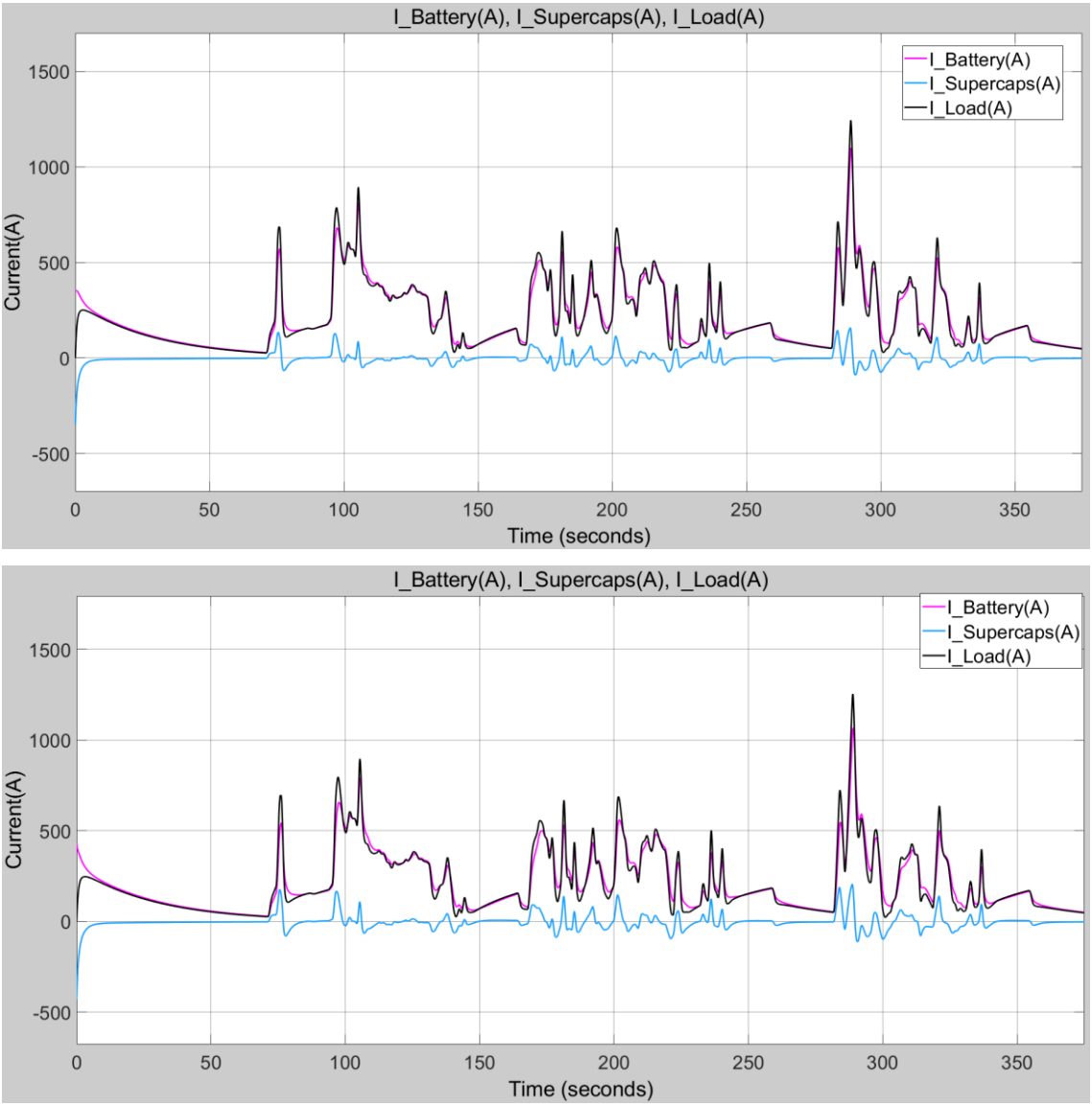

Figure 5.20 – Current profile. a) Maxwell 2.3V 300F, b) Ni-Cu 2V 454F

$$Q_{total} = Ich(t_4 - t_1)\ [C] \tag{5.18}$$

$$Q_1 = C_{0i}V + \frac{1}{2}K_v V^2 = \int (C_{0i} + K_v V)\, dV\ [C] \tag{5.19}$$

The voltage profiles presented by the three setups (Fig.5.21), standalone battery, and hybrid energy storage systems with Maxwell and Ni-Cu devices, also behaved as expected, with a voltage reduction in hybrid cases towards the voltage measured for the battery alone. In Maxwell hybrid, the reduction in voltage slopes was significant, of about 5.05 V. As for the Ni-Cu hybrid supercapacitor, the reduction was more preeminent, with slopes difference of about 6.4V.

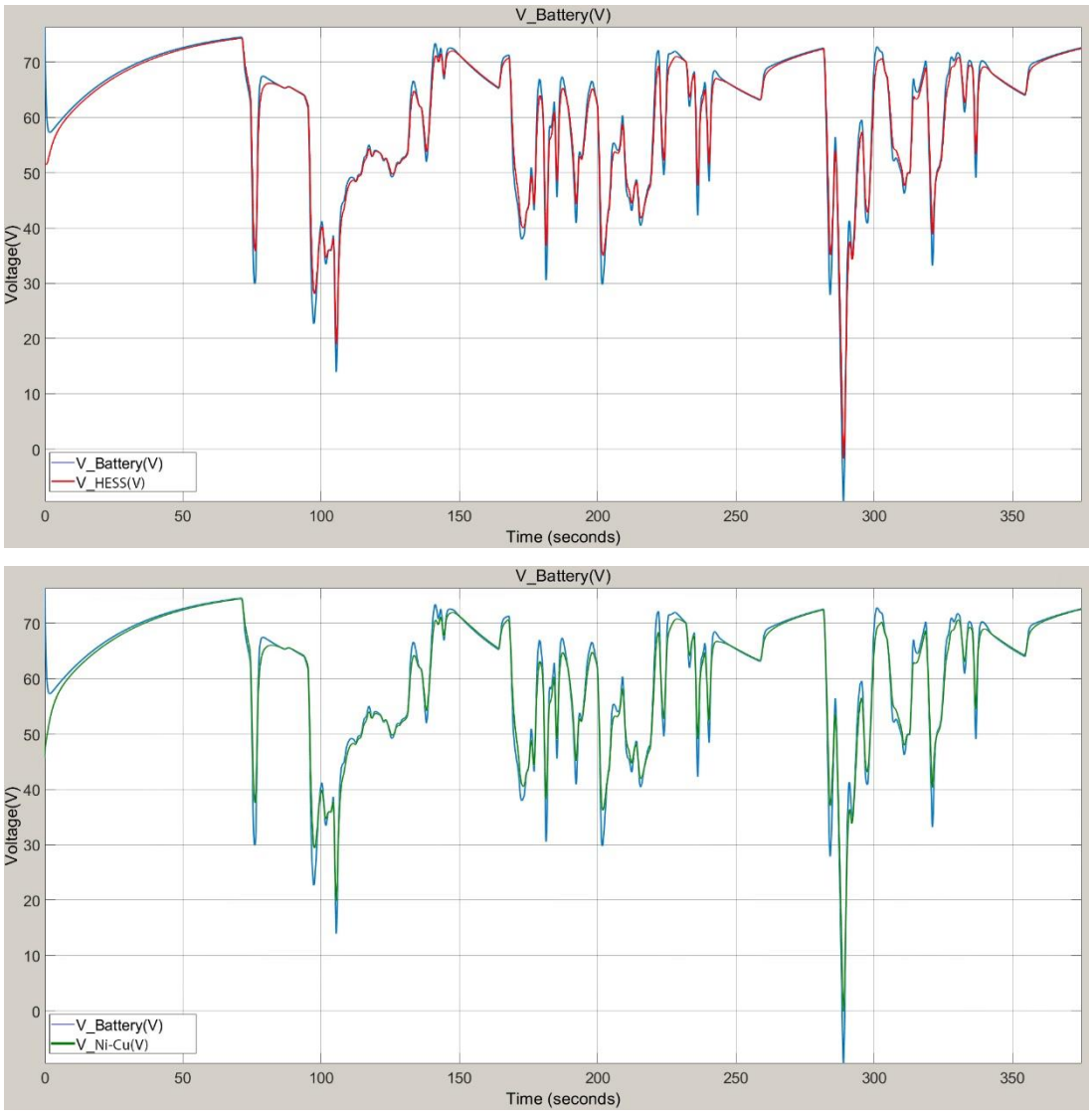

Figure 5.21 – Voltage profiles. Battery vs. Maxwell, b) Battery vs. Ni-Cu

The state of charge of the hybrid configurations (Fig.5.22) displayed for the Maxwell device a battery pack discharge of 0.022% and supercapacitors module SOC oscillating accordingly under 100%, with peaks corresponding to the current's profiles in (Fig.5.20) and maximum discharge of 0.49%. With regards to the Ni-Cu device, its SOC result has shown less charge retention than when compared to the Maxwell device, due to its lower voltage and slightly greater contribution towards the discharge current peak demands, resulting in a maximum discharge of 0.67% and for the battery pack a 0.022% SOC reduction. As for the battery standalone setup, the battery discharge was of about 0.023% (Fig.5.23).

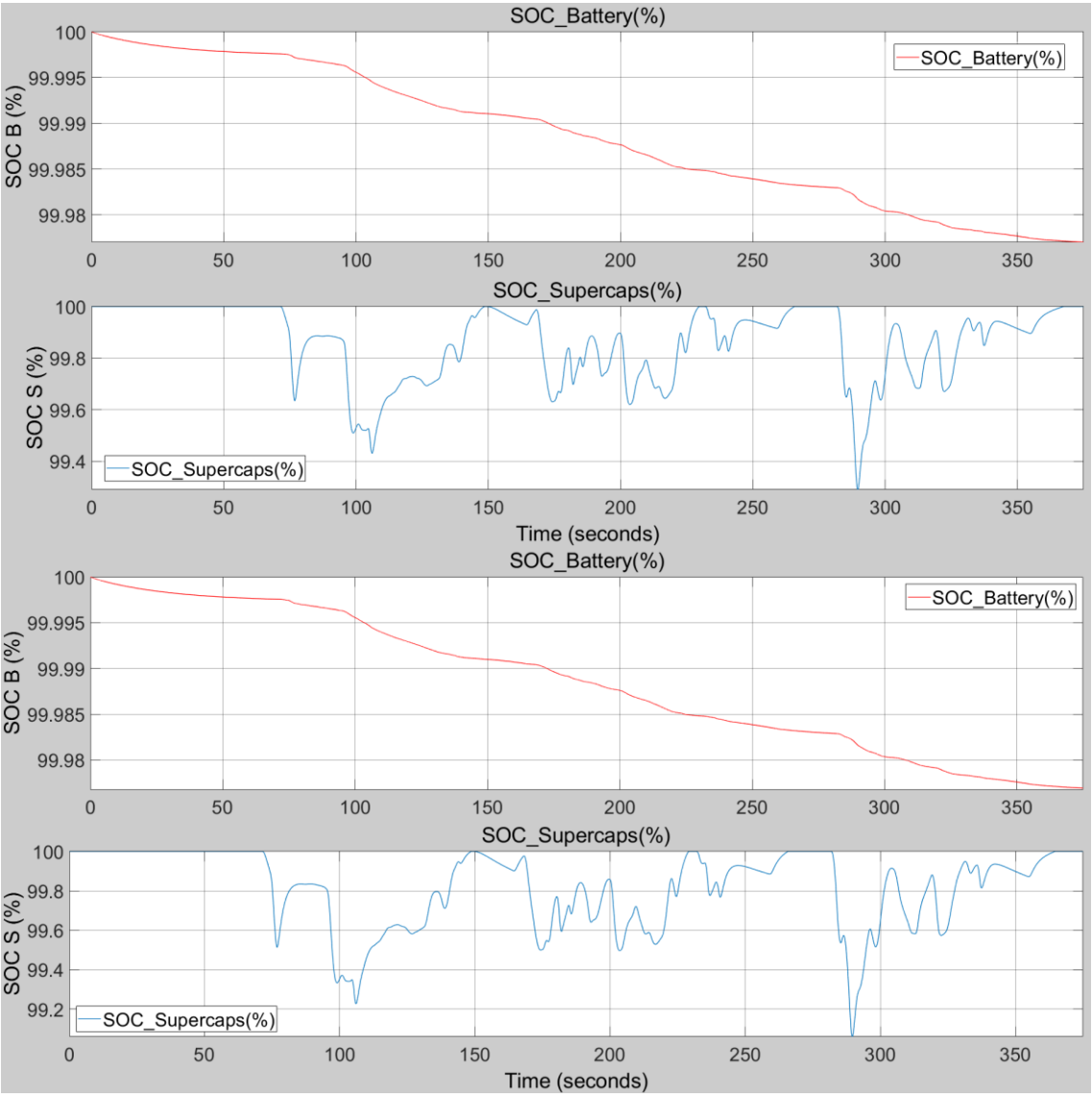

Figure 5.22 – SOC profiles – HESS. a) Maxwell, b) Ni-Cu

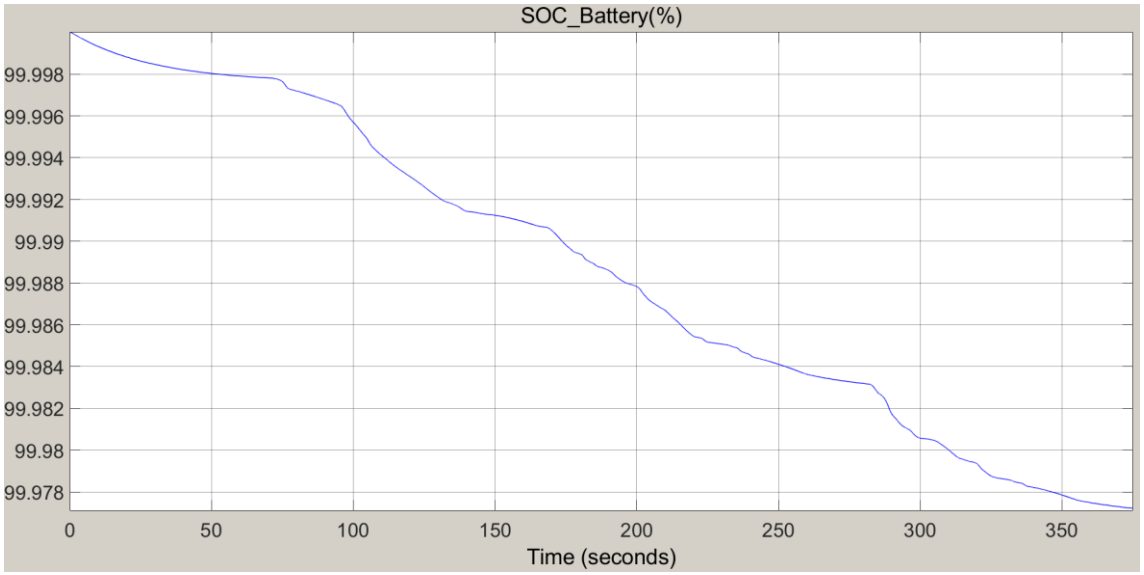

Figure 5.23 – SOC profile – Battery standalone

With regards to the torque, the hybrids and battery standalone configurations displayed a quasi-rectangular profile (Fig.5.24) which behaved according to the implemented speed reference, with maximum and minimum values of 12.5 kN in peak discharging periods and -12.5 kN in peak charging periods.

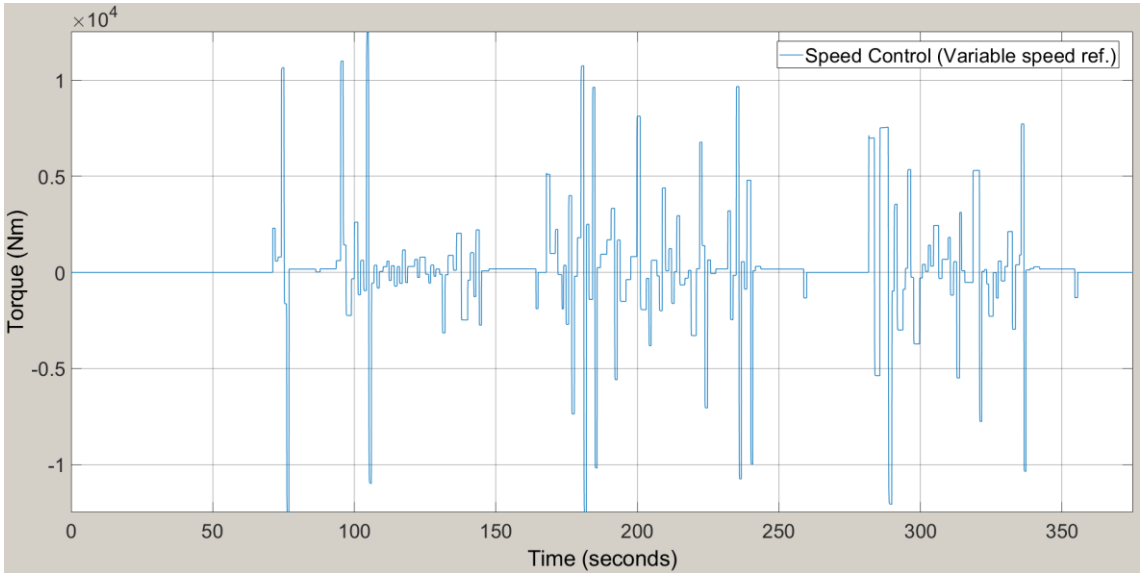

Figure 5.24 – SOC profiles – HESSs and battery standalone

As a vehicle output, in all cases it displayed a maximum velocity of 27.5 km/h with a total linear motion of 400 m (Fig.5.25).

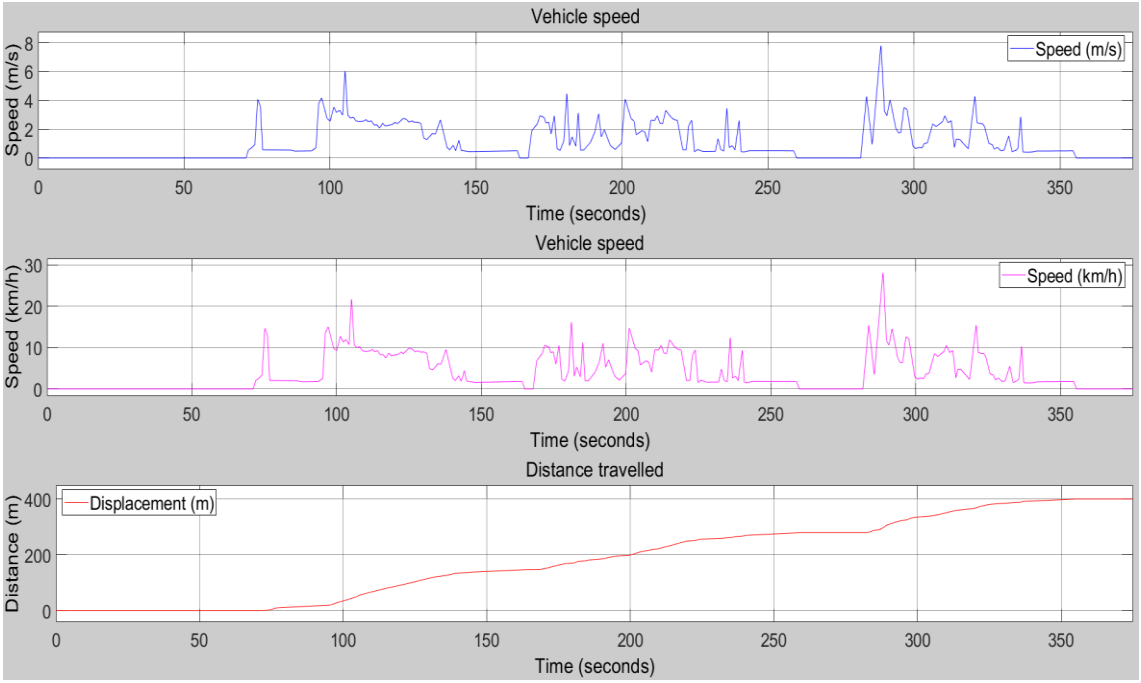

Figure 5.25 – Speed (m/s), speed (km/h), linear motion (m) – HESSs and battery standalone

5.3 Results and Discussion

The simulations performed in this chapter provided enough information to reinforce the initial assumption of battery's lifespan increasing by the direct parallel hybridization with supercapacitors, which was based on [Omar09].

The validation has shown that, despite the reduced base information about the proper load current profile, the profiles generated matched the ones in which the data was based on, therefore demonstrating a reduction in battery current demand in hybrid energy storage configuration when compared to the battery standalone setup, while supplied by the supercapacitors input towards the imposed load current of the system.

With regards to the charge and discharge (cycle) simulation, it made possible to understand how the lifespan extension occurred, as in the load current simulation the proper analysis and comparison was not possible due to a non-completion of full cycles, in which the studied assumption was based on. The decrease in state of charge wave period has postponed the deduction of full cycles from the rated maximum, which determines the lifespan of the device, accounting for its increase in approximately 36 minutes.

When analyzing the obtained results for both Maxwell 2.3V 300F and Ni-Cu hybrid supercapacitor, the modeled Ni-Cu device presented greater contribution to the system with regards to charge and discharge current peaks, therefore absorbing a greater part of the load demand towards the battery, when compared to the Maxwell device. The observed current contribution difference between both devices was, for the charging operations, of +4.3% and +1.46%, while in discharging operation modes +2.15% and +3.8% in the Ni-Cu simulation. The simulations results occurred as expected, as the Ni-Cu device presents greater capacitance and moderate voltage, which was reflected in lower charge and discharge current demands from the battery, therefore increased charge towards the Maxwell 2.3V 300F.

Despite the small proportion of lifespan increasing, it works as a positive indicator of the assumption, which can be further evaluated in laboratorial bench tests, based on real devices so the results can be considered more accurate and consistent.

CHAPTER 6

Conclusion

Here, the dissertation conclusions are presented with regards to the Ni-Cu metallic foam calculation method and its contributions, the modeled Ni-Cu hybrid supercapacitor, the application of hybrid energy storage system to the electric forklift and considerations for future endeavors.

6.1 Conclusions and Contributions

With regards to the increasing electric energy demand from mobile and stationary applications, the development of supercapacitors electrode materials with increasingly higher specific surface area due to its porosity or microstructure, are presented as potential solutions to reach higher energy densities, which contributes to systems energy supply. However, it is still far away from being able to compete with batteries storage capacities as the gap between such technologies is considerably large. Nevertheless, it is important to notice that batteries are known for their lower power densities characteristics which in hybrid configurations with supercapacitors are compensated, hence, supercapacitors with novel electrode materials for higher energy densities would take such hybridization far above known standards either regarding storage capabilities or cost viability.

With regards to the development and modeling of the theoretical nickel-copper metallic foam supercapacitor, the complete procedure has presented a valid and informative way of data extraction and interpretation from a basis device, which supplied information and parameters regarding structural dimensions, energy and power density, materials and design as comparison point. From that, the calculations developed have demonstrated a detailed procedure in order to convert obtained laboratorial tests data from a proposed electrode material into a theoretical supercapacitor cell.

The Ni-Cu hybrid supercapacitor has presented an increased capacitance, of 454F, with regards to the Maxwell 2.3V 300F base example. Regarding the devices forecasted rated voltage, the value of 2V was obtained when a Ni-Cu positive electrode was hybridized with an activated carbon negative electrode. It was noticeable that the voltage obtained was inferior to the Maxwell device, therefore resulting in a slightly reduction in charge but still superior to the base model, 676.16 C and 687.32 C (Table 3.16 and Table 3.17) for the Maxwell 2.3V 300F and Ni-Cu devices, respectively.

In order to digitally model situations where such devices can be implemented, the modeling procedures and equations development presented in this dissertation intend to contribute not just for electrochemical researcher’s but as for professionals from electric engineering community or any other interested personnel.

With regards to the computational model of the hybrid energy storage system comparison addressed in chapter 5, firstly for the implementation of proper parameters into the supercapacitors Simulink block, the data had to be generated, which was made throughout the procedure described in [Zubieta00] and complementary steps such as the digital scaling of the typical procedure voltage waveform and non-linear optimization simulation of the equations mentioned in [Zubieta00] based on the information digitally gathered (chapter 3).

The generated data has shown to be adequate to the scaled waveform making it possible to be implemented in subsequent simulations. Based on [Omar09], which proposed the direct parallel hybridization between batteries and supercapacitors as suitable structure for batteries lifespan increasing, the simulation validation of the very same extracted load current was developed and successfully implemented presenting resulting split battery and supercapacitors currents in line with [Omar09]. From that, the simulation required a better understanding of the interaction between batteries and supercapacitors regarding its effects over the cycle's evolution over time. Therefore, a simulation was developed in order to control charge and discharge cycles based on the applied current and batteries state of charge.

The resulting data has shown the batteries current demand compensation from the supercapacitors towards the total load, resulting in a decrease in cycle completion time of about 2%, which resulted in a 36 minutes lifespan increasing of the battery pack towards a 30h simulation. Such conclusion was based on the understanding that each device has a rated lifespan based on the maximum charge and discharge cycles that it can reach before a compromising defect is most probable to occur.

Therefore, the electric vehicle with hybrid energy storage system simulation (chapter 5) was developed and presented, which structure and dynamics were shown in chapter 4 and based on [Omar09], considering an electric forklift from the Italian manufacturer Carer [Carer17, Omar09]. The chosen energy storage hybridization configuration was a passive topological structure (section 4.7). Thus, the implementation of the typical load current from [Omar09] was made by converting the profile values into power input, then into torque and finally angular velocity, which was implemented in the equivalent point of the

transmission shaft between the electric motor and vehicle front wheels (driven axle). The proposed angular speed profile has matched the scope output values, as well as for the resulting current profile, therefore confirming the accuracy of global simulation implemented data, from vehicle characteristics to energy supply. The reduction in current demand was noticed when comparing the battery standalone setup with both hybrid configurations, which the best results were observed when simulating with Ni-Cu hybrid supercapacitors, as the current contribution difference was, while in charging operations, of +4.3% and +1.46%, which can be interpreted as reduced battery demand when charging the supercapacitors, while in discharging operation modes, +2.15% and +3.8%, demonstrating that the modeled hybrid supercapacitor provided greater current contribution towards the battery. Though, it is important to mention that the inconsistency in cycles completion for the mimicked electric vehicle simulation (sections 5.2 and 5.4), due to the variable load profile, makes it a non-suitable comparison point to observe and understand the lifespan extension, as cycles must be consistently completed, full and continuous charge and discharge events, for the intended analysis. This issue was most certainly solved by the lifespan expansion simulation presented in section 5.3, which results were previously mentioned in this chapter, where full cycles were implemented throughout an SOC controller defining the workable range between 80% and 20%.

The battery lifespan increase by reducing its demand over a certain period, which is supplied by supercapacitors as an additional energy source, presents a valid base knowledge for further studies allowing to analyze different perspectives and gather complementary information, not just related to electric vehicles applications but also to any mobile and stationary intents.

6.2 Future Endeavors and Expectations

Supercapacitors are evolving in an increasing rate as new highly efficient base materials are discovered. There are several public comments that they may replace batteries sometime in the near future even though there is still a long way to go, however it is definitely a possibility what would make electric energy supply and management increasingly fast and high demanded.

With the development of such high energy density supercapacitors, it is possible to predict that smaller but powerful energy storage cells will arise, as well as increasingly high electric vehicles autonomy, what would hopefully reduce the transportation consumption demand for fossil fuels to the lowest limits.

Therefore, the future, near or not, of energy storage system is quite depicted by small energy cells with enormous energy and power densities that, in a way of speaking, can last for a lifetime and run any electric application pollutants-free.

References

[ABB13] ABB – ASEA Brown Boveri, “ABB Demonstrates Technology to Power Flash Charging Electric Bus in 15 Seconds”, May 2013. (https://new.abb.com/news/detail/13930/abb-demonstrates-technology-to-power-flash-charging-electric-bus-in-15-seconds) (accessed in 2019.08.11).

[ABB16] ABB – ASEA Brown Boveri, “ABB’s Innovative Flash-Charging Technology Ushers in a New Era of Sustainable Public Transportation”, July 2016. (https://new.abb.com/news/detail/13896/abb-wins-1st-commercial-order-for-breakthrough-15-second-flash-charging-technology-to-enable-co2-free-public-transport-in-geneva) (accessed in 2019.08.11).

[ABB18] ABB – ASEA Brown Boveri, “ABB’s Innovative Flash-Charging Technology Ushers in a New Era of Sustainable Public Transportation”, January 2018. (https://new.abb.com/news/detail/3318/abbs-innovative-flash-charging-technology-ushers-in-a-new-era-of-sustainable-public-transportation) (accessed in 2019.08.11).

[AE19] American Elements – The Materials Science Manufacturer, “Product Datasheet: Nickel Copper Foam NI-CU-02-FM”, American Elements – The Materials Science Manufacturer, 2019.

[AFC19] AFC – Azerbaijan Film Commission, “Azerbaijan State Photo and Film Archives”. (http://www.afc.az) (accessed in 2019.08.11).

[Allagui16] Allagui, A., Freeborn, T., Elwakil, A. S., Maundy, B. J., “Reevaluation of Performance of Electric Double-layer Capacitors from Constant-current Charge/Discharge and Cyclic Voltammetry”, Scientific Reports, vol. 6, 2016.

[Amador16] Amador, C., Juan, M. de, “Strategies for Structured Particulate Systems Design”, Computer Aided Chemical Engineering, vol. 39, pp. 509-579, 2016.

[AMRE15] AMRE Srl., “Datasheet: DC Traction Motors – 17kW, 80V”, AMRE Srl., 2015.

[Anasori16] Anasori, B., et al., “Control of Electronic Properties of 2D Carbides (Mxenes) by Manipulating their Transition Metal Layers”, Nanoscale Horizons, vol. 1, pp. 227-234, 2016.

[Arubis13] Arubis AG, “Datasheet: CuZn37 Technical Information”, Arubis AG, 2013.

[Arulmani18] Arulmani, S., Anandan, S., Ashokkumar, M., “Chapter 1 - Introduction to Advanced Nanomaterials”, Elsevier, Nanomaterials for Green Energy, pp. 1-53, 2018.

[BAUM13] Baumüller Group, “Datasheet: DC Shunt Wound Motors”, Baumüller Group, 2013.

[BEL19] MicrotracBEL Corp., “Seminar on Adsorption : Specific Surface Area”. (https://www.microtrac-bel.com/en/tech/bel/entry47.html) (accessed in 2019.08.16).

[Béguin13] Béguin, F., Frackoviak, E., “Supercapacitors: Materials, Systems, and Applications”, Wiley-VCH, 2013.

[Bi18] Bi, Z., “Finite Element Analysis Applications: A Systematic and Practical Approach”, Elsevier, Academic Press, 2018.

[Bielenstein80] Bielenstein, H., “The Bureaucracy of Han Times”, Cambridge University Press, 1980.

[Bird07] Bird, J., “Electrical Circuit Theory and Technology”, 3rd ed. Elsevier, Newnes, 2007.

[BMU09] BUM – Federal Minister for the Environment, Nature Conservation, and Nuclear Safety, “National Development Plan for Electric Mobility”, BMU, 2009.

[Bristol16] University of Bristol, “Scientific Breakthrough Reveals Unprecedented Alternative to Battery Power Storage”, December 2016. (http://www.bristol.ac.uk/news/2016/december/super-capacitors.html) (accessed in 2019.08.14).

[Bristol18] University of Bristol, “Alternative to Traditional Batteries Moves a Step Closer After Exciting Progress in Supercapacitor Technology”, February 2018. (http://www.bris.ac.uk/news/2018/february/supercapacitor.html) (accessed in 2019.08.14).

[Cahan93] Cahan, D., “Hermann Von Helmholtz and the Foundations of Nineteenth-century Science California Studies in the History of Science”, 1st ed. University of California Press, Berkeley, 1993.

[Carer17] Carer Srl. - Electric Forklifts, “Datasheet: Electric Forklifts R Series”, Carer Srl. - Electric Forklifts, 2017.

[Carer19] Carer Srl. - Electric Forklifts, “Datasheet: Electric Forklifts R Series”, Carer Srl. - Electric Forklifts, 2019.

[Carignano17] Carignano, M., et al., “Energy management strategy for fuel cell-supercapacitor hybrid vehicles based on prediction of energy demand”, Elsevier, vol. 360, pp. 419-433, 2017.

[Celgard19] Celgard High Performance Battery Separators, “Datasheet: Battery Separators – Monolayer PP 2400”, Celgard High Performance Battery Separators, 2019.

[Chau14] Chau, K. T., “Alternative Fuels and Advanced Vehicle Technologies for Improved Environmental Performance –

Chapter 21: Pure Electric Vehicles", The University of Hong Kong, People's Republic of China, pp. 655.684, 2014.

[Chmiola06] Chmiola, J., et al., "Anomalous Increase in Carbon Capacitance at Pore Sizes Less than 1 Nanometer", Science, vol. 313, pp. 1760-1763, 2006.

[Cole41] Cole, K. S., Cole, R. H., "Dispersion and Absorption in Dielectrics I. Alternating Current Characteristics", The Journal of Chemical Physics, vol. 9, 341 pp., 1941.

[COM16] COM – European Commission, "A European Strategy for Low-Emission Mobility", COM, 2016.

[COM19a] COM – European Commission, "What is Horizon 2020?". (https://ec.europa.eu/programmes/horizon2020/what-horizon-2020) (accessed in 2019.08.12).

[COM19b] COM – European Commission, "EBA – European Battery Alliance". (https://ec.europa.eu/growth/industry/policy/european-battery-alliance_en) (accessed in 2019.08.12).

[Compton12] Compton, R. G., McAuley, C. B., Dickinson, D. J. F., "Voltammetry: Understanding Problems and Solutions", Imperial College Press, 2012.

[Conway03] Conway, B. E., Pell, W. G., "Double-Layer and Pseudocapacitance Types of Electrochemical Capacitors and their Applications to the Development of Hybrid Devices", Journal of Solid State Electrochemistry, vol. 7, pp. 637-644, 2003.

[Conway99] Conway, B. E., "Electrochemical Supercapacitors: Scientific Fundamentals and Technological Applications", Kluwer Academic/Plenum Publishers, 1999.

[Corun19] Corun USA – Corun New Energy Co., "Battery Materials". (http://www.corunusa.com/battery-materials) (accessed in 2019.08.12).

[Curley12] Curley, R., "Fossil Fuels - Energy: Past, Present and Future", 1st ed. Britannica Educational Publishing, 2012.

[Dai15] Dai, Z., Peng, C., Chae, J. H., Chiang, K., Chen, G. Z., "Cell Voltage Versus Electrode Potential Range in Aqueous Supercapacitors", Scientific Reports, vol. 5, 8 pp., 2015.

[Darowicki17] Darowicki, K., Gawel, L., "Impedance Measurement and Selection of Electrochemical Equivalent Circuit of a Working PEM Fuel Cell Cathode", Springer, Electrocatalysis, vol. 8, pp. 235-244, 2017.

[Delta19] Delta Rubber, "Datasheet: DRE80 EPDM Rubber Sheet", Delta Rubber, 2019.

[Díez18] Díez, N., et al., “Highly Packed Graphene–CNT Films as Electrodes for Aqueous Supercapacitors with High Volumetric Performance”, Journal of Materials Chemistry A, vol. 6, pp. 3667-3673, 2018.

[Dong19] Dong, L., et al., “Multivalent Metal Ion Hybrid Capacitors: A Review with a Focus on Zinc-Ion Hybrid Capacitors”, Journal of Materials Chemistry A, vol. 7, pp. 13810-13832, 2019.

[ECB19] ECB – European Central Bank, “ECB Euro Reference Exchange Rate: US dollar (USD)”. (https://www.ecb.europa.eu/stats/policy_and_exchange_rates/euro_reference_exchange_rates/html/eurofxref-graph-usd.en.html) (accessed in 2019.08.13).

[Ehsani05] Ehsani, M., Gao, Y., Gay, S. E., Emadi, A., “Modern Electric, Hybrid Electric, and Fuel Cell Vehicles”, CRC Press LLC, University of West Florida, 395 pp., 2005.

[EIA19] EIA – U.S. Energy Information Administration, “Energy and the Environment Explained: Greenhouse Gasses”. (https://www.eia.gov/energyexplained/energy-and-the-environment/greenhouse-gases.php) (accessed in 2019.09.16).

[Ekpete11] Ekpete, O. A., Horsfall, M. JNR, “Preparation and Characterization of Activated Carbon Derived from Fluted Pumpkin Stem Waste (*Telfairia occidentalis* Hook F)”, Research Journal of Chemical Sciences, vol. 1(3), pp. 10-17, 2011.

[Eland11] Eland, I., “No War for Oil: U.S. Dependency and the Middle East”, The Independent Institute, Oakland - California, 2011.

[Elgrishi18] Elgrishi, N., et al., “A Practical Beginner’s Guide to Cyclic Voltammetry”, Journal of Chemical Education, vol. 95, pp. 197-206, 2018.

[Eliaz19] Eliaz, N., Gileadi, E., “Physical Electrochemistry: Fundamentals, Techniques, and Applications”, Wiley VCH, 2nd. ed., 480 pp., 2019.

[EPRS19] Niestadt M., Bjørnåvold A., “Electric Road Vehicles in the European Union: Trends, Impacts and Policies”, EPRS-European Parliament Research Service, 2019.

[Etheridge96] Etheridge, D. M., Barnola, J. -M., Morgan, V. I., “Natural and Anthropogenic Changes in Atmospheric CO_2 Over the Last 1000 Years from Air in Antarctic Ice and Firn”, Journal of Geophysical Research, vol. 101, nr. D2, pp. 4115-4128, 1996.

[Eugénio13] Eugénio, S., Silva, T. M., Carmezim, M., J., Duarte, R. G., Montemor, M. F., “Electrodeposition and Characterization of Nickel–Copper Metallic Foams for Application as Electrodes

for Supercapacitors", Springer, Journal of Applied Electrochemistry, vol. 44, Issue 4, pp. 455-465, 2013.

[Eurostat19] Eurostat, "Greenhouse Gas Emission Statistics - Emission Inventories", Eurostat Statistics Explained, 2019.

[Faizan17] Faizan, A., et al., "Silicon-Doped Hafnium Oxide Anti-Ferroelectric Thin Films for Energy Storage", Journal of Applied Physics, vol. 122, pp. 144105-1-144105-7 , 2017.

[Feng12] Feng, X., Ding, X., Jiang, D., "Covalent Organic Frameworks", Chemical Society Reviews, vol. 41, pp. 6010-6022, 2012.

[Ferraro19] Ferraro, D., Marcello, G. A., Campisi, M., Pellegrini, V., Polini, M., "Quantum Supercapacitors", Cornell University, 2019.

[Fic12] Fic, K., Frackowiak, E., Béguin, F., "Unusual Energy Enhancement in Carbon-Based Electrochemical Capacitors", Journal of Materials Chemistry, vol. 22, pp. 24213-24223, 2012.

[Fisher13] Fisher, R. A., Watt, M. R., Ready, W. J., "Functionalized Carbon Nanotube Supercapacitor Electrodes: A Review on Pseudocapacitive Materials", ECS Journal of Solid State Science and Technology, vol. 2, pp. 3170-3177, 2013.

[Frackowiak06] Frackowiak, E., Khomenko, V., Jurewicz, K., Lota, K., Béguim, F., "Supercapacitors Based on Conducting Polymers/Nanotubes Composites", Journal of Power Sources, vol. 153, pp. 413-418, 2006.

[Fricke09] Fricke, H., "The Theory of Electrolytic", The London, Edinburgh, and Dublin Philosophical Magazine and Journal of Science, vol. 7, pp. 310-318, 2009.

[Girard15] Girard, H.-L. J.-P., "Modeling and Physical Interpretation of Cyclic Voltammetry for Pseudocapacitors", University of California, Master Thesis, 97 pp., 2015.

[Grbovic13] Grbovic, P. J., "Ultra-Capacitors in Power Conversion Systems: Applications, Analysis, and Design from Theory to Practice", 1st ed. Wiley-IEEE Press, 2013.

[GSMDS15] Global Safety Management Inc., "Safety Datasheet: Manganese Dioxide", Global Safety Management Inc., 2015.

[Gualous11] Gualous, H., Louahlia, H., Gallay, R., "Supercapacitor Characterization and Thermal Modelling with Reversible and Irreversible Heat Effect", IEEE Transactions on Power Electronics, vol. 26, pp. 3402-3409, 2011.

[Hänninen12] Hänninen, V., "Introduction to Computational Chemistry", University of Helsinki, Laboratory of Physical Chemistry, 2012.

[Hao16] Hao, C., et al., "Flexible All-Solid-State Supercapacitors Based on Liquid-Exfoliated Black-Phosphorus Nano Flakes", Advanced Materials, vol. 28, pp. 3194-3201, 2016.

[HEC08] High Energy Corporation, “Ceramic Capacitors”, High Energy Corporation, 2008.

[Herrmann15] Herrmann, M., “Packaging – Materials Review”, AIP Conference Proceedings, vol.1597, 121 pp., 2015.

[Horn18] Horn, M., et al., “Supercapacitors: A new source of power for electric cars?”, Elsevier, Economic Analysis and Policy, vol. 61, pp. 93-103, 2018.

[Horn19] Horn, M., et al., “Graphene-Based Supercapacitor Electrodes: Addressing Challenges in Mechanisms and Materials”, Elsevier, Current Opinion in Green and Sustainable Chemistry, vol. 17, pp. 42-48, 2019.

[Hosseini15] Hosseini, M. G., Zardari, P., “Electrocatalytical Study of Carbon Supported Pt, Ru and Bimetallic Pt-Ru Nanoparticles for Oxygen Reduction Reaction in Alkaline Media”, Applied Surface Science, 2015.

[Huan18] Huan, J., “Diffusion Impedance of Electroactive Materials, Electrolytic Solutions and Porous Electrodes: Warburg Impedance and Beyond”, Elsevier, Electrochimica Acta, vol. 281, pp. 170-188, 2018.

[IEA19a] IEA – International Energy Agency, “Global EV Outlook 2019: Scaling-up the Transition to Electric Mobility”, IEA, 2019.

[IEA19b] IEA – International Energy Agency, “World Energy Investment 2019”, IEA, 2019.

[IC19] Illinois Capacitor, “Datasheet: Supercapacitors”, Illinois Capacitor, 2019.

[Indalco13] Indalco Superior Aliminum Welding Performance, “Datasheet: 1070 Aluminum Alloy”, Indalco Superior Aliminum Welding Performance, 2013.

[IRENA19] IRENA – International Renewable Energy Agency, “Renewable Capacity Statistics 2019”, IRENA, 2019.

[Irwandi16] Irwandi, D., Mas’ud, Z. A., Sutriah, K., Khotib, M., “Preparation and Characterization of Carbon Foam Derived from Fine Coal and Phenolic Resin”, Indonesian Journal of Chemistry, vol. 16(3), pp. 243-248, 2016.

[Jayalakshmi08] Jayalakshmi, M., Balasubramanian, K., “Simple Capacitors to Supercapacitors - An Overview”, International Journal of Electrochemical Science, vol. 3, pp. 1196-1217, 2008.

[Jayaseelan17] Jayaseelan, S. S., et al., “Mesoporous 3D $NiCo_2O_4$/MWCNT Nanocomposite Aerogels Prepared by a Supercritical CO_2 Drying Method for High Performance Hybrid Supercapacitor Electrodes”, Elsevier, Colloids and Surfaces A: Physicochemical and Engineering Aspects (COLSUA 22084), vol. 538, pp. 451-459, 2017.

[Jeong12] Jeong, M.-G., Zhuo, K., Cherevko, S., Chung, C.-H., “Formation of Nanoporous Nickel Oxides for Supercapacitors Prepared by Electrodeposition with Hydrogen Evolution Reaction and Electrochemical Dealloying”, Korean Journal of Chemical Engineering, vol. 29, pp. 1802-1805, 2012.

[Jiang11] Jiang, D., Jin, Z., Wu, J., “Oscillation of Capacitance Inside Nanopores”, American Chemical Society, Nano Letters, vol. 11, pp. 5373-5377, 2011.

[Jocrin06] Jorcin, J. B., Orazem, M. E., Pébère, N., Tribollet, B., “CPE Analysis by Local Electrochemical Impedance Spectroscopy”, Electrochimica Acta, vol. 51, pp. 1473-1479, 2006.

[Jost14] Jost, K., Dion, G., Gogotsi, Y., “Textile Energy Storage in Perspective”, The Royal Society of Chemistry, Journal of Materials Chemistry A, 2014.

[Kakaei18] Kakaei, M. N., Neshati, J., Rezaierod, A. R., “On the Extraction of the Effective Capacitance from Constant Phase Element Parameters”, Protection of Metals and Physical Chemistry of Surfaces, vol. 54, No. 3, pp. 548-556, 2018.

[Kakaei19] Kakaei, K., Esrafili, M. D., Ehsani, A., “Graphene Surfaces: Particles and Catalysts. Chapter 9 - Graphene-Based Electrochemical Supercapacitors”, Elsevier, Interface Science and Technology, vol. 27, pp. 339-386, 2019.

[Kayerematen17] Kayerematen, N. A., Brousse, T., Pech, D., “Microsupercapacitors as miniaturized energy-storage components for on-chip electronics”, Nature Nanotechnology, vol. 12, pp. 7-15, 2017.

[Kim11] Kim, S. H., Choi, W., Lee, K. B., Choi, S., “Advanced Dynamic Simulation of Supercapacitors Considering Parameter Variation and Self-Discharge”, IEEE Transactions on Power Electronics, vol. 26, pp. 3377-3385, 2011.

[Kim17] Kim, B. S., et al., “2D Reentrant Auxetic Structures of Graphene/CNT Networks for Omnidirectionally Stretchable Supercapacitors”, Nanoscale, vol. 9, pp. 13272-13280, 2017.

[Khorasani17] Khorasani, S., Koottandavida, A., “Nonlinear Graphene Quantum Capacitors for Electro-Optics”, Nature Partner Journals, vol. 1, 2017.

[Klein11] Klein, H. A., “The Science of Measurement: A Historical Survey”, Dover Publications, 2011.

[Kroupa16] Kroupa, M., Offer, G. J., Kosek, J., “Modelling of Supercapacitors: Factors Influencing Performance”, Journal of The Electrochemical Society, vol. 163, pp. 2475-2487, 2016.

[Kyerematen16] Kyerematen, N. A., Brousse, T., Pech, D., “Microsupercapacitors as Miniaturized Energy-Storage

Components for On-Chip Electronics", Nature Nanotechnology, vol. 12, pp. 7-15, 2016.

[Largeot08] Largeot, C., et al., "Relation between the Ion Size and Pore Size for an Electric Double-Layer Capacitor", Journal of the American Chemical Society, vol. 130, pp. 2730-2731, 2008.

[Lahyani13] Lahyani, A., Venet, P., Guermazi, A., Troudi, A., "Battery/Supercapacitors Combination in Uninterruptible Power Supply (UPS)", IEEE Transactions on Power Electronics, vol. 28, pp. 1509-1522, 2013.

[Li14] Li, L., et al., "Black Phosphorus Field-Effect Transistors", Nature Nanotechnology, vol. 9, pp. 372-377, 2014.

[Li19] Li, Z., Xu, K., Pan, Y., "Recent Development of Supercapacitor Electrode Based on Carbon Materials", Nanotechnology Reviews, vol. 8, pp. 35-49, 2019.

[Liivand15] Liivand, K., Thomberg, T., Jänes, A., Lust, E., "Separator Materials Influence on Supercapacitors Performance in Viscous Electrolytes", The Electrochemical Society, vol. 20, pp. 41-49, 2015.

[Loba16] Loba Chemie Laboratory Regents & Fine Chemicals, "Datasheet: Aluminium Foil Extra Pure MSDS", Loba Chemie, 2016.

[LS17] LS Ultracapacitors, "LS Ultracapacitors Cells Datasheet", LS Ultracapacitors, 2017.

[Lüthi08] Lüthi, D., "High-resolution Carbon Dioxide Concentration Record", Nature Publishing Group, vol. 453, pp. 379-382, 2008.

[MacDonald84] Macdonald, J. R., "Note on The Parameterization of the Constant-Phase Admittance Element", Solid State Ionics, vol. 13, pp. 147-149, 1984.

[Mahmoudi14] Mahmoudi, C., Flah, A., Sbita, L., "An Overview of Electric Vehicle Concept and Power Management Strategies", International Conference on Electrical Sciences and Technologies, Maghreb (CISTEM), 2014.

[MathWorks18a] MathWorks Student Competitions Team, "Matlab Simulink: Student Competitions - Physical Modeling Training", 2018. (https://www.mathworks.com/matlabcentral/fileexchange/52631-student-competitions-physical-modeling-training) (accessed in 2019.18.10).

[MathWorks19a] The MathWorks, Inc, "Matlab Simulink: Supercapacitor Block", 2019. (https://www.mathworks.com/help/physmod/sps/ref/supercapacitor.html?s_tid=doc_ta) (accessed in 2019.19.10).

[MathWorks19b] The MathWorks, Inc, Matlab Simulink 2018b, “Matlab Simulink 2018b: Supercapacitor Block Parameters Dialog Box – Software Screenshot”, October 2019.

[MathWorks19c] The MathWorks, Inc, Matlab Simulink 2018b, “Matlab Simulink 2018b: Supercapacitor Parameters Identification Example – Software Screenshot”, October 2019.

[Maxwell10] Maxwell Technologies, “Datasheet: 2.7V 650F SUPERCAPACITOR CELL BCAP0650”, Maxwell Technologies, 2010.

[Maxwell18a] Maxwell Technologies, “Datasheet: 2.3V 300F PSEUDOCAPACITOR CELL”, Maxwell Technologies, 2018.

[Maxwell19] Maxwell Technologies, “Company Overview”. (https://www.maxwell.com/about_us/company-overview) (accessed in 2019.08.10).

[May18] May, G. J., Davidson, A., Monahov, B., “Lead batteries for utility energy storage: A review”, Journal of Energy Storage, vol. 15, pp. 145-157, 2018.

[Menictas14] Menictas, C., Skyllas-Kazacos, M., Lim, T. M., “Advances in Batteries for Medium and Large-Scale Energy Storage”, 1st ed. Woodhead Publishing, 2014.

[Merck06] Merck Group, “Safety Datasheet: Potassium Hydroxide Solution for 1000ml”, Merck Group, 2006.

[Merlet12] Merlet, C., et al., “On the Molecular Origin of Supercapacitance in Nanoporous Carbon Electrodes”, Nature Materials, vol. 11, pp. 306-310, 2012.

[Metrohm11] Metrohm Autolab B.V., “Electrochemical Impedance Spectroscopy (EIS) Part 3 – Data Analysis”, Autolab Application Note EIS03, 2011.

[Moseley15] Moseley, P. T., Garche, J., “Electrochemical Energy Storage for Renewable Sources and Grid Balancing”, Elsevier, 2015.

[Murnane17] Murnane, M., Ghazel, A., “A Closer Look at State of Charge (SOC) and State of Health (SOH) Estimation Techniques for Batteries”, Analog Devices, Inc., 2017.

[Muzaffar19] Muzaffar, A., Ahamed, M. B., Deshmukh, K., Thirumalai, J., “A Review on Recent Advances in Hybrid Supercapacitors: Design, Fabrication and Applications”, Elsevier, vol. 101, pp. 123-145, 2019.

[Narayanan15] Narayanan, P. R., Murty, S. V. S. N., “A Review on Recent Advances in Hybrid Supercapacitors: Design, Fabrication and Applications”, Materials Science Forum, vol. 830-831, pp. 655-658, 2015.

[Nasa19] NASA - GLOBAL CLIMATE CHANGE, “Climate change: How do we know?”. (https://climate.nasa.gov/evidence/) (accessed in 2019.08.10).

[NatGeo13] National Geographic, “Supercapacitors Amp Up as an Alternative to Batteries”, August 2013. (https://www.nationalgeographic.com/news/energy/2013/08/130821-supercapacitors/) (accessed in 2019.08.10).

[Niu15] Niu, G., Arribas, A. P., Slameh, M., Krishnamurthy, M., J. M., “Hybrid Energy Storage Systems in Electric Vehicle”, IEEE Transportation Electrification Conference and Expo (ITEC), 6 pp., 2015.

[Obreja10] Obreja, V., Obreja, A. C., Dinescu, A., “Activated Carbon Based Electrodes in Commercial Supercapacitors and their Performance”, International Review of Electrical Engineering, vol. 5, 2010.

[Omar09] Omar, N., et al., “Effectiveness Evaluation of a Supercapacitor-Battery Parallel Combination for Hybrid Heavy Lift Trucks”, 24th International Battery, Hybrid and Fuel Cell Electric Vehicle Symposium and Exhibition, vol. 4, 11 pp., 2009.

[OPEC19] OPEC - Organization of the Petroleum Exporting Countries, “OPEC Share of World Crude Oil Reserves”. (https://www.opec.org/opec_web/en/data_graphs/330.htm) (accessed in 2019.07.10).

[OWiD16] Ritchie, H., Roser, M., “Renewable Energy”, 2019. (https://ourworldindata.org/renewable-energy) (accessed in 2019.07.10).

[Pan98] Pan, J., et al., “Characterization of High-Temperature Oxide Films on Stainless Steels by Electrochemical-Impedance Spectroscopy”, Oxidation of Metals, vol. 50, No. 5/6, 1998.

[Parigi13] Parigi, F., “Fabrication and Modeling of Electrochemical Double-Layer Capacitors Using Carbon Nano-Onion Electrode Structures”, The Graduate College at the University of Nebraska, Doctoral Thesis, 2013.

[Porter12] Porter, D., “Renewable Energy Policy and Incentives”, Elsevier, Association of Electricity Producers, pp. 1-4, 2012.

[POWER16] Power Thru - Phillips Service Industries, Inc., “Lead Acid Battery Working – Lifetime Study”, Power Thru, Phillips Service Industries, Inc., 2016.

[POWERSTREAM19] PowerStream Technology, “Wire Gauge and Current Limits Including Skin Depth and Strength”, PowerStream Technology, 2019.

[Presser12] Presser, V., et al., “The Electrochemical Flow Capacitor: A New Concept for Rapid Energy Storage and Recovery”, Advanced Energy Materials, vol. 2, pp. 895-902, 2012.

[Protec91] Protec - Cursos Técnicos Industriais, “Manual do Desenhista de Máquinas”, Editora F. Provenza, SP, Brasil, 46 ed., 411 pp., 1991.

[Protec96] Protec - Cursos Técnicos Industriais, “Manual do Projetista de Máquinas”, Editora F. Provenza, SP, Brasil, 71 ed., 481 pp., 1996.

[Purkait18] Purkait, T., Singh, G., Kumar, D., Singh, M., Dey, R. S., “High-performance Flexible Supercapacitors Based on Electrochemically Tailored Three-dimensional Reduced Graphene Oxide Networks”, Scientific Reports, vol. 8, 2018.

[Qu14] Qu, D., “Studies of Activated Carbons Used in Double-Layer Capacitors”, AIP Conference Proceedings, vol. 1597, pp. 14-25, 2014.

[Qu98] Qu, D., Shi, H., “Studies of Activated Carbons Used in Double-Layer Capacitors”, Journal of Power Sources, vol. 74, pp. 99-107, 1998.

[Radovic97] Radovic, L. R., “Energy and fuels in society: Analysis of Bills and Media Reports”, 2nd ed. McGraw-Hill Primis Custom Publishing, Boston, 1997.

[Ram17] Ram, M., et. al., “Comparing Electricity Production Costs of Renewables to Fossil and Nuclear Power Plants in G20 Countries”, Greenpeace, 2017.

[Ratha18] Ratha, S., Samantara, A. K., “Supercapacitor: Instrumentation, Measurement and Performance Evaluation Techniques”, Springer, 2018.

[Raza18] Raza, W., et al., “Recent Advancements in Supercapacitor Technology”, Elsevier, Nano Energy, vol. 52, pp. 441-473, 2018.

[Roldán15] Roldán, S., et al., “An Approach to Classification and Capacitance Expressions in Electrochemical Capacitors Technology”, Physical Chemistry Chemical Physics, vol. 17, pp. 1084-1092, 2015.

[Senthilkumar13] Senthilkumar, S. T., Selvan, R. K., Melo, J. S., “Redox Additive/Active Electrolytes: A Novel Approach to Enhance the Performance of Supercapacitors”, Journal of Materials Chemistry A, vol. 1, pp. 12386-12394, 2013.

[SICME02] Sicme Motori Srl., “Catalogue: D.C. Motors for Industrial Applications P-NP Series Frames 80-200”, Sicme Motori Srl., 2002.

[Sing85] Sing, K. S. W., et al., “Reporting Physisorption Data for Gas/Solid Systems with Special Reference to the Determination of Surface Area and Porosity”, International Union of Pure and Applied Chemistry, Physical Chemistry Division, 1985.

[Shabeeba18] Shabeeba, P., Thayyil, M. S., Pillai, M. P., Soufeena, P. P., Niveditha, C. V., “Electrochemical Investigation of Activated Carbon Electrode Supercapacitors”, Russian Journal of Electrochemistry, vol. 54, No. 3, pp. 302-308, 2018.

[Sheng12] Sheng, K., Sun, Y., Li, C., Yuan, W., Shi, G., “Ultrahigh-Rate Supercapacitors Based on Electrochemically Reduced Graphene Oxide for Ac Line-Filtering”, Scientific Reports, vol. 2, 2012.

[Shi14] Shi, F., “Reactor and Process Design in Sustainable Energy Technology”, 1st ed. Elsevier, 2012.

[Sørensen91] Sørensen, B., “A History of Renewable Energy Technology”, Energy Policy, vol. 19, issue 1, pp. 8-12, 1991.

[Stearn24] Stearn, H. O., “Zur Theorie der Elektrolytischen Doppelschicht”, Journal of Electrochemistry and Applied Physical Chemistry, 1924.

[Stearns13] Stearns, P., “The Industrial Revolution in World History”, 4th ed. Westview Press, 2013.

[Stoller10] Stoller, D. M., Ruoff, R. S., “Best Practice Methods for Determining an Electrode Material’s Performance for Ultracapacitors”, Energy and Environmental Science, vol. 3, pp. 1294-1301, 2010.

[Superdielectrics19] Superdielectrics Ltd. (https://www.superdielectrics.com/) (accessed in 2019.08.14).

[Surendar15] Surendar, V., Mohankumar, V., Anand, S., Vadana, D. P., “Estimation of State of Charge of a Lead Acid Battery Using Support Vector Regression”, Elsevier, Smart Grid Technologies, Procedia Technology, vol. 21, pp. 264-270, 2015.

[Svasta17] Svasta, P., Negroiu, R., Vasile, Al., “Supercapacitors - an Alternative Electrical Energy Storage Device”, 5th ed. International Symposium on Electrical and Electronics Engineering (ISEEE), 2017.

[Tabatabaei09] Tabatabaei, S. H., Carreau, P. J., Ajji, A., “Microporous membranes obtained from PP/HDPE multilayer films by stretching”, Elsevier, Journal of Membrane Science, vol. 345, pp. 148.159, 2009.

[Tappan10] Tappan, B. C, Steiner III, S. A., Luther, E. P., “Nanoporous Metal Foams”, Angewandte Chemie, vol. 49, pp. 4544-4565, 2010.

[Thaller76] Thaller, L. H., U.S. Patent 3996, 1976.

[Tesla19a] Tesla Motors, “Tesla Gigafactory”. (https://www.tesla.com/en_GB/gigafactory?redirect=no) (accessed in 2019.08.13).

[Tesla19b] Tesla Motors, “Investors: Tesla Completes Acquisition of Maxwell Technologies”, May 2019. (https://ir.tesla.com/news-releases/news-release-details/tesla-completes-acquisition-maxwell-technologies) (accessed in 2019.08.13).

[Torres17] Torres, P. C, “Relationship Between Constant-Phase Element (CPE) Parameters and Physical Properties of Films With a Distributed Resistivity”, Elsevier, Electrochimica Acta, vol. 225, pp. 592-604, 2017.

[TFP17] The Famous People, “Inventors & Discoverers”. (https://www.thefamouspeople.com/profiles/hermann-von-helmholtz-4828.php) (accessed in 2019.07.09).

[Upadhyay17] Upadhyay, K. K., “Metal Oxides and sulfides based materials active in negative potential window for Supercapacitors”, Universidade de Lisboa, Instituto Superior Técnico, Doctoral Thesis, 2017.

[Venkataraman15] Venkataraman, A., “Pseudocapacitors for Energy Storage”, Portland State University, Master Thesis, 2015.

[Verbrugge05] Verbrugge, M. W., Liu, P., “Microstructural Analysis and Mathematical Modeling of Electric Double-Layer Supercapacitors”, Journal of The Electrochemical Society, vol. 152, pp. 79-87, 2005.

[Vicentini19] Vicentini, R., et al., “How to Measure and Calculate Equivalent Series Resistance of Electric Double-Layer Capacitors”, MDPI, Molecules, vol. 24, pp. 1452, 2019.

[Vishay17] Vishay Draloric, “Datasheet: Power Barrel Capacitors”, Vishay Draloric, 2017.

[Viswanathan17] Viswanathan, B., “Fundamentals of Chemical Conversion Processes and Applications: Chapter 13 - Supercapacitors”, Elsevier, Energy Sources, pp. 315-328, 2017.

[Wang17] Wang, F., et al., “Latest Advances in Supercapacitors: From New Electrode Materials to Novel Device Designs”, Chemical Society Reviews, vol. 46, pp. 6816-6854, 2017.

[Westerhoff16] Westerhoff, U., Kurbach, K., Lienesch, F., Kurrat, M., “Analysis of Lithium-Ion Battery Models Based on Electrochemical Impedance Spectroscopy”, Wiley Online Library, Energy Technology, vol. 4, pp. 1620-1630, 2016.

[Yaghi05] Yaghi, O. M., “Porous, Crystalline, Covalent Organic Frameworks”, Science, vol. 310, pp. 1166-1170, 2005.

[Yassine17] Yassine, M., Fabris, D., “Performance of Commercially Available Supercapacitors”, MDPI, Energies, vol. 10, 1340 12 pp., 2017.

[Ye18] Ye, B., et al., “A High-performance Asymmetric Supercapacitor Based on Ni3S2-Coated NiSe Arrays as Positive Electrode”, New Journal of Chemistry, vol. 43, pp. 2389-2399, 2018.

[Yoon16] Yoon, Y., Lee, K., Lee, H., “Low-dimensional Carbon and Mxene-Based Electrochemical Capacitor Electrodes”, IOP Publishing, Nanotechnology, vol. 27, 172001 21pp., 2016.

[Xia15] Xia, W., Mahmood, A., Zou, R., Xu, Q., “Metal–Organic Frameworks and their Derived Nanostructures for Electrochemical Energy Storage and Conversion”, Energy & Environmental Science, vol. 8, pp. 1837-1866, 2015.

[Xu12] Xu, R., Berduque, A., “Rubber Sealing Materials for high Voltage and High Temperature Aluminum Electrolytic Capacitors”, ECA – Electronics Components Assemblies & Materials Association, pp. 221-236, 2012.

[Zhang16] Zhang, Q., et al., “A Rule Based Energy Management System of Experimental Battery/Supercapacitor Hybrid Energy Storage System for Electric Vehicles”, Hindawi Publishing Corporation, Journal of Control Science and Engineering, vol. 2016, 17 pp., 2016.

[Zhu06] Zhu, C., Lu, R., Tian, L., Wang, Q., “The Development of an Electric Bus with Super-Capacitors as Unique Energy Storage”, IEEE Vehicle Power and Propulsion Conference, Windsor, 2006, pp. 1-5, 2006.

[Zubieta00] Zubieta, L., Bonert, R., “Characterization of Double-Layer Capacitors for Power Electronics Applications”, IEEE Transactions on Industry Applications, vol. 36, No. 1, pp. 199-205, 2000.

Annexes

Annex 1 – Electrodeposited Ni-Cu Metallic Foam

1 Ni-Cu Metallic Foam

In [Eugénio13], the Ni-Cu metallic foams were electrodeposited at different deposition times and current densities as mentioned hereinafter.

The deposition times applied to the samples were defined in a range of 30 to 180 s, which morphologies presents different aspects as it increases. In the results it is noticeable that for higher deposition times the morphology changes forming a three-dimensional foam-type film, showing randomly distribute pores and its dendrites assume a fern-like structure with secondary and tertiary branching which maintains a non-compact pore wall.

The applied current densities ranged between 0.6 to 1.8 A cm^{-2} [Eugénio13] and, as the same as for time, the increase in current resulted in better results, with films presenting a foam-like morphology, randomly distributed nearly-circular pores and inner pore walls with open dendrite structure. Besides that, with the increase in current, dendrites become larger and more ramified.

As previously mentioned, both the deposition time and current density when incremented presented better structural results, therefore, increase in porosity. At 1.8 A cm^{-2}, the pores presented the best surface pore area result of 225 μm^2 for 180 s, from which it was determined, when taking the area in relation to the pores nearly circular geometry, 17 μm as respective diameter. These data alone are not enough to estimate the material's porosity once they require a greater amount of data, which will be covered in chapter 5, section 5.6.1.

The maximum value for specific capacitance, of 105 F g^{-1} at 1 $mAcm^{-2}$, was obtained from a sample with deposition current density and time of 1.8 Acm^{-2} and 180 s, respectively. As for cyclic stability the sample presented a capacitance retention of 90 % after 10 thousand cycles.

1.2 Cyclic Voltammetry - CV

Cyclic voltammograms of 1 M KOH solution on Ni–Cu foams a) deposited during 90 s at different current densities (scan rate100 mV s^{-1}), b) deposited at 1.8 A cm^{-2} with different deposition times (scan rate 100 mV s^{-1}), c) deposited at 1.8 A cm^{-2} for 90 s with increasing scan

rates and d the variation of the cathodic peak current with the square root of the scan rate

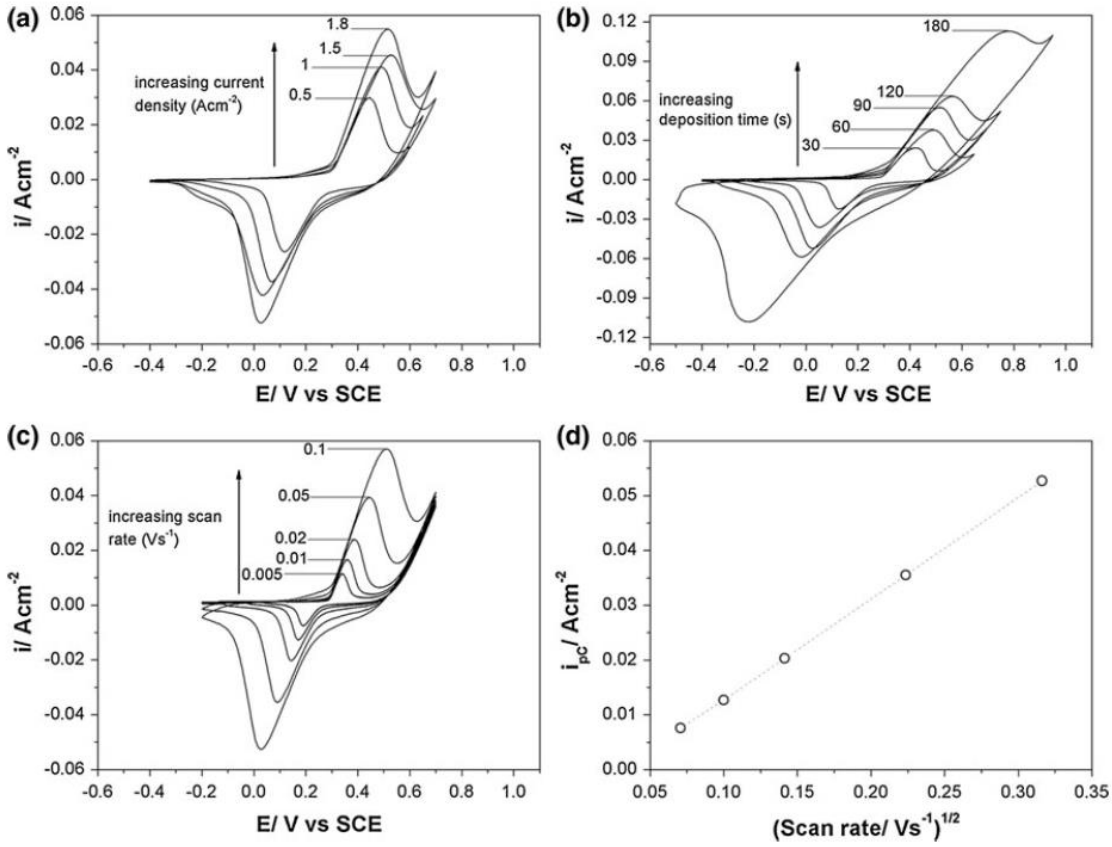

1.3 Galvanostatic Charge and Discharge - GCD

Galvanostatic charge–discharge curves of Ni–Cu foams: a) effect of deposition time and b) effect of applied charge–discharge current; c) variation of specific capacitance with applied charge– discharge current and the deposition time and d cycling stability of Ni–Cu foams

deposited at 1.8 A cm^{-2} during 180 s at 10 mA cm^{-2}

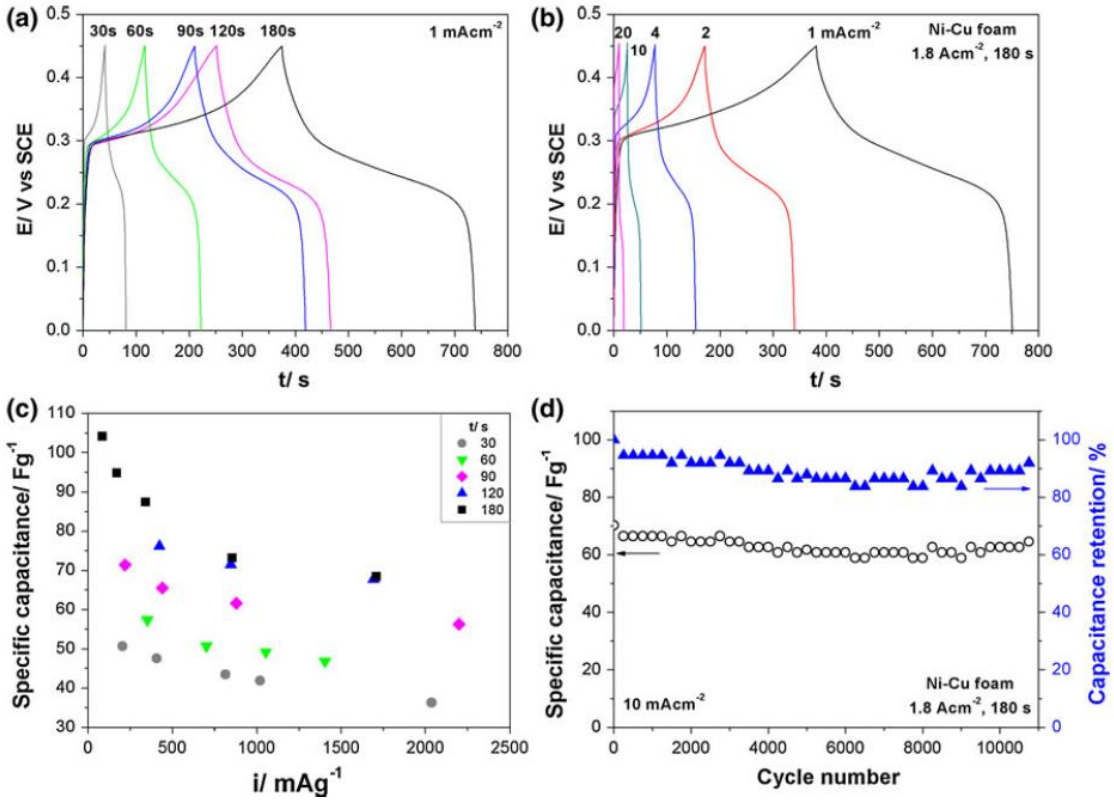

Annex 2 – Supercapacitors Parameter Identification Procedure [Zubieta00]

A. Immediate Branch Parameter Identification

Event $n = 0$:

Before identification $V_0 = 0$ V.
$Q_0 = 0$.
Current source is switched on $(I = I_{ch})$.

Event $n = 1$:

$t_1 = 20$ ms.
t_1 is given by the experimental fact that the current rises to the set value I_{ch} in less than 20 ms.
Measure V_1.
After the small time t_1, the DLC terminal voltage is mainly determined by the voltage drop at R_i.
Parameter:

$$Ri = \frac{V_1}{I_{ch}}.$$

Event $n = 2$:

Reached when $V_2 = V_1 + \Delta V$.
ΔV is chosen to be 50 mV.
Measure t_2, $t = t_2 - t_1$.
As Vci is approximately zero, the differential capacitance as defined in (3) is equal to $Ci0$.
Parameter:

$$Ci0 = I_{ch} * \frac{\Delta t}{\Delta V}.$$

Event $n = 3$:

Reached when $V_3 =$ Vrated.
Measure t_3.
The current source is turned off $(I_{ch} = 0)$.

Event $n = 4$:

$t_4 = t_3 + 20$ ms.
20 ms is given by fall time of the current.
Measure V_4.
Total charge supplied to the DLC: $Q_{\text{tot}} = I_{ch} * (t_4 - t_1)$.
From $Q_{\text{tot}} = C_q * V_4$, we can find C_q, and then using (6) the voltage-dependent capacitance may be calculated.
Parameter:

$$Ci1 = \frac{2}{V_4} * \left(\frac{I_{ch} * (t_4 - t_1)}{V_4} - Ci0 \right).$$

B. Delayed Branch Parameter Identification

Event $n = 5$:

Reached when $V_5 = V_4 - \Delta V$.
ΔV is chosen to be 50 mV.
Measure t_5, $\Delta t = t_5 - t_4$.
As ΔV is small and Cd is assumed discharged, I_{tr} is virtually constant and given by: $I_{tr} = (V_4 - \Delta V/2)/Rd$. ($Ri$ neglected because $Ri \ll Rd$).
Relating the transfer current I_{tr} with the change in charge at the immediate branch, we get: $I_{tr} = C_{\text{diff}} * \Delta V/\Delta t$.
C_{diff} is calculated at the voltage $Vci = V_4 - \Delta V/2$ using (3).
Parameter:

$$Rd = \frac{(V_4 - \Delta V/2) * \Delta t}{C_{\text{diff}} * (\Delta V)}.$$

Event $n = 6$:

$t_6 = t_5 + 3(Rd * Cd)$.
Typically $Rd * Cd \approx 100$ s.
Measure V_6.
As $t_6 - t_5$ is three times the second branch time constant, the charge redistribution from the immediate to the delayed branch has ended at t_6 and $Vci = Vd$.
The delayed branch capacitance is calculated using the charge balance: $Q_{\text{tot}} = Cd * V_6 + V_6\ (Cio + Ci1 * V_6/2)$.
Parameter:

$$Cd = \frac{Q_{\text{tot}}}{V_6} - \left(Cio + \frac{Ci1}{2} * V_6\right).$$

C. *Long-Term Branch Parameters Identification*

Event $n = 7$:

Reached when $V_7 = V_6 - \Delta V$.
ΔV is chosen to be 50 mV.
Measure t_7, $\Delta t = t_7 - t_6$.
As ΔV is small and Cl is assumed discharged, I_{tr} is virtually constant and given by: $I_{tr} = (V_6 - \Delta V/2)/Rl$. ($Ri$ and Rd neglected because $Ri \ll Rd \ll Rl$).
Because Rd is much larger than Ri, the transfer current I_{tr} at this initial instant is supplied mainly from the immediate branch: $I_{tr} = C_{\text{diff}} * \Delta V/\Delta t$.
Parameter:

$$Rl = \frac{(V_6 - \Delta V/2) * \Delta t}{C_{\text{diff}} * (\Delta V)}.$$

Event $n = 8$:

$t_8 = 30$ min.

At t_8 it is assumed that the charge redistribution to the long-term branch has ended and the three equivalent capacitors have the same voltage.

Measure V_8.

The long-term capacitance is calculated using the charge balance: $Q_{\text{tot}} = Cl * V_8 + Cd * V_8 + V_8(Cio + Ci1 * V_8/2)$.
Parameter:

$$Cl = \frac{Q_{\text{tot}}}{V_8} - \left(Cio + \frac{Ci1}{2} * V_8\right) = Cd.$$

Annex 3 – Load Current to Angular Speed Conversion

t	I	V	R	P(W)	P(kW)	P(%) rated	ω (rad s^{-1})	speed(km/h)
72.06	33.0846	60.9423	1.842014	2016.252	2.016252	12%	1.349188	2.039972226
73.04	32.4886	76.2705	2.347608	2477.922	2.477922	15%	1.658118	2.507073787
74.23	43.8152	75.7324	1.72845	3318.23	3.31823	20%	2.220416	3.357268255
75.14	219.8205	66.7145	0.303495	14665.21	14.66521	86%	9.813325	14.83774669
76.12	190.6102	66.47	0.348722	12669.86	12.66986	75%	8.47812	12.81891717
76.89	31.1475	65.1907	2.092967	2030.527	2.030527	12%	1.358741	2.054415885
86.42	29.5079	66.3559	2.24875	1958.023	1.958023	12%	1.310224	1.981058829
87.89	25.1861	67.5	2.68005	1700.062	1.700062	10%	1.137607	1.720062476
93.63	24.5901	71.51	2.908081	1758.438	1.758438	10%	1.17667	1.779125557
95.17	34.8733	72.04	2.065764	2512.273	2.512273	15%	1.681104	2.541828679
96.01	185.5432	72.23	0.389289	13401.79	13.40179	79%	8.967892	13.5594534
97.06	205.2154	72.46	0.353092	14869.91	14.86991	87%	9.950296	15.04484798
98.95	133.8297	72.8061	0.54402	9743.619	9.743619	57%	6.520006	9.858249327
100.00	125.335	72.9166	0.581774	9139.002	9.139002	54%	6.115423	9.246519732
101.26	172.7266	73.0492	0.422918	12617.54	12.61754	74%	8.44311	12.7659816
102.17	153.6506	73.1449	0.476047	11238.76	11.23876	66%	7.520488	11.37097845
103.29	160.9531	73.3122	0.455488	11799.83	11.79983	69%	7.895931	11.93864734
104.27	144.262	73.1971	0.50739	10559.56	10.55956	62%	7.065999	10.68379016
104.97	321.0121	73.079	0.227652	23459.24	23.45924	138%	15.69791	23.73523435
106.02	157.9724	67.2165	0.425495	10618.35	10.61835	62%	7.10534	10.74327361
106.93	147.3913	66.96	0.454301	9869.321	9.869321	58%	6.604121	9.985431112
107.98	153.2036	65.89	0.430081	10094.59	10.09459	59%	6.754858	10.21334503
108.82	139.791	65.5	0.468557	9156.311	9.156311	54%	6.127005	9.2640318
110.15	137.5556	65.137	0.473532	8959.959	8.959959	53%	5.995615	9.065370401
111.49	143.6658	63.57	0.442485	9132.835	9.132835	54%	6.111296	9.240280023
112.26	150.968	62.8419	0.41626	9487.116	9.487116	56%	6.348366	9.598729088
113.03	142.7716	62.79	0.439793	8964.629	8.964629	53%	5.99874	9.070094985
114.08	146.3482	62.6269	0.427931	9165.334	9.165334	54%	6.133043	9.273161546
115.13	136.9594	59.26	0.432683	8116.214	8.116214	48%	5.431018	8.211698915
115.97	138.3008	59.55	0.430583	8235.813	8.235813	48%	5.511048	8.332704553
116.95	123.6956	59.9	0.484253	7409.366	7.409366	44%	4.958026	7.496535457
118.00	142.4735	60.26	0.422956	8585.453	8.585453	51%	5.745012	8.686458441
118.84	130.7002	60.55	0.463274	7913.897	7.913897	47%	5.295636	8.007001782
121.29	135.3201	61.1569	0.451942	8275.758	8.275758	49%	5.537778	8.37311968
122.27	143.9638	61.3002	0.425803	8825.01	8.82501	52%	5.905313	8.928833377
123.04	137.5556	61.36	0.446074	8440.412	8.440412	50%	5.647957	8.539710576
125.07	159.4628	61.64	0.386548	9829.287	9.829287	58%	6.577332	9.944925662
126.26	152.7564	61.96	0.405613	9464.787	9.464787	56%	6.333424	9.576136974
126.96	142.9206	62.1787	0.435058	8886.617	8.886617	52%	5.946538	8.991165548
128.08	146.9442	62.18	0.423154	9136.99	9.13699	54%	6.114077	9.24448436

128.78	141.5795	62.3937	0.440697	8833.669	8.833669	52%	5.911107	8.937594365
130.11	141.4303	62.45	0.44156	8832.322	8.832322	52%	5.910206	8.936231908
131.09	136.3633	62.5015	0.458345	8522.911	8.522911	50%	5.703162	8.623180334
132.07	78.5394	62.2504	0.792601	4889.109	4.889109	29%	3.271579	4.946627996
133.12	72.7272	62.38	0.857726	4536.723	4.536723	27%	3.035778	4.590095945
134.94	96.7211	61.97	0.640708	5993.807	5.993807	35%	4.010795	6.064321938
136.07	95.8269	61.7126	0.644001	5913.727	5.913727	35%	3.957209	5.98330041
137.75	153.3526	61.6588	0.402072	9455.537	9.455537	56%	6.327235	9.566778908
140.06	42.1757	61.87	1.466958	2609.411	2.609411	15%	1.746104	2.640109507
140.97	32.4886	62.02	1.908977	2014.943	2.014943	12%	1.348312	2.038648183
142.16	49.7765	63.34	1.272488	3152.844	3.152844	19%	2.109746	3.189935787
143.00	28.0176	64.34	2.296414	1802.652	1.802652	11%	1.206257	1.823860059
144.12	67.5111	65.0292	0.963237	4390.193	4.390193	26%	2.937726	4.441842151
144.89	28.7628	65.21	2.267165	1875.622	1.875622	11%	1.255085	1.897688331
147.55	24.4409	64.6168	2.643798	1579.293	1.579293	9%	1.056794	1.597872662
164.15	24.4409	72.8157	2.979256	1779.681	1.779681	10%	1.190885	1.800618669
164.92	0	72.8157	0	0	0	0%	0	0
167.86	0	72.9598	0	0	0	0%	0	0
169.05	91.9522	73.0181	0.794088	6714.175	6.714175	39%	4.492834	6.793165228
171.01	116.3932	73.1136	0.62816	8509.926	8.509926	50%	5.694473	8.610042642
171.85	143.0696	73.1553	0.511327	10466.3	10.4663	62%	7.003593	10.58943244
173.32	136.2143	73.2273	0.537589	9974.605	9.974605	59%	6.674573	10.09195371
173.88	118.3306	73.2406	0.618949	8666.604	8.666604	51%	5.799315	8.768564191
174.79	120.2679	73.71	0.612882	8864.947	8.864947	52%	5.932037	8.969240402
175.70	80.0297	74.07	0.925531	5927.8	5.9278	35%	3.966626	5.997538701
176.75	141.2813	74.3161	0.526015	10499.48	10.49948	62%	7.025793	10.62299846
177.73	31.2963	74.5494	2.382052	2333.12	2.33312	14%	1.561223	2.360568862
178.78	25.7824	73.1	2.835267	1884.693	1.884693	11%	1.261155	1.906866304
180.04	59.0164	71.38	1.209494	4212.591	4.212591	25%	2.818883	4.262150522
181.02	236.5118	70.03	0.296095	16562.92	16.56292	97%	11.08319	16.75777925
182.00	43.9642	68.69	1.562408	3019.901	3.019901	18%	2.020786	3.055429144
182.84	77.6452	67.52	0.869597	5242.604	5.242604	31%	3.508123	5.304281597
184.17	43.2191	66.66	1.542374	2880.985	2.880985	17%	1.92783	2.91487915
184.95	172.5776	66.3738	0.384603	11454.63	11.45463	67%	7.664941	11.58939147
185.79	28.7628	66.56	2.3141	1914.452	1.914452	11%	1.281068	1.936974932
186.98	30.7003	65.7285	2.140973	2017.885	2.017885	12%	1.350281	2.041624488
189.22	57.675	68.4	1.185956	3944.97	3.94497	23%	2.639803	3.991381412
190.69	98.3604	65.86	0.669578	6478.016	6.478016	38%	4.334807	6.554227896
191.95	167.8085	65.5494	0.39062	10999.75	10.99975	65%	7.360552	11.12915527
192.86	77.347	66.9836	0.866014	5180.981	5.180981	30%	3.466887	5.241933221
193.91	102.8314	67.74	0.658748	6965.799	6.965799	41%	4.66121	7.047749613
195.94	46.3488	67.61	1.458722	3133.642	3.133642	18%	2.096897	3.170508749
197.62	30.4023	68.96	2.268249	2096.543	2.096543	12%	1.402915	2.121207815

199.79	53.3532	68.99	1.293081	3680.837	3.680837	22%	2.463056	3.724141236
200.98	214.9025	68.3282	0.31795	14683.9	14.6839	86%	9.825829	14.85665278
203.08	145.1377	66.81	0.460321	9696.65	9.69665	57%	6.488577	9.810727969
204.06	137.4064	66.6608	0.485136	9159.621	9.159621	54%	6.12922	9.267380791
204.83	85.2458	67.21	0.788426	5729.37	5.72937	34%	3.833846	5.796774574
206.86	98.2114	68.83	0.700835	6759.891	6.759891	40%	4.523425	6.839418787
207.77	92.3992	69.135	0.748221	6388.019	6.388019	38%	4.274585	6.463171853
208.75	57.377	69.7624	1.21586	4002.757	4.002757	24%	2.678471	4.049848486
209.88	134.2769	69.9956	0.521278	9398.792	9.398792	55%	6.289263	9.509366207
211.07	138.3008	67.05	0.484813	9273.069	9.273069	55%	6.205135	9.382163565
212.05	160.506	65.09	0.40553	10447.34	10.44734	61%	6.990903	10.57024537
212.96	133.5317	64.51	0.483106	8614.13	8.61413	51%	5.764202	8.715472672
213.87	131.8924	64.1865	0.486658	8465.712	8.465712	50%	5.664886	8.565308139
214.92	181.5193	64.84	0.357207	11769.71	11.76971	69%	7.87578	11.90817861
216.74	153.7996	65.49	0.425814	10072.34	10.07234	59%	6.739969	10.19083387
217.93	143.5168	65.6927	0.457735	9428.006	9.428006	55%	6.308812	9.538923806
218.91	140.3871	66.5712	0.474197	9345.738	9.345738	55%	6.253762	9.455687567
220.80	31.1475	65.36	2.098403	2035.801	2.035801	12%	1.362269	2.059751195
221.99	32.0415	64.1148	2.000992	2054.334	2.054334	12%	1.374671	2.078503004
222.76	124.2918	63.7204	0.512668	7919.923	7.919923	47%	5.299669	8.01309878
223.81	146.9442	63.72	0.433634	9363.284	9.363284	55%	6.265503	9.473440711
224.79	24.4409	62.73	2.566599	1533.178	1.533178	9%	1.025936	1.551215041
225.84	33.681	62.22	1.847332	2095.632	2.095632	12%	1.402306	2.120286312
227.66	26.2292	61.9637	2.362394	1625.258	1.625258	10%	1.087552	1.644378966
231.93	24.8881	66.6608	2.678421	1659.061	1.659061	10%	1.110171	1.678579017
232.84	72.5782	66.03	0.909777	4792.339	4.792339	28%	3.206825	4.848718999
233.75	32.3398	65.2445	2.017468	2109.994	2.109994	12%	1.411916	2.134817541
234.88	25.4841	66.7	2.617318	1699.789	1.699789	10%	1.137425	1.719786993
235.86	185.6922	68.1242	0.366866	12650.13	12.65013	74%	8.464919	12.79895766
236.70	37.7048	68.9	1.827354	2597.861	2.597861	15%	1.738376	2.628423787
237.75	43.6661	69.82	1.598952	3048.767	3.048767	18%	2.040102	3.08463495
238.66	28.1668	70.4259	2.500316	1983.672	1.983672	12%	1.327387	2.007009561
240.06	132.0414	71.0441	0.538044	9380.762	9.380762	55%	6.277199	9.491124337
240.76	22.2054	71.3112	3.211435	1583.494	1.583494	9%	1.059605	1.602123058
241.67	20.8642	71.66	3.434591	1495.129	1.495129	9%	1.000475	1.51271832
243.56	25.0372	71.34	2.84936	1786.154	1.786154	11%	1.195217	1.807167423
258.76	24.4409	72.65	2.972476	1775.631	1.775631	10%	1.188175	1.796521166
259.81	0	72.7195	0	0	0	0%	0	0
281.72	0	75.2501	0	0	0	0%	0	0
283.69	204.7684	75.3208	0.367834	15423.32	15.42332	91%	10.32062	15.60477052
285.65	44.2622	75.3919	1.703302	3337.011	3.337011	20%	2.232983	3.376270313
288.59	375.8554	75.4979	0.20087	28376.29	28.37629	167%	18.98818	28.71013215
289.85	152.4584	75.5433	0.495501	11517.21	11.51721	68%	7.706817	11.65270724

290.69	138.1516	75.5736	0.547034	10440.61	10.44061	61%	6.986405	10.56344451
291.74	191.2064	75.61	0.395437	14457.12	14.45712	85%	9.674074	14.62719962
293.77	100.5959	72.11	0.716828	7253.97	7.25397	43%	4.854042	7.339311177
294.61	90.4618	69.1709	0.764642	6257.324	6.257324	37%	4.187129	6.3309397
295.45	90.4618	69.52	0.768501	6288.904	6.288904	37%	4.208262	6.362891446
296.50	183.6058	68.2	0.371448	12521.92	12.52192	74%	8.379122	12.66923221
297.55	189.5671	63.25	0.333655	11990.12	11.99012	71%	8.023267	12.1311793
299.65	48.2861	59.23	1.226647	2859.986	2.859986	17%	1.913778	2.893632594
300.63	39.4932	59.4357	1.50496	2347.306	2.347306	14%	1.570715	2.374921352
301.68	44.4112	59.3461	1.336287	2635.632	2.635632	16%	1.76365	2.666638946
302.73	41.7287	59.7223	1.431204	2492.134	2.492134	15%	1.667628	2.521453163
303.50	59.1654	60.36	1.020191	3571.224	3.571224	21%	2.389708	3.613237939
304.55	60.9537	61.5	1.008963	3748.653	3.748653	22%	2.508435	3.792754345
306.37	135.0221	62.43	0.462369	8429.43	8.42943	50%	5.640608	8.528599464
307.56	127.1233	61.1031	0.48066	7767.628	7.767628	46%	5.197759	7.859011568
309.74	141.5795	63.55	0.448864	8997.377	8.997377	53%	6.020654	9.103228722
310.51	161.5493	64.56	0.39963	10429.62	10.42962	61%	6.97905	10.55232425
311.63	131.8924	66.06	0.500863	8712.812	8.712812	51%	5.830235	8.815315614
312.75	136.5124	67.3422	0.493305	9193.045	9.193045	54%	6.151587	9.301198818
313.80	38.152	67.84	1.778151	2588.232	2.588232	15%	1.731932	2.618681464
314.43	68.8523	68.2386	0.991087	4698.385	4.698385	28%	3.143955	4.753659671
315.62	67.5111	67.86	1.005168	4581.303	4.581303	27%	3.065609	4.635200931
318.56	34.575	65.61	1.897614	2268.466	2.268466	13%	1.517959	2.295153582
320.80	241.5789	63.8461	0.264287	15423.87	15.42387	91%	10.32098	15.60532791
321.57	136.0653	63.72	0.468305	8670.081	8.670081	51%	5.801641	8.772081868
322.55	134.2769	63.5233	0.473077	8529.712	8.529712	50%	5.707713	8.630061352
323.32	131.1472	64.85	0.494483	8504.896	8.504896	50%	5.691107	8.604953519
324.09	123.5466	63.31	0.512438	7821.735	7.821735	46%	5.233965	7.913755661
325.63	53.8002	66.51	1.236241	3578.251	3.578251	21%	2.39441	3.620348376
326.75	49.6273	67.38	1.35772	3343.887	3.343887	20%	2.237584	3.383227327
327.45	31.7435	67.92	2.139651	2156.019	2.156019	13%	1.442714	2.181383444
328.50	38.45	68.9376	1.792915	2650.651	2.650651	16%	1.7737	2.681834846
329.76	26.5272	66.63	2.511762	1767.507	1.767507	10%	1.182739	1.78830154
330.81	29.9551	64.21	2.143542	1923.417	1.923417	11%	1.287067	1.946045406
332.43	86.438	63.4158	0.733656	5481.535	5.481535	32%	3.668005	5.546023567
333.55	24.5901	63.48	2.581527	1560.98	1.56098	9%	1.04454	1.579344013
334.95	29.9551	63.6129	2.123608	1905.531	1.905531	11%	1.275098	1.92794879
335.58	37.4068	64.87	1.734177	2426.579	2.426579	14%	1.623761	2.455127106
336.49	157.2273	66.13	0.420601	10397.44	10.39744	61%	6.957516	10.51976419
337.26	22.5037	67.0073	2.977613	1507.912	1.507912	9%	1.009029	1.52565232
338.66	20.8642	68.27	3.272112	1424.399	1.424399	8%	0.953146	1.441156569
339.99	21.0134	69.37	3.301227	1457.7	1.4577	9%	0.975429	1.474848965
342.02	24.4409	70.0658	2.866744	1712.471	1.712471	10%	1.145911	1.732617931

354.48	24.2921	72.5706	2.987416	1762.892	1.762892	10%	1.179651	1.783632181
355.53	0	72.6425	0	0	0	0%	0	0
359.74	0	72.9097	0	0	0	0%	0	0

Annex 4 – Simulation Parameters

Electric vehicle simulation parameters

```
%Electric vehicle simulation with hybrid energy storage system as
%battery-supercapacitor.

%Electric Vehicle (Forklift Carer R45NCF)
%with Hybrid Energy Storage System.
%80 V, 960 Ah, Generic Battery Pack &
%80.5 V, 300 F, Generic Supercapacitor Module
%80 V, 454 F, Ni-Cu/AC Hybrid Supercapacitor Module

clc; clear all;

%Vehicle parameters
Mpilot  =80;                    % Mass of pilot                                    [kg]
mvehicle=6950;                  % Mass of vehicle-Service weight(incl.batt.pack)  [kg]
h_CG    = 870;                  % Centroid height                                  [mm]
drag    = 1.2;                  % Drag coefficient
faxle   =800;                   % Front axle                                       [mm]
raxle   =1150.5;                % Rear axle                                        [mm]
farea   =2.25;                  % Frontal area                                     [m^2]

%Wheels parameters
w_b     =10;                    % B tire coefficient
w_c     =1.9;                   % C tire coefficient
w_d     =1;                     % D tire coefficient
w_e     =0.97;                  % E tire coefficient
Dw      =84;                    % Front wheel diameter (Front driven)              [cm]
Mw      =250;                   % Front wheel mass (Front driven)                  [kg]
winertia=mw*(Dw/2/100)^2;       % Tires inertia
[kg*m^2]
rolresist=0.006;                % Rolling resistance coeff.(truck tires on asph.)


%% Generic Battery Parameters 960Ah 2V 1mOhm - Pack with 40 series batteries

Ns    = 40;                     % Series cells                                     [unt]
Np    = 1;                      % Parallel cells                                   [unt]
AH    = 960;                    % Ampere-hour rating                               [hr*A]
Vnom  = 2;                      % Nominal voltage                                  [V]
Q     = AH*Vnom*Ns;             % Battery capacity                                 [W*hr]
Rib   = 0.001;                  % Internal resistance                              [Ohm]
V1    = 0.9*Vnom*Ns;            % Voltage V1 < Vnom when charge is AH1             [V]
AH1   = AH/2;                   % Charge AH1 when no-load volts are V1             [hr*A]
AH0   = 0.7*AH;                 % Initial charge                                   [hr*A]
Ich   = 100;                    % Charging current - Charge PBM Italy 72Vdc,400A   [A]
SOCi  = 100;                    % Initial State of Charge                          [%]
Tamb  = 25;                     % Ambient temperature                              [°C]

%% Other Parameters
Ts    = 0.01;                   % Fundamental sample time                          [s]
Cdc   = 0.001;                  % Capacitance                                      [F]
Vcdc0 = 0.95*Vnom;              % Initial Capacitor voltage                        [V]

%% Supercapacitor Maxwell 2.3V 300F Parameters
Ri    = 0.0043;                 % Immediate branch resistance                      [Ohm]
Ci0   = 168.3746;               % Immediate branch cte capacitance                 [F]
Kv    = 116.7993;               % Immediate branch capacitance cte parameter       [F/V]
Rd    = 0.8392;                 % Delayed branch resistance                        [Ohm]
Cd    = 89.7711;                % Delayed branch capacitance                       [F]
Rl    = 12.1234;                % Long-term branch resistance                      [Ohm]
Cl    = 165.1719;               % Long-term branch capacitance                     [F]
Vsc   = 2.3;                    % Nominal  voltage                                 [V]
R     = [0.00440429447538712 3.85744007824104 12.0602576306802];
C     = [168.565477206141 72.7295126675884 146.52752720182];
Np_sc = 1;                      % Number of parallel cells                         [unt]
Ns_sc = 35;                     % Number of series cells connections               [unt]
```

```
%% Supercapacitor Ni-Cu 2V 4546F Parameters
Ria    = 0.002667114;          % Immediate branch resistance                    [Ohm]
Ci0a   = 218.3258456;          % Immediate branch cte capacitance               [F]
Kva    = 245.0375629;          % Immediate branch capacitance cte parameter     [F/V]
Rda    = 1.522937446;          % Delayed branch resistance                      [Ohm]
Cda    = 129.8708916;          % Delayed branch capacitance                     [F]
Rla    = 9.635474826;          % Long-term branch resistance                    [Ohm]
Cla    = 243.483842;           % Long-term branch capacitance                   [F]
Vsca   = 2;                    % Nominal  voltage                               [V]
Ra     = [0.00266711436954014 1.52293744575966 9.63547482595327];
Ca     = [218.325845584342 129.870891561134 243.48384199323];
Np_sca = 1;                    % Number of parallel cells                       [unt]
Ns_sca = 40;                   % Number of series cells connections             [unt]


R_discharge = 9e3;

% Input current by configuring the Step block parameters of the Supercapacitor
Parameter identification block [MathWorks19c].
%%Maxwell

%stepTime = [40 1900 1917];     % Step time                                      [s]
%initialValue = [18 0 0];       % Initial value                                  [A]
%finalValue = [0 -20 20];       % Final value                                    [A]

%%Ni-Cu

%stepTime = [40 1900 1917];     % Step time                                      [s]
%initialValue = [23 0 0];       % Initial value                                  [A]
%finalValue = [0 -25 25];       % Final value                                    [A]
```

Annex 5 – Supercapacitors Laboratorial Tests and Manufacturing Processes

5.1 Asymmetric Cell Configuration

Supercapacitors cells, according to [Ratha18], can be configured in many different forms which are defined based on either the type of electrodes, electrolyte, current collectors, separator and casing (Fig.A5.1).

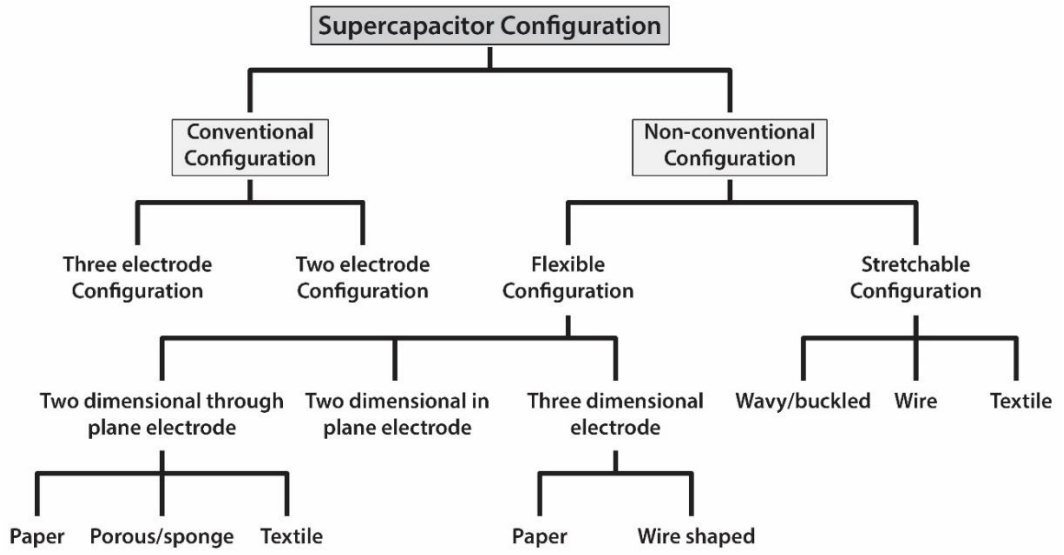

Figure A5.1 – Supercapacitors cell configurations [Ratha18].

As this dissertation aims to use data obtained from laboratorial tests for Ni-Cu metallic foams as alternative for supercapacitors positive electrodes, material which is described as a metal oxide, which pseudocapacitive properties are therefore destined to hybrid supercapacitors, only the conventional configurations, two and three electrodes, will be taken into consideration since these are the usual supercapacitor's cell configuration for the respective tests [Ratha18] and as presented in [Eugénio13]. Complementary, as described in sections 3.1 and 3.2, in hybrid supercapacitors, its configuration can be defined as being asymmetric which also provides the best energy results, therefore, the structure is composed of two different active materials, which defines the emphasis solely in asymmetric device configuration.

Also, it is important to state that such setups can referrer to either the supercapacitor's cell or test configuration.

Asymmetric Configuration

In an asymmetric configuration, the supercapacitor is either constructed with two different active materials for each electrode [Roldán15], or as a hybrid device by combining faradic battery-type with capacitive electrode [Stoller10], which in both cases usually leads to higher potential difference, therefore, increase in cell working voltage [Roldán15].

Asymmetric supercapacitors can be classified regarding their technology (Fig.A5.2) [Roldán15].

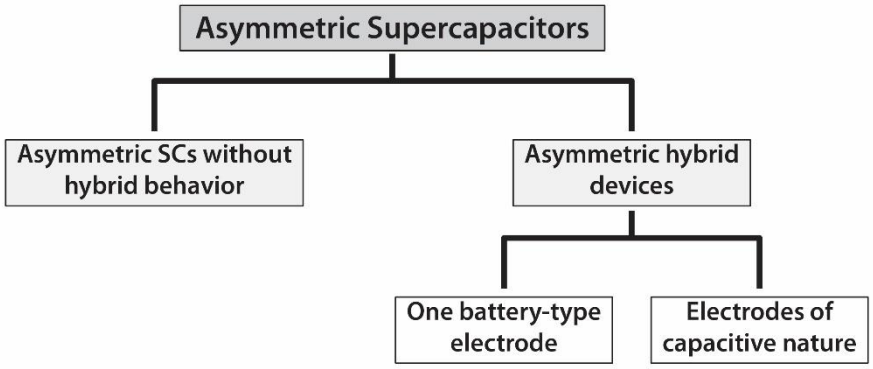

Figure A5.2 – Asymmetric supercapacitors classification [Roldán15].

Three-electrode Configuration

With regards to the testes performed on supercapacitor's cells, the three-electrode (3E) configuration comprises three different electrodes, only one electrode containing the active material, the so-called working electrode, a reference electrode and an auxiliary electrode, which are dipped in an electrolyte solution (aqueous or not) (Fig.A5.3) [Ratha18].

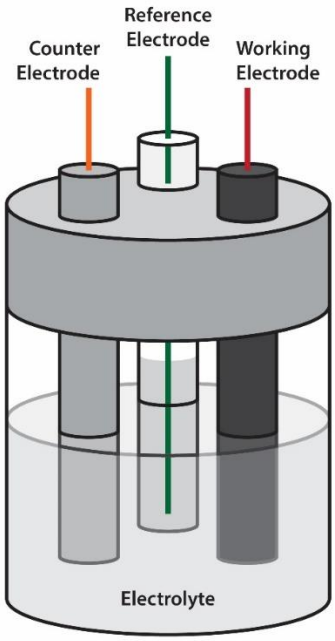

Figure A5.3 – Three-electrode (3E) configuration [Ratha18].

According to [Stoller10], the working electrode contains the material which is the subject of analysis and the voltage applied on this single electrode is significantly different than in a two-electrode (2E) setup. In a 3E cell, the voltage applied to the working electrode is with respect to referenced active material being tested, while for a symmetrical 2E cell the potential difference is the same for both electrodes, therefore one-half than for the 3E [Stoller10].

The reference electrode, as described by [Ratha18], is often a silver chloride electrode (Ag/AgCl) or a saturated calomel electrode (SCE), which is based on a mercury-chloride/elemental mercury reaction [Compton12]. As for the auxiliary electrode, also called counter electrode, platinum wire is commonly implemented for such usage [Ratha18].

Two-electrode Configuration

According to [Ratha18], in a two-electrodes (2E) configuration, there are two working electrodes, which are formed by the deposition of active material on the current collector, divided by a porous membrane called separator, which soaked with electrolyte

(Fig.A5.4). The 2E setup mimics a real supercapacitor [Qu98] which measurement supplies proper capacitance and power values [Ratha18].

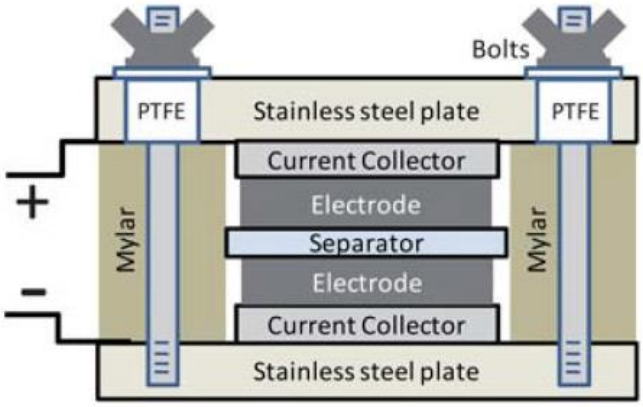

Figure A5.4 – Two-electrode (2E) configuration [Stoller10].

The 2E tests cells are commercially available in many forms, such as the Swagelok type, screwed metallic plates and coin cells [Ratha18].

This test configuration is the most popular amongst material researchers in order to perform efficiency tests for electrodes and devices prototypes [Ratha18].

5.2 Cyclic Voltammetry - CV

According to [Béguin13], cyclic voltammetry (CV) is a widely implemented transient technique by researchers due to its versatility. As testing large devices would not be technically simple as the large active material volumes would require a great amount of current, researchers rely on CV for testing scaled experiments or prototypes, which provides very accurate results [Béguin13]. This powerful technique is commonly implemented in the investigation of reduction and oxidation processes of molecular species [Elgrishi18].

The concept of cyclic voltammetry is the application of a linear varying potential called working potential window, which runs across the working electrode on a three-electrode configuration or across both electrodes in a two-electrode setup [Ratha18].

As test result it generates a voltammogram or cyclic voltammogram (Fig.A5.5) which is defined by an *XY*-axis graph where the horizontal axis represents a parameter imposed to the system, normally attributed to potential (*E*), also referred as voltage (*V*), as for the vertical axis it is attributed to the response, often set as current (*I*) [Elgrishi18].

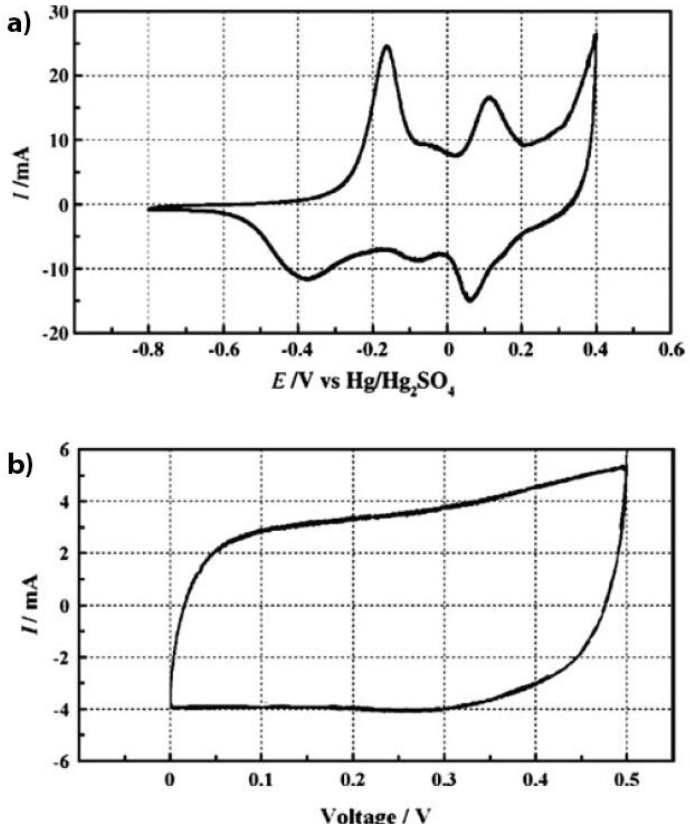

Figure A5.5 –Three (a) and two-electrodes (b) cell cyclic voltammetry (CV) [Stoller10].

The cyclic voltammetry is considered, for purely capacitive electrodes, the best practice to acquire values of specific capacitance from each electrode in a three-electrode setup [Roldán15].

5.3 Galvanostatic Charge and Discharge - GCD

The galvanostatic charge and discharge cycle (GCD) test, also called galvanostatic cycle or *chronopotentiometry*, is a very much different test then cyclic voltammetry because in GCD the current is controlled while the voltage is measured against time [Béguin13].

According to [Allagui16], it consists of applying a stepping current (*I)* and analyzing the resulting transient voltage (*V*) (Fig.A5.6).

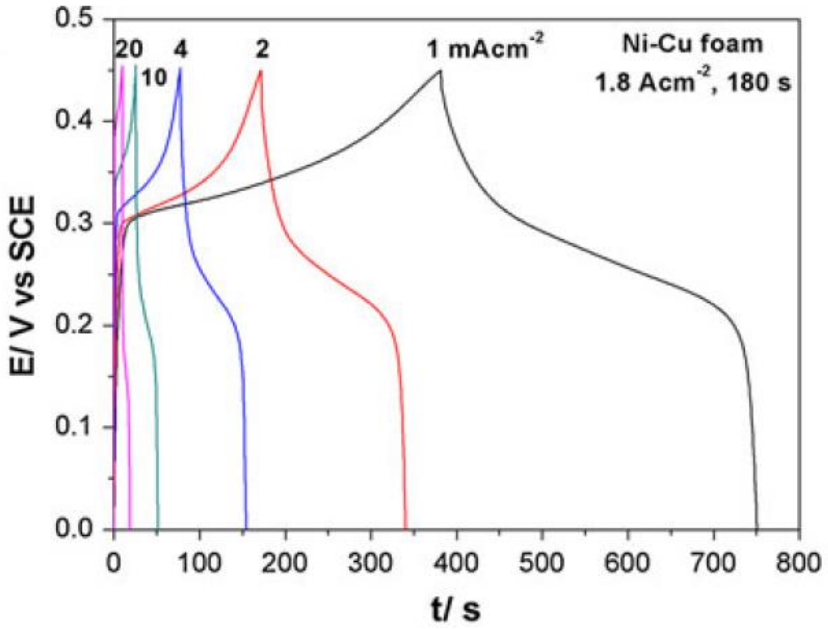

Figure A5.6 – Ni-Cu metallic foam GCD [Eugénio13].

In batteries research field, GCD is the most widely implemented test technique as it allows scaling of laboratorial tests to industrial purposes [Béguin13]. From the tests results different parameters can be acquired, such as capacitance, resistance and cyclability [Béguin13].

5.4 Electrodeposition

Electrodeposition or electrochemical deposition is a well-known technique of depositing metals as layers in certain conducting substrates [Arulmani18]. As described by [Narayanan15], the technique is similar to electrophoretic deposition, which takes place in an electrochemical cell, however, in this case a chemical bonding process occurs.

For the deposition process, electric current is used [Arulmani18]. During the process, ions available in the electrolyte or the anode, due to the replenishment process, will be deposited on the cathode. In order to obtain optimized grain sizes from the deposition

process, which is stated to be in the range of nanometers, adjustments on the controlling variables are required (bath composition, pH, temperature and current density) [Arulmani18].

Typically, potentiostatic and galvanostatic (GV) techniques are implemented in electrodeposition process under different potential ranges, time duration and current densities [Arulmani18]. In [Eugénio13] the Ni-Cu metallic foams were electrodeposited by applying hydrogen bubble evolution as dynamic template. The deposition was performed from an electrolyte solution containing 0.5 M $NiSO_4.7H_2O$, 1.5 MH_2SO_4, 1 M HCl and 0.01 M $CuSO_4.5H_2O$, in a two-electrode cell connected to a power source, with stainless steel plates (substrates) as working electrodes and a platinum plate was implemented as counter electrode. This technique of producing NFMs is very versatile, creating large arrays of morphologies when tuning the variables involved. By taking advantage of the dynamic template formed by the hydrogen bubbling, which often occurs simultaneously with metal deposition, it results in a one-step, cost reduced fabrication method [Eugénio13].

According to [Narayanan15], the advantages of electrodeposition as electrode manufacturing process includes the relative low-cost and improved interfacial bonding between the coated material and substrate before the heat treatment or sintering. In completion, to emphasize relatively lower cost of such procedure it is important to mention that his affirmation is partly consequence of the process being energy efficient where it is typically carried at near room temperature [Escoubas13].

Annex 6 – Ni-Cu Hybrid Supercapacitors Computational Simulation

6.1 Computational Model

Throughout the software Matlab 2018b and its simulation tool Simulink, a computational model of a supercapacitor was developed of either the Maxwell 300F 2.3V pseudocapacitor and the theoretical Ni-Cu hybrid supercapacitor data, so it could be implemented in a further complex analysis, as it is the case of electric vehicles hybrid energy storage system simulation.

The Simulink supercapacitor block (Fig.A6.1) (Simscape/Electrical/Power Systems/Sources) was chosen to either directly represent the Maxwell pseudocapacitor and regarding its circuit structure, as basis for the faradaic branch of the Ni-Cu hybrid supercapacitor.

Figure A6.1 – Matlab 2018b – Simulink supercapacitor block [MathWorks19a]

In order to properly configure the block, its structure requires the input of three resistances values, R_1 to R_3, as well as three capacitances, C_1 to C_3 and a voltage-dependent capacitor gain (Fig.A6.2).

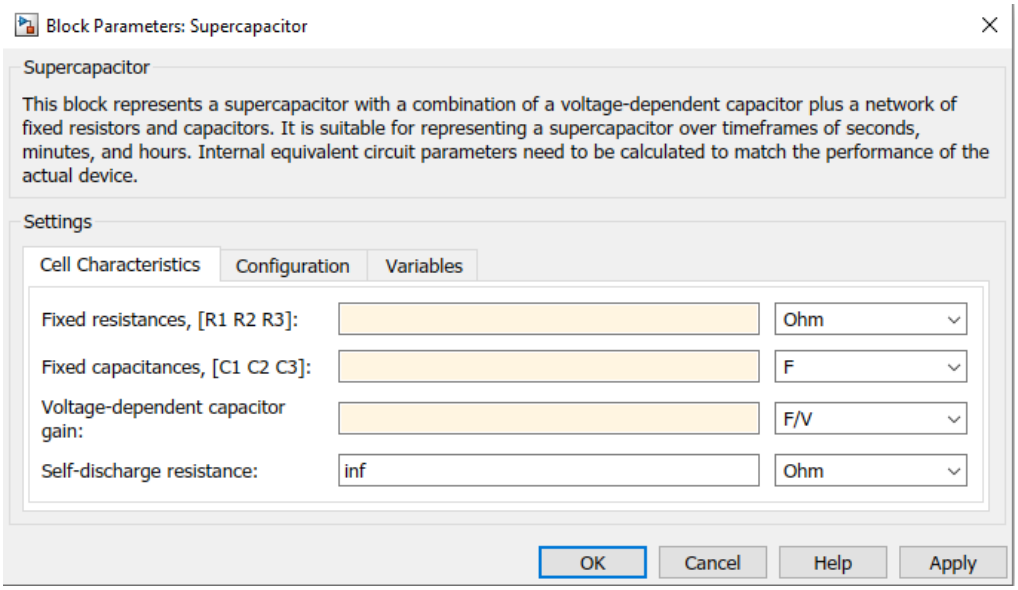

Figure A6.2 – Matlab 2018b – Simulink, supercapacitor block parameters input [MathWorks19b]

The required values are related to the parameters identification procedure which takes into consideration a three branches structure (Fig.A6.3) [MathWorks19a].

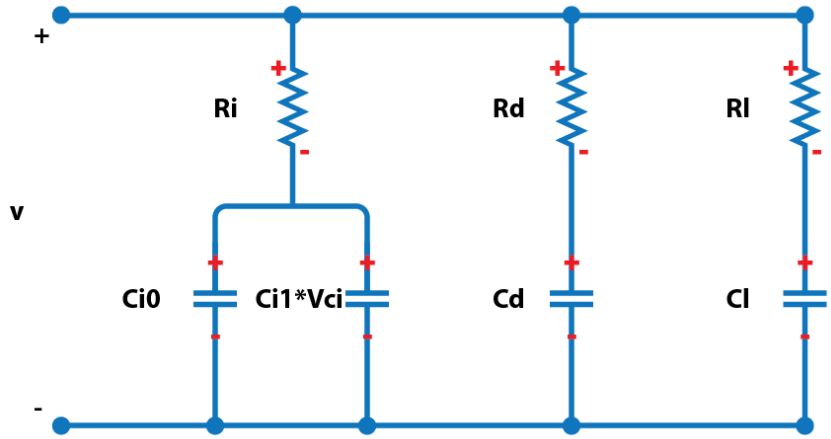

Figure A6.3 – Matlab 2018b – Simulink, supercapacitor block electric circuit [MathWorks19a, Zubieta00]

Where Ri (R1 for Simulink block), Ci0 and Ci1 represents the immediate resistance, constant capacitance and a constant parameter, also defined as voltage dependent

capacitor gain [MathWorks19a], respectively. The capacitance Ci (C1 for Simulink block) is defined by (A6.1) [Zubieta00].

$$Ci = Ci0 + Ci1.Vci[F] \quad \text{(A6.1)}$$

The second is the delayed branch, which dominates the thermal behavior and is composed by Rd (R2 for Simulink block) and Cd (C2 for Simulink block). As for the third, it is described as the long-term branch which determines the device's behavior for periods longer than 10 minutes and is composed of Rl (R3 for Simulink block) and Cl (C3 for Simulink block).

With the intent to identify the input parameters, the procedure described by [Zubieta00] was performed aided by the Simulink simulation example for the supercapacitor's parameters identification (Fig.A6.4) [MathWorks18b], which was also based on [Zubieta00].

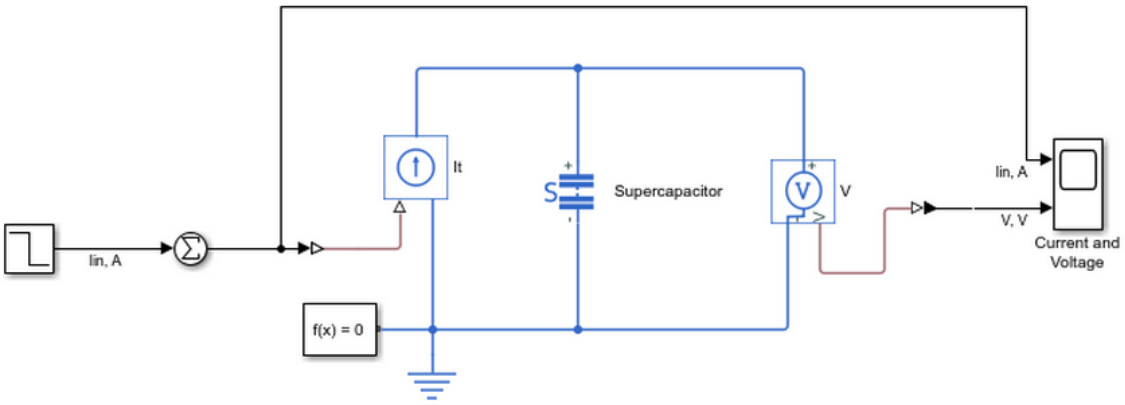

Figure A6.4 – Matlab 2018b – Simulink, Supercapacitor Parameter Identification example [MathWorks19c]

According to [MathWorks19c], in order to identify the required parameters one can, use the typical voltage waveform (Fig.A6.5) from the base values supplied by the example. With that said, throughout the CAD software AutoCAD 2014 the waveform of [MathWorks19c] was vertically stretched (Fig.A6.6) to fit the desired 2V of the Ni-Cu hybrid supercapacitor maintaining the time constraints imposed by the procedures of

[Zubieta00] and [MathWorks19c]. As for the Maxwell pseudocapacitor, as the example already described was a 2.3V device the original waveform was maintained as basis (Fig.A6.5).

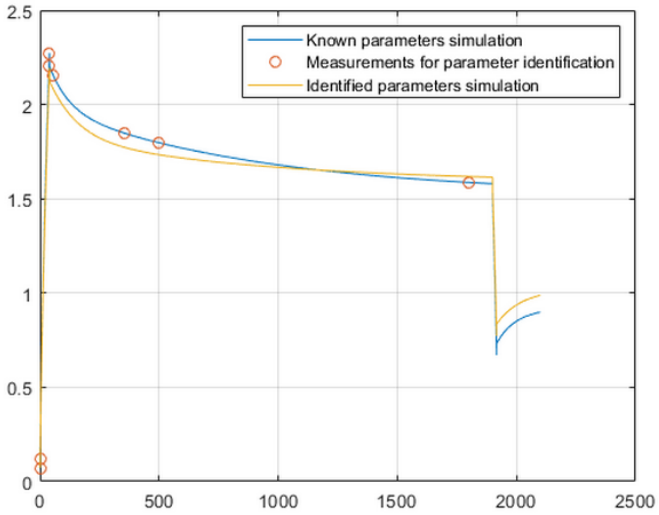

Figure A6.5 – Matlab 2018b – Simulink, Supercapacitor Parameter Identification example – Proposed waveform for 2.3V device [MathWorks18c]

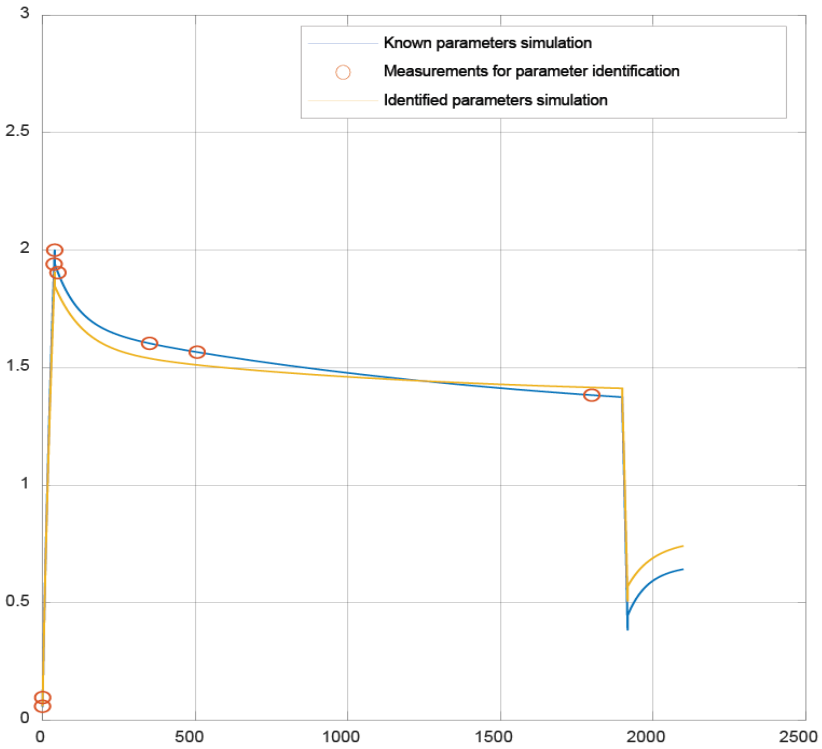

Figure A6.6 –Supercapacitor Parameter Identification – Proposed waveform for Ni-Cu 2V device

The method described in [Zubieta00] consists of 8 steps (Annex 2) which takes into consideration experimental charge and discharge procedures from which various voltage and time measurements are obtained, values that are required for the completion of the steps parameters calculations.

In order to do so, a nonlinear optimization problem (NLP) was implemented in Microsoft Excel 365 Plus Solver plugin, GRG nonlinear solving method, taking into consideration the fixed parameters present in both [Zubieta00] and [MathWorks19c] (Annex 2). From [Maxwell18a] the Maxwell 300F 2.3V device's rated voltage and capacitance were extracted, while as for the Ni-Cu hybrid supercapacitor, the analogous data was gathered from the calculations in Annex 5.

The real supercapacitor capacitance was assumed as given by (A6.2) [Zubieta00].

$$Cq = Ci0 + Ci1.Vci[F] \quad \text{(A6.2)}$$

The time and voltage values obtained for each device are presented in (Table A6.1) and (Table A6.2).

Table A6.1 – Maxwell 300F 2.3V pseudocapacitor parameters identification

Def.	Time (s)	Voltage (V)
Fixed	0.02	0.0718
Variable	0.537	0.1218
Fixed	40	2.2717
Fixed	40.02	2.2019
Variable	56.695	2.1519
Fixed	356.695	1.8473
Variable	499.025	1.7973
Fixed	1800	1.5865

Table A6.2 – Ni-Cu hybrid supercapacitor parameters identification

Def.	Time (s)	Voltage (V)
Fixed	0.02	0.0582
Variable	0.52	0.1082
Fixed	40	2.0000
Fixed	40.02	1.9236
Variable	50.54	1.9043
Fixed	350.54	1.6034
Variable	505.99	1.5662
Fixed	1800	1.3834

The respective resistances and capacitances values are presented in (Table A6.3) and (Table A6.4).

Table A6.3 – Maxwell 300F 2.3V pseudocapacitor parameters identification

Parameter	Value
Ri	0.0043
Ci0	168.3746
Ci1	116.7993
Rd	0.8392
Cd	89.7711
Rl	12.1234
Cl	165.1719
Cdiff	428.7055
Cq	300.00
Qtotal	676.1623
Vci	2.2289
Ich	18.00

Table A6.4 – Ni-Cu hybrid supercapacitor parameters identification

Parameter	Value
Ri	0.0027
Ci0	218.3258
Ci1	245.0376
Rd	1.5229
Cd	129.8709
Rl	9.6355
Cl	243.4838
Cdiff	687.3174
Cq	454.0000
Qtotal	873.3034
Vci	1.9110
Ich	23.00

The values were then applied to the parameter's identification simulation, which output is depicted in (Fig.A6.7) and (Fig.A6.8).

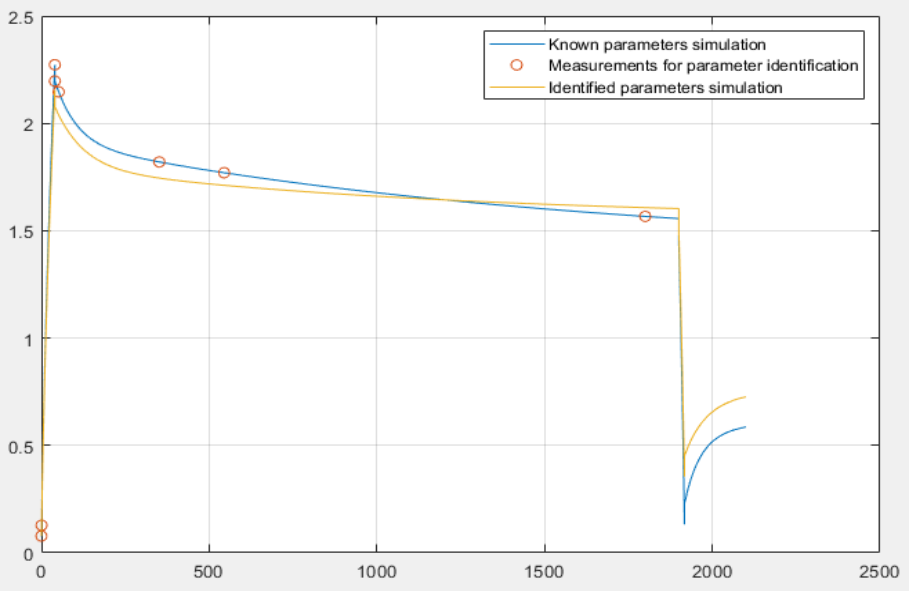

Figure A6.7 –Supercapacitor Parameter Identification – Simulated waveform for Maxwell 300F 2.3V device

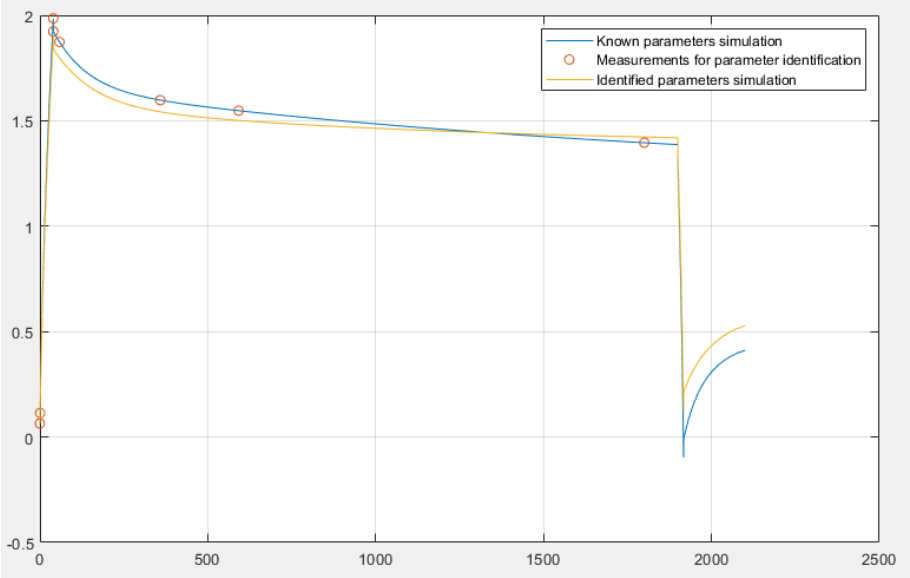

Figure A6.8–Supercapacitor Parameter Identification – Simulated waveform for Ni-Cu 454F 2V device

As one can notice, both (Fig.A6.6) (Fig.A6.8) depict a very similar waveform, which validates the parameters generated in (Table A6.4) towards the simulation procedure. The resulting values are presented in (Table A6.5) and (Table A6.6).

Table A6.5 – Ni-Cu hybrid supercapacitor simulation results

Time (s)	**Voltage (V)**
0.02	0.063264
0.51573	0.11326
40	1.999
40.02	1.9377
68.354	1.8877
368.35	1.62
510.97	1.57
1800	1.3912

Table A6.6 – Ni-Cu hybrid supercapacitor simulation results

Parameter	Value
Ri	0.0028
Ci0	228.0359
Ci1	254.6858
Rd	1.5156
Cd	133.5609
Rl	7.1731
Cl	122.5403
Cdiff	634.2645
Cq	474.787
Qtotal	920.00
Vci	1.5729
Ich	23.00

Despite the fact that the Simulink supercapacitor block is proposed as an EDLC example, it was assumed as sufficiently feasible for implementing both the Maxwell 300F 2.3V pseudocapacitor and the Ni-Cu hybrid supercapacitor, as the values for capacitance and voltage are already known from the datasheet [Maxwell18a] and experimental data [Eugénio13], respectively.